UNIVERSITÀ DEGLI STUDI DI NAPOLI FEDERICO II

Facoltà di Scienze Matematiche Fisiche e Naturali

Study of single-top production in the *t*-channel with the CMS experiment at LHC at $\sqrt{s} = 8$ TeV

Tesi di Laurea Magistrale in Fisica
A.A. 2012/2013

Relatori:	Candidato:
Ch.mo Prof. Crisostomo Sciacca	Francesco Fienga
Dott. Luca Lista	N94/40
Dott. Alberto Orso Maria Iorio	

to my family

"Now the smallest Particles of Matter may cohere by the strongest Attractions
and compose bigger Particles of weaker Virtue; and many of these may cohere
and compose bigger Particles whose Virtue is still weaker, and so on for divers
Successions, until the Progression ends in the biggest Particles on which
the Operations in Chemistry and the Colours of natural Bodies depend,
and which by cohering compose Bodies of sensible Magnitude.
There are therefore Agents in Nature able to make
the Particles of Bodies stick togheter by very strong Attractions.
And it is the Business of Experimental Philosophy to find them out."

Isaac Newton, Opticks, 1704

CONTENTS

INTRODUCTION

The Large Hadron Collider (LHC) at CERN is a circular accelerator designed to provide proton-proton (and lead-lead ions) collisions with the unprecedented luminosity of 10^{34} cm^{-2} s^{-1} and a centre-of-mass energy of 14 TeV suitable for the study of rare events such as the production of the Higgs boson. Four are the main experiments situated in the interaction points where the proton beams collide: the general purpose CMS and ATLAS , the *B*-physics-oriented LHC*b* and the experiment dedicated to ion collisions, ALICE . During the first years of running the CMS and ATLAS collected more than 30 fb^{-1} of data and published an impressive amount of physics results spanning from the first Standard Model precision tests, i.e. vector bosons production, to more complex and challenging measurements as top strong and electroweak production, towards the announcement of the discovery of a Higgs like boson and new physics beyond the Standard Model (supersymmetry, extra-dimension theoretical models, etc.).

The work presented in this thesis consists of the study of one of the electroweak production modes of the top quark, the *t*-channel single top, done analyzing the collision data collected by the CMS detector during 2012 data taking. The top quark, heaviest of the six constituting the three families of known quarks, was observed for the first time in the associated $t\bar{t}$ production at the proton-antiproton collider Tevatron at Fermilab in 1995. With more and more collected data, precision measurements of the top quark properties could be performed, till the first observation of the single top quark production in 2009 (first observation at LHC in 2010). The increased center of mass energy and the higher luminosity of the machine, make the LHC a top quark factory, producing at nominal energy and intensity around 1 $t\bar{t}$ pair per second and around 30 single tops per minute.

The aim of the analysis presented is to measure the *t*-channel single top production cross section and charge asymmetry after appropriate treatment of the underlying backgrounds has been established. For this purpose a data-driven estimation technique has been set up in order to minimize the effect of theoretical model uncertainties on the various backgrounds. Taking advantage of the particular topology of the process and of the spin correlations between the particles involved, a template fit signal extraction is performed and the *t*-channel cross section is measured both, inclusively and singly for top and anti top processes. The present thesis is organized in four chapters:

CHAPTER 1 briefly introduces the Standard Model of elementary particles.

CHAPTER 2 is devoted to a detailed description of the LHC accelerator machine and to the CMS detector.

CHAPTER 3 presents the theoretical and experimental state of the art concerning the top quark physics, with particular stress on the recent measurements obtained at hadron colliders.

CHAPTER 4 contains the detailed description of the analysis set up for the single top cross section measurement in the t-channel. Starting from the event selection algorithm, the data-driven techniques for backgrounds estimation are presented and in the end the fit procedure for signal extraction is described. This analysis is performed using part of the data collected by CMS in 2012.

My thesis work has been devoted to the study of methods used to estimate the yield of the different sources of background directly from data. These methods have been implemented in the analysis notes which describe the current procedure to extract the inclusive cross-section and to measure the charge asymmetry for single-top *t*-channel events at a centre-of-mass of 8 TeV. In chapter 4 these method are described in details and the preliminary results for the measurement of the inclusive and charge divided cross-section are given.

1 THE STANDARD MODEL OF PARTICLE PHYSICS

1.1 OVERVIEW

The Standard Model of particle physics is a $SU(3) \times SU(2) \times U(1)$ relativistic Quantum Field Theory (QFT) developed to describe the electroweak and strong interactions of elementary particles in a single framework. The theory was initially designed to combine electrodynamics with the weak interaction by Sheldon Glashow in 1960 [1] and later in 1967 by Steven Weinberg [2] and Abdus Salam [3], who incorporated the Higgs mechanism [4, 6]. As a result of their work, the three shared the Nobel Prize in Physics in 1979 "for their contributions to the theory of the unified weak and electromagnetic interaction between elementary particles, including, inter alia, the prediction of the weak neutral current". In addition, the theory of strong interaction, Quantum Chromodynamics (QCD), was developed in parallel through the 60s and 70s. In 1964, Murray Gell-Mann and George Zweig independently suggested the existence of quarks with different flavors as the components of hadrons [7] and, in 1965, Moo-Young Han with Yoichiro Nambu [8] and Oscar W. Greenberg [9] proposed an additional $SU(3)$ gauge degree of freedom, the color charge. The theory reached its present form in 1973 with the discovery of asymptotic freedom of strong interactions by David Politzer [10, 11] and David Gross together with Frank Wilczek [12]. The three were awarded the Nobel Prize in Physics in 2004 "for the discovery of asymptotic freedom in the theory of the strong interaction".

In the Standard Model of particle physics, all elementary particles are classified in two categories: bosons and fermions. The fermions are half-integer spin particles obeying the Pauli Exclusion Principle and a total of twelve fermions, with their respective antiparticle, are known to date. Fermions are divided in two categories: quarks (up, down, charm, strange, top, bottom) and leptons (electron, muon, tau, and their corresponding neutrinos). Quarks hold electric charge, weak isospin, color charge and, therefore, interact through both electroweak and strong forces. Due to confinement (a property of strong interaction), quarks have never been observed as free particles, forming instead bound states of color neutral particles, the hadrons, which are divided into baryons and mesons. Leptons have zero color charge, therefore can only interact through the electroweak force. As neutrinos also do not have electric charge, only interact via the weak force. On the other hand, all interactions in the Standard Model are mediated by bosons, which are integer spin particles. There are three kinds of force mediating particles: photons, massive bosons and gluons. The photon is a massless particle and, together with the three massive bosons (W^+, W^- and Z), mediates the electroweak interaction. The Z boson is electrically neutral and more massive than the W boson ($m_W = 80.399 \pm 0.023$ GeV and $m_Z = 91.1876 \pm 0.0021$ GeV) [13]. The mediator of the strong force is the gluon; according to QCD, there are eight different massless and color charged gluons that can also interact with themselves. Finally, the Higgs boson, theorized in 1964 [4, 6] to explain the spontaneous breaking of electroweak symmetry, or in other words, how the other elementary particles acquire mass. The Higgs particle is a massive scalar boson, with zero electric charge and is its own anti-particle.

The Standard Model of particle physics is the most successful theory of elementary particles and interacting fields built to date. The development of renormalization in Quantum Electrodynamics (QED) by Ernst Stueckelberg [14], Julian Schwinger [15, 16], Richard Feynman [17, 19], Sin-Itiro Tomonaga [20] and Freeman Dyson [21, 22], led to an outstanding agreement between theory and experiment. The discovery of the massive gauge bosons in 1983 by UA1 and UA2 collaborations established the Glashow-Weinberg-Salam model as one of the pillars of the SM [23, 24], for which Carlo Rubbia and Simon van der Meer were laureated with the Nobel Prize in Physics in 1984. Furthermore, several tests have been performed on perturbative QCD throughout the years, such as the jet production cross sections, Drell-Yan processes, the running QCD coupling, the production of heavy flavors, among others [25].

1.2 ELECTROWEAK INTERACTION

The electroweak interaction is formulated as a $SU(2) \times U(1)$ gauge theory that unifies the electromagnetic and weak interactions. The electromagnetic interaction alone is described by the quantum electrodynamics, a relativistic quantum field theory that describes how electrically charged particles interact by means of exchange of photons. The weak interaction was first theorized by Fermi as a four fermion contact interaction [26], and is nowadays described as a short-ranged interaction mediated by massive bosons. The weak interaction comprises several unique features such as the violation of parity symmetry (P), conserved in the electromagnetic interaction, the violation of charge conjugation symmetry (C), the violation of the combination of charge conjugation and parity symmetries (CP), the capacity of changing quark flavors, *i.e.* changing one quark into another of a different kind, the existence of massive gauge bosons from which

stems the need for a spontaneous symmetry breaking mechanism.
Even though the electromagnetic and the weak interactions do not seem to be related at low energies, the two are unified around the order of the electroweak energy scale, $v = 246$ GeV. The formulation of the electroweak unification under the $SU(2)_L \times U(1)$ gauge group is presented in the next sections.

1.2.1 Quantum Electrodynamics

The interaction between a Dirac fermion and the electromagnetic field can be derived by requiring local $U(1)_Y$ gauge invariance on the Lagrangian for a free Dirac fermion, *i.e.* using the gauge principle.
The Lagrangian for a free Dirac massive fermion is:

$$\mathcal{L} = i\overline{\psi}(x)\gamma^\mu\partial_\mu\psi(x) - m\overline{\psi}(x)\psi(x), \tag{1}$$

where $\psi(x)$ in the Dirac field, m is the mass field, γ^μ represents the gamma matrices [**?**], and $\overline{\psi}(x) = \psi^\dagger\gamma^0$. The free Dirac Lagrangian is invariant under global $U(1)$ gauge transformations:

$$\psi(x) \to \psi^{'}(x) = e^{iQ\theta}\psi(x), \tag{2}$$

where Q is the electric charge in units of the elementary charge e, and θ is an arbitrary real constant value. However, the same Lagrangian is not invariant under local $U(1)$ gauge transformations, *i.e.* in case the phase depends on the space-time coordinates ($\theta = \theta(x)$):

$$\partial_\mu\psi(x) \to \partial_\mu\psi^{'}(x) = e^{iQ\theta}(\partial_\mu + iQ\partial_\mu\theta)\psi(x). \tag{3}$$

To guarantee the local $U(1)$ gauge invariance, an additional spin-1 field has to be introduced:

$$A_\mu(x) \to A^{'}_\mu(x) = A_\mu(x) - \frac{1}{e}\partial_\mu\theta(x). \tag{4}$$

Therefore, the gauge invariant Lagrangian under local $U(1)$ transformations is:

$$\begin{aligned}\mathcal{L} &= i\overline{\psi}(x)\gamma^\mu D_\mu\psi(x) - m\overline{\psi}(x)\psi(x)\\ &= i\overline{\psi}(x)\gamma^\mu\partial_\mu\psi(x) - m\overline{\psi}(x)\psi(x) - eQA_\mu\overline{\psi}(x)\gamma^\mu\psi(x),\end{aligned} \tag{5}$$

where the covariant derivative is defined as $D_\mu\psi(x) = (\partial_\mu + ieA_\mu(x))\psi(x)$. To complete the QED Lagrangian an additional, gauge invariant, kinetic term needs to be introduced, which describes the propagation of the $A_\mu(x)$ field:

$$\mathcal{L} = -\frac{1}{4}F^{\mu\nu}(x)F_{\mu\nu}(x), \tag{6}$$

where $F^{\mu\nu}(x) = \partial^{\mu}A^{\nu} - \partial^{\nu}A^{\mu}$. Moreover, in order to preserve the local $U(1)$ gauge invariance of the Lagragian the photon must be massless since the mass term for the gauge field $\mathcal{L}_m = \frac{1}{2}m^2 A_{\mu}A^{\mu}$ is not gauge-invariat.

QED has been tested throughout the years with an unprecedented precision. In particular, the high-precision measurement of the electron anomalous magnetic moment provides the most accurate determination of the fine structure constant [27]:

$$\alpha^{-1} = 137.035999084 \pm 0.000000051. \tag{7}$$

1.2.2 Weak Interaction

The weak interaction manifests itself through the charged and neutral currents, by means of the $W^{\pm}$ bosons and the Z boson, respectively. The experimental results obtained over more than one century, from early studies on the β-decay to modern neutrino scattering experiments, provide information on the nature of these currents. In particular, the charged current exhibits the following features:

- Only left-handed (right-handed) fermions (anti-fermions) couple with the $W^{\pm}$ bosons: the weak interaction violates parity conservation [28, 29].
- All fermion doublets couple to the $W^{\pm}$ bosons with the same strength, also known as the "weak universality" [30].
- The weak eigenstates of the three generation of quarks are different from the mass eigenstates. The weak eigenstates of the three down-type quarks, $|d_i^{'}\rangle$, are related to the mass eigenstates, $|d_j\rangle$, as [31]:

  $$|d_i^{'}\rangle = \sum_j \mathbf{V_{ij}} \, |\mathbf{d_j}\rangle \,, \tag{8}$$

  where $\mathbf{V}$ is the Cabibbo-Kobayashi-Maskawa matrix, a 3×3 unitary matrix, *i.e.* $\mathbf{V}\mathbf{V}^{\dagger} = \mathbf{V}^{\dagger}\mathbf{V} = \mathbf{1}$.
- Neutrinos change their flavor as they propagate, an effect known as neutrino oscillation [32, 33, 36] which implies non-massless neutrinos as the weak eigenstates differ from the mass eigenstates [37]. Nonetheless, the neutrinos masses are tiny, and therefore not considered in the Standard Model.

On the other hand, the neutral current also exhibits peculiar properties that characterize the weak interaction:

- The Z boson and the photon couple to a fermion and its own anti-fermion at tree level. Flavor changing neutral currents are absent at tree level and strongly suppressed in higher order processes in the SM through the GIM mechanism [38].

- The fermionic couplings with the Z boson depend on the electric charge and the weak isospin of the fermions.
- Unlike the photon, the Z boson couplings are different for left-handed and right-handed fermions; the Z boson does not couple with right-handed neutrinos.
- The Z boson lineshape at LEP reveals the existence of three families of light neutrinos [39].

In the previous section, the QED Lagrangian was simply derived using the local $U(1)$ gauge invariance. For the electroweak interaction, the unification between the weak and the electromagnetic interactions is accomplished under the $SU(2)_L \times U(1)$ symmetry group. The $SU(2)$ notation represents the group of 2×2 unitary matrices with determinant 1, *i.e.* the group of matrices that can be written as $U = e^{i\vec{\alpha}\cdot\vec{\tau}/2}$, where $\vec{\tau}$ represents the Pauli matrices:

$$\tau_1 = \begin{pmatrix} 0 & 1 \\ 1 & 0 \end{pmatrix} \quad \tau_2 = \begin{pmatrix} 0 & -i \\ i & 0 \end{pmatrix} \quad \tau_3 = \begin{pmatrix} 1 & 0 \\ 0 & -1 \end{pmatrix}. \tag{9}$$

Thus, for a generic family with up and down quarks, the fermion fields are written as:

$$\psi_1(x) = \begin{pmatrix} u \\ d \end{pmatrix}_L, \quad \psi_2(x) = u_R, \quad \psi_3(x) = d_R, \tag{10}$$

or for a family of leptons:

$$\psi_1(x) = \begin{pmatrix} \nu_l \\ l \end{pmatrix}_L, \quad \psi_2(x) = (\nu_l)_R, \quad \psi_3(x) = l_R^-, \tag{11}$$

where L and R represent the left-handed and right-handed chiralities. The free Dirac Lagrangian for massless fermions,

$$\mathcal{L} = \sum_{j=1}^{3} i\overline{\psi}_j(x) i\gamma^\mu \partial_\mu \psi_j(x), \tag{12}$$

is invariant under global gauge transformation, as in QED,

$$\psi_1(x) \rightarrow \psi_1'(x) = e^{i\vec{\alpha}\cdot\vec{\tau}/2} e^{iy_1\beta} \psi_1(x), \tag{13}$$

$$\psi_2(x) \rightarrow \psi_2'(x) = e^{iy_2\beta} \psi_2(x), \tag{14}$$

$$\psi_3(x) \rightarrow \psi_3'(x) = e^{iy_3\beta} \psi_3(x), \tag{15}$$

where y_j is the weak hypercharge, a conserved quantum number relating the electrical charge and the third component of the weak isospin:

$Q = T_3 + Y/2$. The request for local gauge invariance ($\vec{\alpha} = \vec{\alpha}(x)$ and $\beta = \beta(x)$) of the Lagrangian 12 implies the introduction of a vector ($\vec{W}_\mu$) and a scalar (B_μ) gauge fields, one for each gauge parameter, transforming as:

$$B_\mu(x) \to B_\mu(x)' = B_\mu(x) + \frac{1}{g'}\partial_\mu \beta x, \tag{16}$$

$$\vec{\tau}\cdot\vec{W}_\mu \to \vec{\tau}\cdot\vec{W}'_\mu = U(x)\vec{\tau}\cdot\vec{W}_\mu U^\dagger(x) + \frac{2i}{g}U(x)\partial_\mu U^\dagger(x), \tag{17}$$

where $U(x) = e^{i\vec{\alpha}\cdot\vec{\tau}/2}$. As in QED, the couplings to the B_μ field are arbitrary, however, since the $SU(2)$ commutation relation is non-linear, the constant g must be the same for every coupling. The remaining gauge invariant kinetic terms are given by:

$$\mathcal{L}_K = -\frac{1}{4}B^{\mu\nu}(x)B_{\mu\nu}(x) - \frac{1}{4}\vec{W}^{\mu\nu}(x)\vec{W}_{\mu\nu}(x), \tag{18}$$

where $B^{\mu\nu} = \partial^\mu B^\nu - \partial^\nu B^\mu$ and $\vec{W}^{\mu\nu} = \partial^\mu \vec{W}^\nu - \partial^\nu \vec{W}^\mu + g\vec{W}^\nu \times \vec{W}^\mu$. The gauge invariant Lagrangian under local $SU(2)_L \times U(1)$ trasformations,

$$\mathcal{L} = \sum_{j=1}^{3} i\overline{\psi}_j(x)i\gamma^\mu D_\mu \psi_j(x) - \frac{1}{4}B^{\mu\nu}(x)B_{\mu\nu}(x) - \frac{1}{4}\vec{W}^{\mu\nu}(x)\vec{W}_{\mu\nu}(x), \tag{19}$$

where the covariant derivatives are defined as:

$$D_\mu \psi_1(x) = \left(\partial_\mu - i\frac{g}{2}\vec{\tau}\cdot\vec{W}_\mu(x) - ig' y_1 B_\mu\right)\psi_1(x), \tag{20}$$

$$D_\mu \psi_2(x) = \left(\partial_\mu - ig' y_2 B_\mu\right)\psi_2(x), \tag{21}$$

$$D_\mu \psi_3(x) = \left(\partial_\mu - ig' y_3 B_\mu\right)\psi_3(x). \tag{22}$$

The Lagrangian 19 only contains massless gauge fields and massless fermions at this point, because the mass terms explicitly violate the gauge symmetry. The Higgs mechanism, which generates the mass of particles through electroweak symmetry breaking, is explained in section ... .

1.2.3 Gauge Bosons

The interaction between fermions and the gauge bosons is included in Lagrangian 19 by:

$$\mathcal{L} = \sum_{j=1}^{3} \frac{g}{2}\overline{\psi}_j(x)i\gamma^\mu(\vec{\tau}\cdot\vec{W}_\mu)\psi_j(x) + g' y_j B_\mu \overline{\psi}_j(x)i\gamma^\mu \psi_j(x), \tag{23}$$

where:

$$\vec{\tau}\cdot\vec{W}_\mu = \begin{pmatrix} W^3_\mu & W^1_\mu - iW^2_\mu \\ W^1_\mu + iW^2_\mu & -W^3_\mu \end{pmatrix}. \tag{24}$$

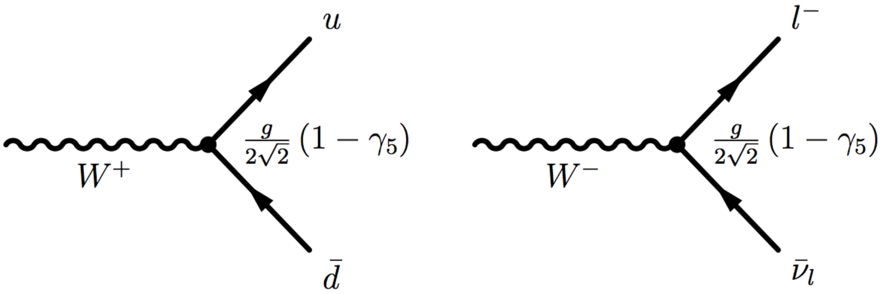

Figure 1: Charged current interaction vertices.

Therefore, the charged current sector of the weak interaction for three families of quarks and leptons, except for the quark mixing matrix, is written as:

$$\mathcal{L}_{CC} = \frac{g}{2\sqrt{2}} W_\mu^\dagger \left(\sum_j \overline{u}_j \gamma^\mu (1-\gamma_5) d_j + \overline{\nu}_j \gamma^\mu (1-\gamma_5) l_j \right) + h.c. \quad (25)$$

where the term $(1-\gamma^5)$ has been included to take into account the parity violation [?]. The charged current interaction vertices are shown in Figure 1.

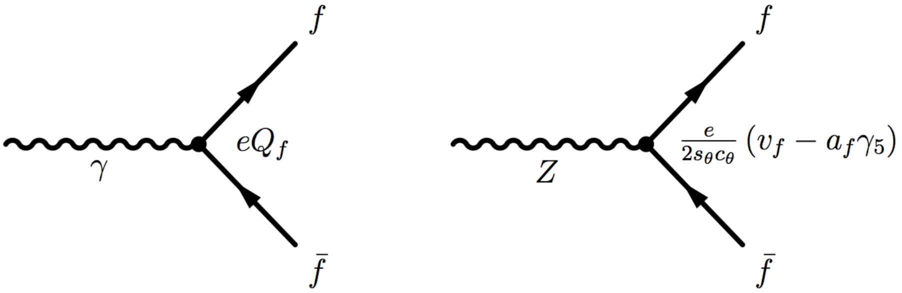

Figure 2: Neutral current interaction vertices.

The remaining gauge fields, W_μ^3 and B_μ, can be written as:

$$\begin{pmatrix} W_\mu^3 \\ B_\mu \end{pmatrix} = \begin{pmatrix} \cos\theta_W & \sin\theta_W \\ -\sin\theta_W & \cos\theta_W \end{pmatrix} \begin{pmatrix} Z_\mu \\ A_\mu \end{pmatrix}, \quad (26)$$

	ν_L^l	l_L^-	l_R^-	u_L	d_L	u_L	d_L
Q	0	-1	-1	$2/3$	$-1/3$	$2/3$	$-1/3$
T_3	$1/2$	$-1/2$	0	$1/2$	$-1/2$	0	0
Y	$-1/2$	$-1/2$	-1	$1/6$	$1/6$	$2/3$	$-1/3$

Table 1: Electroweak charges Q, Y and the third component of the weak isospin T_3 for quarks and leptons in the SM.

where Z_μ and A_μ represent the Z boson and photon fields, respectively, and θ_W is the weak mixing angle. As a result, the Lagrangian for the neutral current sector of the weak interaction is given by:

$$\begin{aligned}\mathcal{L}_{NC} = &\sum_j \overline{\psi}_j(x) i\gamma^\mu \left(\frac{g}{2}\tau_3 \sin\theta_W + g^{'} y_j \cos\theta_W\right) A_\mu \psi_j \\ &+ \sum_j \overline{\psi}_j(x) i\gamma^\mu \left(\frac{g}{2}\tau_3 \cos\theta_W - g^{'} y_j \sin\theta_W\right) Z_\mu \psi_j + h.c., \end{aligned} \tag{27}$$

which successfully recreates QED if, and only if, $g \sin\theta_W = g^{'} \cos\theta_W = e$, and $Y = Q - T_3$, where $T_3 = \tau_3/2$ and Q is the electromagnetic charge operator.

The electroweak charges Q, Y, and the third component of the weak isospin, T_3, for leptons and quarks are collected in Table1. The right-handed neutrino is not considered in this table since it has no electric charge nor weak hypercharge (sterile neutrino). In Figure 2 the neutral current interaction vertices are shown. The final Lagrangian for neutral current can be written as:

$$\begin{aligned}\mathcal{L}_{NC} &= \mathcal{L}_{QED} + \mathcal{L}_Z \\ &= eA_\mu \sum_f \overline{f}\gamma^\mu Q_f f + \frac{e}{2\sin\theta_W \cos\theta_W} Z_\mu \sum_f \overline{f}\gamma^\mu (v_f - a_f\gamma_5) f,\end{aligned} \tag{28}$$

where the vectorial and axial couplings, v_f and a_f, respectively, are presented in Table2 for quarks and leptons.

The self-interaction terms among the gauge fields can be taken into account considering the cubic and quadratic terms generated by the Lagrangian 18. The Feynman graphs for these self-interactions are shown in Figure 3.

1.2.4 Higgs Mechanism

The electroweak interaction Lagrangian, derived in the previous sections, is still far from reality since it only contains massless gauge

	u	d	ν_L	l
v_f	$\left(1-\frac{8}{2}\sin^2\theta_W\right)/2$	$\left(-1+\frac{4}{3}\sin^2\theta_W\right)/2$	$1/2$	$\left(-1+4\sin^2\theta_W\right)/2$
a_f	$1/2$	$-1/2$	$1/2$	$-1/2$

Table 2: Neutral current couplings.

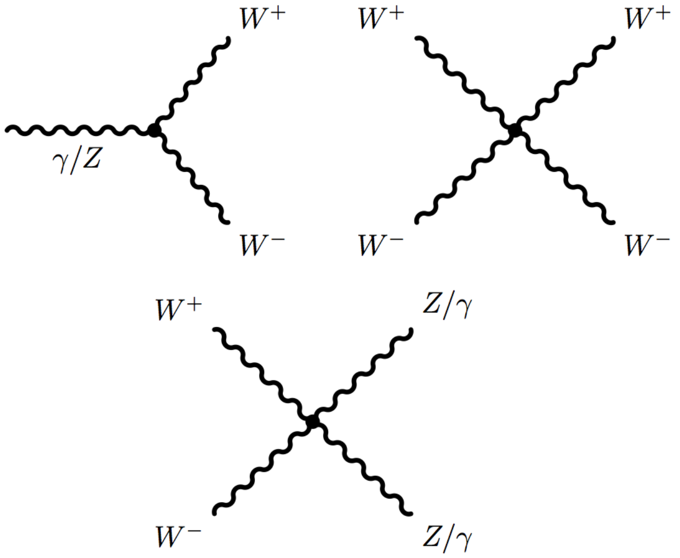

Figure 3: Gauge boson self-interaction vertices..

fields and fermions. The Higgs mechanism allows to generate the masses of the $W^{\pm}$ and Z gauge bosons through spontaneous symmetry breaking, by postulating the existence on a new compilex scalar field doublet. The Higgs mechanism was independently suggested in 1964 by Robert Brout and Francois Englert [4], Peter Higgs [5], and Gerald Guralnik, C. R. Hagen, and Tom Kibble [6], and is the generally accepted renormalizable model which spontaneously breaks the electroweak symmetry. The six authors of the 1964 PRL symmetry breaking papers were awarded the J. J. Sakurai Prize for Theoretical Particle Physics in 2010, by the American Physical Society, "for elucidation of the properties of spontaneous symmetry breaking in four-dimensional relativistic gauge theory and of the mechanism for the consistent generation of vector boson masses".
The Higgs boson field is written as an $SU(2)$ doublet with twon scalar components:

$$\Phi = \begin{pmatrix} \phi^{+} \\ \phi^{0} \end{pmatrix} = \begin{pmatrix} \frac{1}{\sqrt{2}}\phi^{1} + i\phi^{2} \\ \frac{1}{\sqrt{2}}\phi^{3} + i\phi^{4} \end{pmatrix}. \tag{29}$$

The Lagrangian for such a boson field is written as:

$$\mathcal{L}_H = (D^{\mu}\Phi)^{\dagger}D_{\mu}\Phi - V\Phi = (D^{\mu}\Phi)^{\dagger}D_{\mu}\Phi - \mu^2\Phi^{\dagger}\Phi - \lambda(\Phi^{\dagger}\Phi)^2. \tag{30}$$

The ground state of the potential, V, is particularly interesting if $\mu^2 < 0$: the minimum of the potential is not unique anymore, but it is located on a continuous ring on a complex plane, as seen in Figure 4. This configuration of is invariant under symmetry group transformation but different configurations of minimum exist: the symmetry is spontaneously broken when a particular minimum is choosen. An easier form of scalar potential can be choosen as:

$$\Phi = \begin{pmatrix} 0 \\ \phi(x) \end{pmatrix}, \tag{31}$$

with $\phi(x)$ real. The degree of freedom in the Higgs field that are removed by this transformation can be absorbed into three longitudinal degrees of freedom of the new massive bosons.
There is therefore a degree of freedom for the choice of Higgs vacuum expectation value:

$$\Phi_0 = \begin{pmatrix} 0 \\ v/\sqrt{2} \end{pmatrix}, \tag{32}$$

where $v = \sqrt{-\mu^2/\lambda}$. The scalar field Φ can be expanded around the minimum in the most general form:

$$\Phi = \frac{1}{\sqrt{2}} \begin{pmatrix} 0 \\ v + H(x) \end{pmatrix}, \tag{33}$$

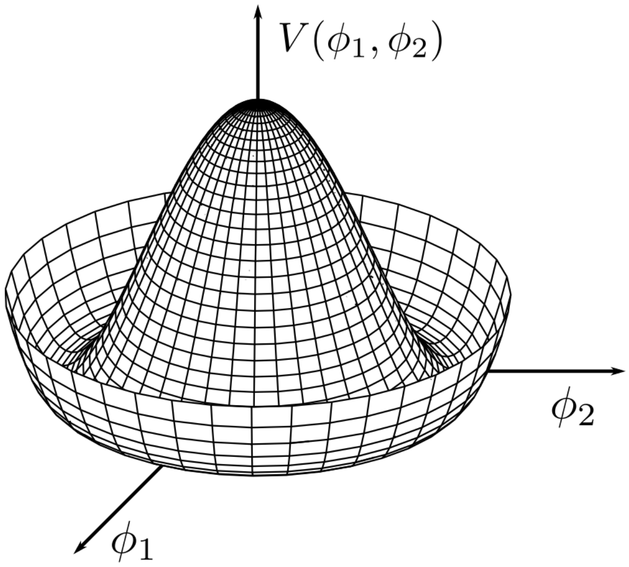

Figure 4: Graph of a mexican hat potential function.

$v/\sqrt{2}$ is the Higgs vacuum expectation value and $H(x)$ is the fluctuation around the minimum. After breaking symmetry, the kinetic term of the Lagrangian becomes:

$$\begin{aligned}(D^\mu\Phi)^\dagger D_\mu\Phi =& \frac{1}{2}\partial^\mu H \partial_\mu H \\ &+ (v+H)^2\left(\frac{g^2}{4}W_\mu^\dagger W^\mu + \frac{g^2}{8\cos^s\theta_W}Z_\mu Z^\mu\right). \end{aligned} \tag{34}$$

This describes three massive gauge bosons (rather than three massless bosons as assumed up to now) and one massive gauge boson:

$$m_H = \sqrt{2}\mu = \sqrt{2v} \tag{35}$$

$$m_W = \frac{1}{2}gv \tag{36}$$

$$m_Z = \frac{1}{2}v\sqrt{g^2 + g'^2} = \frac{m_W}{\cos\theta_W}. \tag{37}$$

The photon remains to be massless, that is to say, the $U(1)$ symmetry remains unbroken under the gauge subgroup generated by the electric charge.

The fermionic masses are also allowed after the spontaneous symmetry breaking, and the Yukawa-type Lagrangian takes the following form:

$$\mathcal{L}_H = -\left(1 + \frac{H}{v}\right)(m_u\bar{u}u + m_d\bar{d}d + m_e\bar{e}e). \tag{38}$$

On 4th July 2012, the CMS and ATLAS experiments announced the discovery of a new boson, compatible with the SM Higgs boson, at

$125.3 \pm 0.4 \pm 0.5$ GeV (CMS) and $126 \pm 0.4 \pm 0.4$ GeV (ATLAS), with global statistical significances of 5.8σ (CMS) [40] and 5.9σ (ATLAS) [41].

1.2.5 CP Violation and CKM Matrix

The CP-symmetry corresponds to the combination of the C-symmetry, and the P-symmetry. Since the discovery of parity violation in the 1950s [28, 29], the CP-symmetry was believed to be the true symmetry of the Standard Model. However, the discovery of the CP violation in the weak decays of neutral kaons, by James Cronin and Val Fitch in 1964 [42], forced a reformulation of the electroweak sector of the Standard Model. The Cabibbo-Kobayashi-Maskawa (CKM) matrix, which contains the information on the strength of flavor-changing weak decays, and explains the observed CP violation in the context of a renormalizable theory of the weak interaction, is presented in this section.

It is now almost fifty years since the publication of Nicola Cabibbo's famous letter "Unitary Symmetry and Leptonic Decays" [30], which provided the basic foundation for quark mixing in the weak interaction sector of the Standard Model. Ten years later, Makoto Kobayashi and Toshihide Maskawa extended the work of Cabibbo to three generations of quarks and established the unitary CKM matrix [31]. The work of Kobayashi and Maskawa became notorious for explaining CP violation in the Standard Model, and for predicting the existence of the bottom and top quarks [43, 45]. In recognition of their work, the two japanese physicists were laureated with the Nobel Prize in Physics in 2008 "for the discovery of the origin of the broken symmetry which predicts the existence of at least three families of quarks in nature".

The charged current sector for the quarks in the Standard Model Lagrangian, i.e. the V-A coupling to the W boson, can be written in terms of mass eigenstates as:

$$\mathcal{L}_{CC} = -\frac{g}{2\sqrt{2}} W^{\dagger}_{\mu} \sum_{ij} \overline{u}_i \gamma^{\mu} (1 - \gamma_5) V_{ij} d_j + h.c. \tag{39}$$

where i and j are the quark generation indices and V is the CKM matrix, which relates the down-type weak eigenstates, $|d'_i\rangle$, to the mass eigenstates, $|d_j\rangle$:

$$|d'_i\rangle = \sum_j V_{ij} \, |d_j\rangle \, , \tag{40}$$

expliciting the quark generations:

$$\begin{pmatrix} |d'\rangle \\ |s'\rangle \\ |b'\rangle \end{pmatrix} = \begin{pmatrix} V_{ud} & V_{us} & V_{ub} \\ V_{cd} & V_{cs} & V_{cb} \\ V_{td} & V_{ts} & V_{tb} \end{pmatrix} \begin{pmatrix} |d\rangle \\ |s\rangle \\ |b\rangle \end{pmatrix} , \tag{41}$$

so that each up-type quark couples with every down-type quark by means of the CKM matrix, a 3×3 unitary matrix with four independent parameters.

Assuming unitarity and the existence of three quark families, the best determination of the CKM matrix elements magnitudes is [?]:

$$\begin{pmatrix} 0.97428 \pm 0.00015 & 0.2253 \pm 0.0007 & 0.00347^{+0.00016}_{-0.00012} \\ 0.2252 \pm 0.0007 & 0.97345^{+0.00015}_{-0.00016} & 0.0410^{0.0011}_{-0.0007} \\ 0.00862^{+0.00026}_{-0.00020} & 0.0403^{+0.0011}_{-0.0007} & 0.999152^{0.000030}_{-0.000045} \end{pmatrix}. \quad (42)$$

1.3 QUANTUM CHROMODYNAMICS

Quantum Chromodynamics, a theory of the strong force that describes how the constituents of hadrons (quarks and gluons) interact, assumes the existence of a new quantum number, the color charge. Quarks can hold three different colors (red, green, blue), however, only appear in colorless bound states (hadrons), *i.e.* color singlets, an features known as confinement [10].

The first, not understood, evidence of the color was given in 1969 by the observation of the experiments ad ADONE. They observed that the hadronic production was substantially larger than expected. However, at the time quarks had not yet been accepted as physical entities and a correct theoretical interpretation was impossible. In retrospect, since the u, d and s quarks are produced at the ADONE energies ($1.6 < \sqrt{s} < 3$ GeV), the expected value of R[1] is $2/3$, whilst the experiments indicated values between $1 \div 3$. Actually, the quarks of every flavour come in three types, each with a different colour. Consequently R is three times larger, as shown in Figure 5.

Since there are three color states, $SU(3)_C$ is the natural gauge symmetry group for QCD. The free Dirac Lagrangian for massive quarks,

$$\mathcal{L} = \sum_f \bar{q}_f (i\gamma^\mu \partial_\mu - m_f) q_f, \quad (43)$$

where $q_f^i = (q_f^1, q_f^2, q_f^3)$ is the quarks color vector of flavor f, is invariant under global $SU(3)_C$ transformations:

$$q_f^\alpha \to (q_f^\alpha)' = U^\alpha_\beta q_f^\beta, \quad (44)$$

where $U = e^{i\lambda^a \theta_a/2}$, satisfying $U^\dagger U = 1$ and $\det U = 1$. The matrices λ^a, for $a = 1, 2, ..., 8$ known as Gell-Mann matrices [7], represent the

---

[1] R is the ratio between the total hadronic e^+e^- cross section and the $e^+e^- \to \mu^+\mu^-$ cross section, namely: $R = \frac{\sigma(e^+e^- \to hadrons)}{\sigma(e^+e^- \to \mu^+\mu^-)}$. If the quarks are point-like, without any structure, this ratio is simply given by the ratio of the sum of the electric charges, $R = \sum_i q_i^2/1$, where the sum is over the quark flavours with production above threshold.

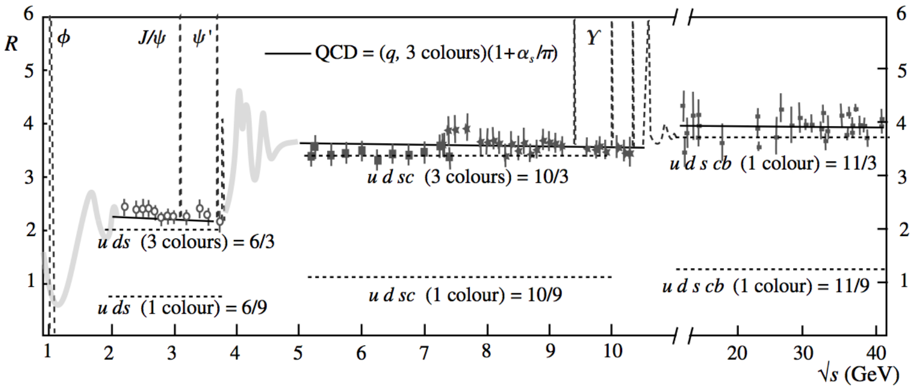

Figure 5: Ratio R of hadronic to point-like cross section in e^+e^- annihilation as a function of $\sqrt{s}$. [?]

$SU(3)$ group generators, and θ_a are argitrary parameters. The Gell-Mann matrices are traceless and satisfy the following commutation relation:

$$\left[\frac{\lambda^a}{2}, \frac{\lambda^b}{2}\right] = i f^{abc} \frac{\lambda^c}{2} \tag{45}$$

where the structure constants f^{abc} are completely antisymmetric. In order to preserve the local gauge symmetry, $\theta^a = \theta^a(x)$, the covariant derivative is defined as:

$$D^\mu q_f = \left(\partial^\mu + i g_s \frac{\lambda^a}{2} G^\mu_a(x)\right) q_f = (\partial^\mu + i g_s G^\mu(x)), \tag{46}$$

where $G^\mu(x) = \frac{1}{2}\lambda^a G^\mu_a(x)$, and trasforms as,

$$G^\mu(x) \to (G^\mu(x))' = U G^\mu U^\dagger + \frac{i}{g_s}(\partial^\mu U)U^\dagger. \tag{47}$$

Finally, the gauge-invariant kinetic term for the gluon fields is,

$$\mathcal{L}_K = \frac{1}{4} G^{\mu\nu}_a G^a_{\mu\nu}, \tag{48}$$

where $G^{\mu\nu}_a = (\partial^\mu G^\nu_a - \partial^\nu G^\mu_a)(\partial_\mu G^a_\nu - \partial_\nu G^a_\mu) - g_s f^{abc} G^\mu_b G^\nu_c$. Consequently, the final QCD Lagrangian can be written as,

$$\begin{aligned}
\mathcal{L}_K = {} & \frac{1}{4}(\partial^\mu G^\nu_a - \partial^\nu G^\mu_a)(\partial_\mu G^a_\nu - \partial_\nu G^a_\mu) + \sum_f \overline{q}_f (i\gamma^\mu \partial_\mu - m_f) q_f \\
& - g_s G^\mu_a \sum_f \overline{q}^\alpha_f \gamma^\mu \left(\frac{\lambda^a}{2}\right)_{\alpha\beta} q^\beta_f \\
& + \frac{g_s}{2} f^{abc} (\partial^\mu G^\nu_a - \partial^\nu G^\mu_a) G^\mu_b G^\nu_c - \frac{g_s^2}{4} f^{abc} f_{ade} G^\mu_b G^\nu_c G^d_\mu G^e_\nu,
\end{aligned} \tag{49}$$

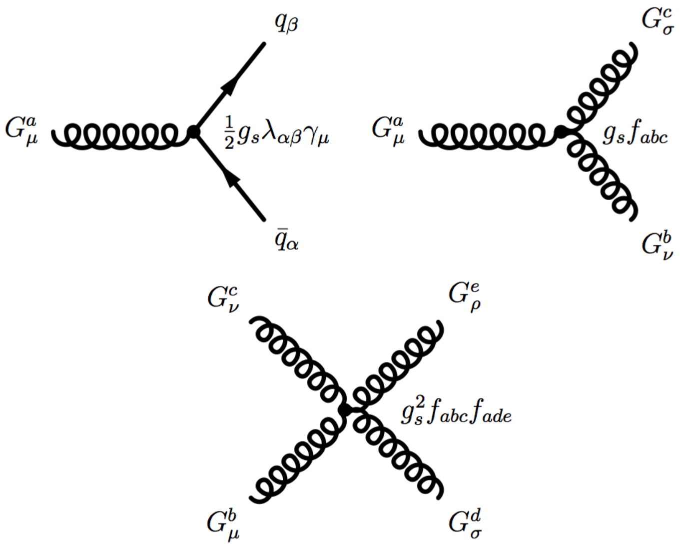

Figure 6: QCD interaction vertices.

which contains the color interaction between quarks and gluons, and the cubic and quartic gluon self-interactions, corresponding to the Feynman diagrams shown in Figure 6.

2 THE CMS EXPERIMENT AT LHC

2.1 THE LARGE HADRON COLLIDER

The Large Hadron Collider (LHC) is a particle accelerator and collider at the European Organization for Nuclear Research (CERN) near Geneva, Switzerland. The LHC is designed to accelerate bunches of either protons or heavy ions and bring them to collision at the centres of four particle detectors with a centre of mass energy up to $\sqrt{s} = 14$ TeV. The LHC physics program is broad and diverse, ranging from precise measurements of Standard Model (SM) parameters to the search for new physics phenomena. One of its main goals is establishing the origin of the electroweak symmetry breaking, either by discovering the SM Higgs boson and measuring its properties or excluding it and looking for evidence for alternative mechanisms. It also enables searches for physics beyond the SM that could appear at the TeV scale, such as supersymmetrical particles, new heavy gauge bosons, technicolor particles or extra dimensions. The LHC is thoroughly described in [47].

2.2 LHC: AN OVERVIEW

The LHC is a circular accelerator. This topology allows the particles to be indefinitely recirculated through the accelerating sections, thus allowing to reach very high energies while keeping a relatively compact design. The highest energy accelerators that preceded the LHC, the LEP (Large Electron Positron) lepton synchrotron and the Tevatron hadron synchrotron were both circular accelerators. The LEP collided electrons with positrons at a centre of mass energy of up to $\sqrt{s} = 209$ GeV, while the Tevatron collided protons with antiprotons at a centre of mass energy of up to $\sqrt{s} = 1.96$ TeV. A striking drawback of the circular design is the loss of energy via synchrotron radiation: charged particles in circular motion emit electromagnetic radiation due to the acceleration produced by the bending of the beams. The power emitted can be expressed as:

$$P = \frac{e^2 c}{6\pi\epsilon_0 R^2}\gamma^2 = \frac{e^2 c}{6\pi\epsilon_0 R^2}\frac{E^4}{(mc^2)^4} \tag{50}$$

where ϵ_0 is the vacuum permittivity, γ is the relativistic gamma factor, R is the radius of the circle, E, m and e are respectively the energy, mass and charge of the particle. One can obtain the lost energy per revolution writing:

$$\Delta E = PT = P\frac{2\pi R}{v} = \frac{e^2}{3\epsilon_0 R}\frac{E^4}{(mc^2)^4}\frac{c}{v} \approx \frac{e^2}{3\epsilon_0 R}\frac{E^4}{(mc^2)^4} \tag{51}$$

where the ultra-relativistic approximation is used to consider the particle speed $v \approx c$. The quartic dependence of this quantity on the particle energy, compared to the only linear dependency on the inverse accelerator radius, makes a TeV scale circular electron collider absolutely infeasible. To obtain a crude estimate one can take the 26.7 km long LEP tunnel as an example, considering it a perfect circle. Electrons at $\sqrt{s}/2 = 104.5$ GeV would approximately lose 2.5 GeV per revolution, i.e. 4.2% of the energy. Even a modest twofold increase in electron energy would increase synchrotron losses per revolution by a factor of 16, bringing them to 33.6% of the particle energy. It is not realistically possible to compensate such losses simply increasing the accelerator radius. The alternative is to use particles with a higher mass instead. The proton's mass is three orders of magnitude greater than the electron's. In this case, in the same LEP tunnel length and with a particle energy of 7 TeV the losses would be limited to a negligible 4 keV.

In order to pursue the goals of the LHC physics programme, extremely rare processes need to be studied. Figure 7 helps quantifying what "extremely rare processes" means, showing the cross sections of various processes at a hadron collider. As a significant example, the cross section for a "light" SM Higgs (with mass $M_H = 150$ GeV) is 10 order of magnitude smaller than the total hadron-hadron cross section.

The number of events per second generated in a collider via a given process is given by:

$$N = L\sigma \tag{52}$$

where σ is the cross section for the process under study and L the machine luminosity, which depends only on the beam parameters. The LHC was therefore designed to provide collisions with an unprecedented peak instantaneous luminosity of $L = 10^{34}$ cm^{-2}s^{-1}. At this luminosity, a light Higgs boson event would occur with an average frequency of ≈ 0.25 Hz. As a comparison, at the maximum luminosity obtained at the Tevatron, $L = 5 \cdot 10^{32}$ cm^{-2}s^{-1}, a light Higgs boson event would only occur with an average frequency of the order of 10^{-4} Hz.

A circular collider's luminosity can be written as:

$$L = \frac{N_1 N_2 n_b f_{rev} \gamma}{4\pi\epsilon_n \beta^*} F \tag{53}$$

where N_1 and N_2 are the numbers of particles per bunch in each beam, n_b is the number of bunches per beam, f_{rev} in the revolution frequency,

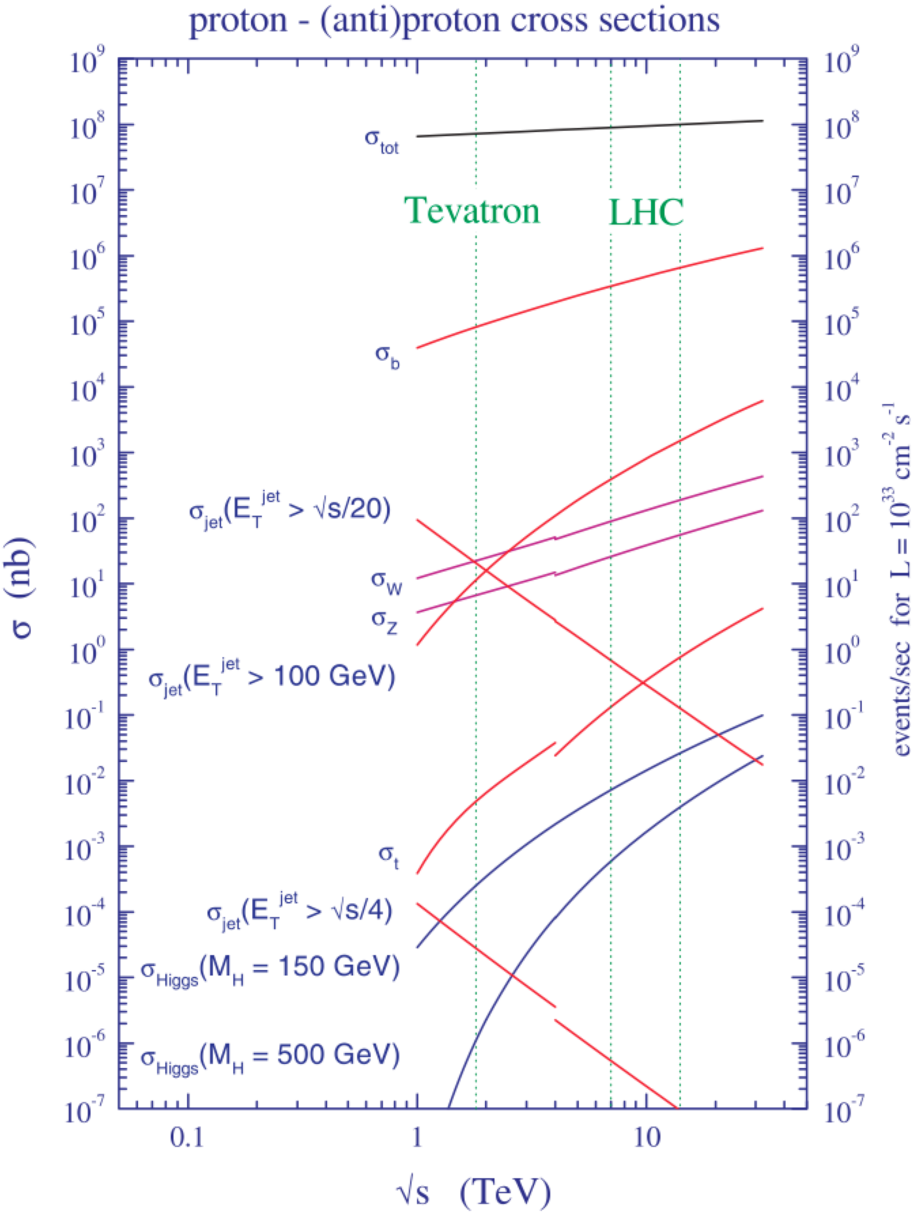

Figure 7: Various Standard Model cross-sections at the Tevatron and LHC colliders as function of the centre-of-mass energy ($\sqrt{s}$), []

γ is the relativistic gamma factor for particles in the beam, ϵ_n is the normalized beam emittance which give a measure of how much the particles depart from the ideal trajectory, β^* is the beta function at the collision point giving the envelope for the particles' motion and F is the luminosity reduction factor due to the crossing angle at the interaction point. f_{rev} and γ are determined by collider radius and particle energy while all the other parameters may be controlled to maximize the luminosity.

2.3 DESIGN AND NOMINAL PARAMETERS

The LHC is housed in the aforementioned tunnel which the LEP collider occupied until 2000. It uses superconducting resonating cavities to accelerate the two counter-rotating proton beams and superconducting magnets to bend them.

The necessity for high luminosities dictated the decision to collide protons with protons instead of antiprotons as done e.g. at the Tevatron. While using antiprotons would have enabled a simplified collider configuration of a common vacuum and magnet system for both counter-rotating beams, antiproton production and storage are challenging processes. They would have imposed significant limits on the total number of particles in the antiproton beam, N_2 in equation **??** , thus bounding the maximum luminosity. Therefore two proton beams are used, each controlled by separate magnets.

The 26.7 km long tunnel straddles the French-Swiss border near Geneva; it lies between 45 m and 170 m underground and consists of eight straight sections, each about 528 m long, and eight arcs. This shape was necessary for LEP to accommodate long straight accelerating sections to compensate the high synchrotron radiation losses discussed in section **??**. The LHC would have longer arcs and shorter straight sections for the same circumference, thus requiring less intense magnetic fields to bend the beams. However reusing the existing tunnel was clearly the most cost-effective option. The straight sections serve as insertion regions: four of them house physics experiments, one the acceleration system, one the beam dump and the remaining two the beam cleaning systems. The arcs are occupied by magnets and the systems to make them functional. The overall layout of the tunnel is shown in figure 8.

Due to space constraints in the tunnel the LHC uses twin bore magnets that consist of two sets of coils and beam channels within the same mechanical structure and cryostat. Each arc consists of 23 cells, each one composed of dipoles for deflecting and quadrupoles for focusing the bunches. In order to focus the beam in both planes, a series of focusing and defocusing quadrupoles is arranged. In total there are 1232 main dipoles and 392 quadrupoles. In addition, sextupole, octupole and decapole corrector magnets are positioned to correct errors in the particle trajectory.

In this geometry structure the bending radius of the dipoles is about 2.8 km. The magnetic field needed to keep 7 TeV protons on a circular trajectory can be calculated as:

$$B = \frac{p}{e\rho} \tag{54}$$

where $p = \sqrt{E^2 - m^2}$ is the proton's momentum and ρ is the bending radius. Thus one obtains a peak dipole field of 8.33 T. Producing such a high field using a conventional electromagnet is unfeasible, due to extremely high currents and consequent heat dissipation. The LHC therefore uses superconducting magnets. In particular the magnet coils are made of niobium-titanium alloy, a superconductor with a critical temperature of 9.2 K. The coolant used is super-fluid helium at 1.9 K. Helium becomes super-fluid at 2.17 K. Super-fluid helium has the highest thermal conductivity of any known substance, making it a very good choice as a coolant. In this state it is also characterized by a complete absence of viscosity, which enables it to penetrate in the complex shape of the coils. The high-field super-conducting magnets operate in a static bath of pressurized super-fluid helium at 1.9 K, cooled by continuous heat exchange with flowing super-fluid helium.

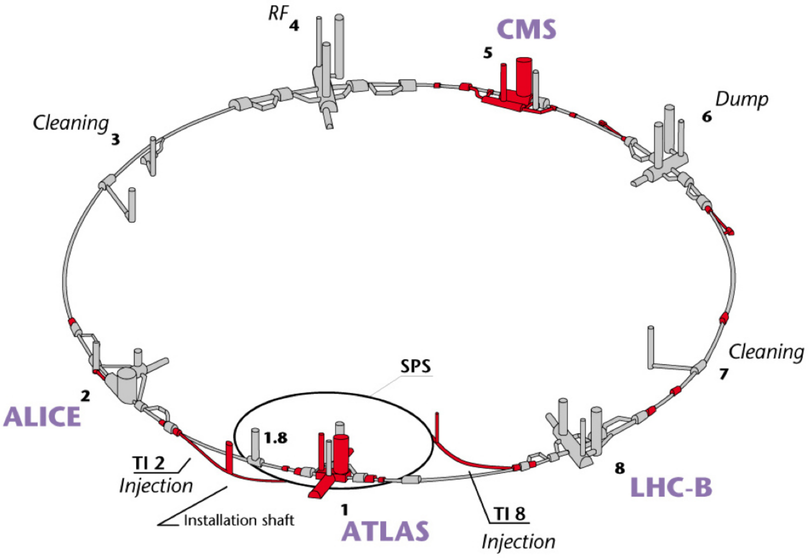

Figure 8: Layout of the LHC tunnel [48]. The red parts are new underground buildings built specifically for LHC. The grey parts represent existing LEP infrastructure.

Before reaching the LHC, the particles are accelerated by a chain of accelerators that gradually increase the particles' energy. The protons start their journey to the LHC in the linear accelerator Linac2. This accelerator yields protons with an energy of 50 MeV which are then injected into the first circular accelerator of the chain, the Proton Synchrotron Booster (PSB), which increases the energy to 1.4 GeV. The protons are then transferred to the Proton Synchrotron (PS), that raises the energy to 25 GeV and organises them in bunches with about $1.15 \cdot 10^{11}$ particles each. From the PS the beam is injected into the Super Proton Synchrotron (SPS) where the energy of the bunches increases by a factor of almost 20 up to 450 GeV, which is the injection energy of the LHC.

The LHC acceleration system consists of 8 radio-frequency (RF) superconducting resonating cavities per each beam, that supply the protons with about 485 keV per revolution during the ramp phase from 450 GeV to 7 TeV. The RF cavities operate at a peak voltage of 2 MV at a frequency of approximately 400 MHz. This results in 35640 potential wells in the RF field, so-called RF buckets, where it is energetically favourable for the bunches to be located in the beam. This corresponds to a spacing in time of only 2.5 ns, but only every tenth RF bucket is used, making the minimum bunch spacing $\Delta t = 25\text{ns}$. The LHC therfore has $N_B = 3564$ possible locations, called buckets, where bunches can sit for each beam. The bunch patterns of the two counter-rotating beams together determine when there will be collisions in the the centre of the experiments. After acceleration the beams circulate in the machine for a period of typically 10-20 hours during which they are brought into collision.

In high-luminosity colliders, there is a non-negligible probability that one single bunch crossing may produce several separate events, a phenomenon known as pileup. The average number of superimposed events can be estimated as:

$$\mu = L\sigma_{pp}\overline{\Delta t} \tag{55}$$

where $\overline{\Delta t} = \Delta t \cdot (N_B/N_b)$ is the average bunch spacing. Assuming a proton-proton inelastic cross section of $\sigma_{pp} \approx 80$ mb [49], one obtain $\mu = 25$.

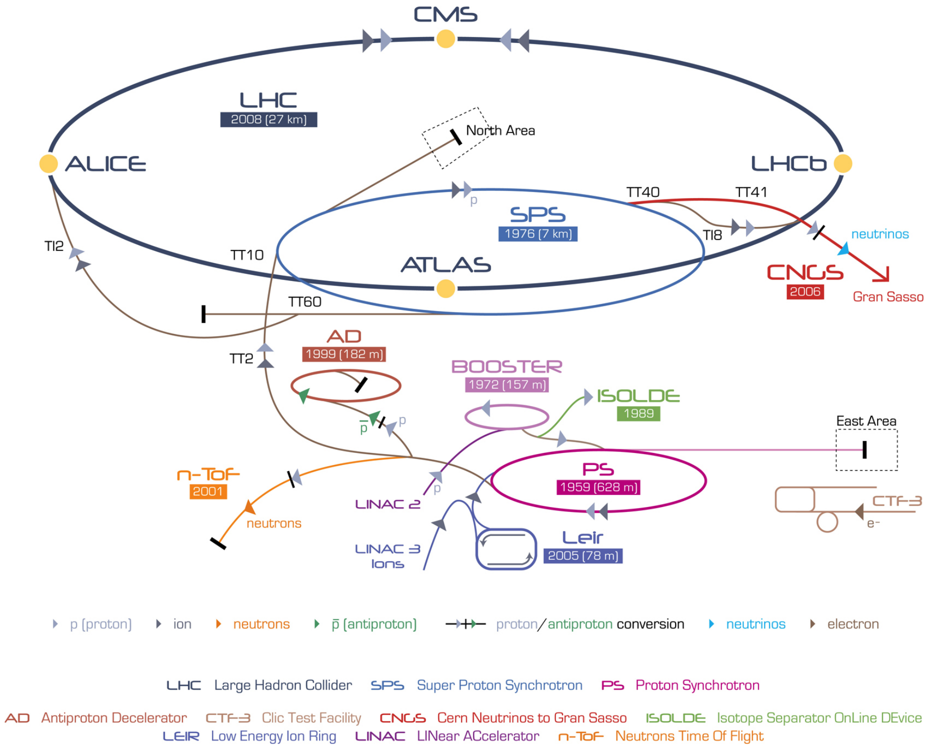

Figure 9: The CERN Accelerator Complex.

2.4 EXPERIMENTS

At the LHC experimental interaction points, four particle detectors reconstruct the collision events to perform detailed studies of known physics processes and to search for evidence of new physics. Two of them, ATLAS [50] and CMS [51], are general purpose detectors; ALICE [52] is dedicated to the study of the quark-gluon plasma, which is postulated to have existed during the early universe, using lead-ion collisions; LHCb [53] is targeted towards studying the decays of B hadrons in order to better understand the matter-antimatter asymmetry in the universe.

2.5 THE CMS EXPERIMENT

The Compact Muon Solenoid [51] is one of the two "general purpose" detectors at the Large Hadron Collider. Its aim is to study a large spectrum of physical phenomena, starting from the completion of the Standard Model predictions looking for the Higgs Boson and up to the search for new physics beyond the Standard Model at the TeV scale. The experiment is located in an underground cavern at LHC experimental point number five, near the french town of Cessy. The main feature of the detector is a strong super-conductive solenoidal magnet, which can reach a 4 T field and dictates the cylindrical shape of the experiment. Another characteristic of CMS is its modularity. This had made it possible to build CMS on surface, while the experimental cavern was being excavated, and it was lowered one section at the time in 2007. The magnet occupies the central region of the detector, called barrel, which is externally subdivided in 5 wheels. The wheels compose the iron yoke for the return of the magnetic fields, and contain the chambers for the detection of muons. The central wheel (designated wheel 0) is also the structural support for the magnet to which it's connected. The barrel region is closed on both ends by three instrumented iron disks called endcaps. Once closed, the detector is quite compact (at least with respect to ATLAS), being a cilinder 21.6 m long and with a diameter of 14.6 m. Its total weight is of about 14500 tons. In Figure 10 an expanded section of the CMS detector is shown, with highlighted the main sub-detectors.

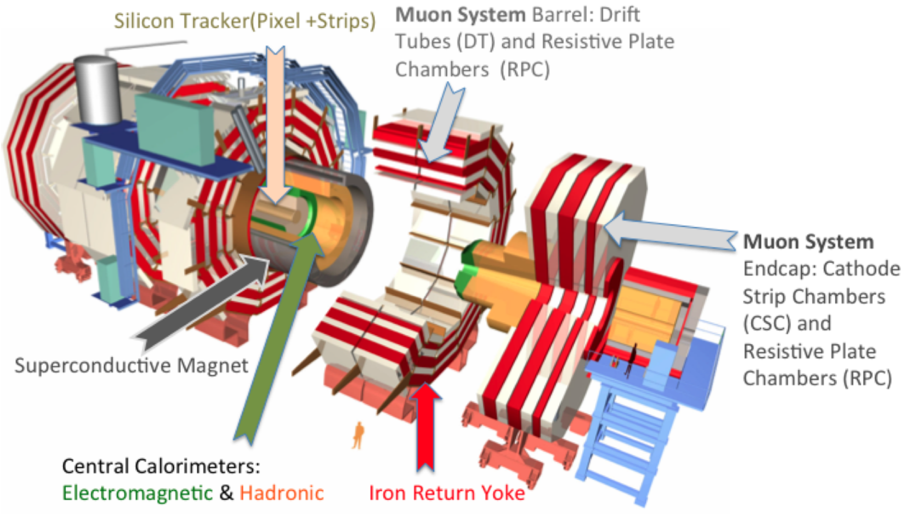

Figure 10: CMS schematic layout.

2.6 CMS COORDINATE SYSTEM

The CMS coordinate system used to describe the detector is a right-handed Cartesian frame, centred in the interaction point and with the z axis along the beam line (this direction is referred to as *longitudinal*). The x axis is chosen to be horizontal and pointing towards the centre of the LHC ring, and the y axis is vertical and pointing upwards. The $x - y$ plane is called *transverse* plane.
Given the cylindrical symmetry of the CMS design, usually a (ϕ, θ) cylindrical coordinate system is used in the reconstruction of the tracks of particles. ϕ is the polar angle, laying in the $x - y$ plane, measured from the x-axis in mathematical positive direction (i.e. the y axis is at $\phi = 90°$. The azimuthal angle θ is measured from the z-axis towards the $x - y$ plane. The angle θ can be translated into the pseudo-rapidity η by:

$$\eta = -\ln\left(\tan\frac{\theta}{2}\right) \tag{56}$$

A longitudinal view of CMS detector displaying the segmentation η of the sub-detectors is shown in Figure 11.
Using these parameters, a distance between two particle directions can be defined as

$$\Delta R = \sqrt{\Delta\phi^2 + \Delta\eta^2} \tag{57}$$

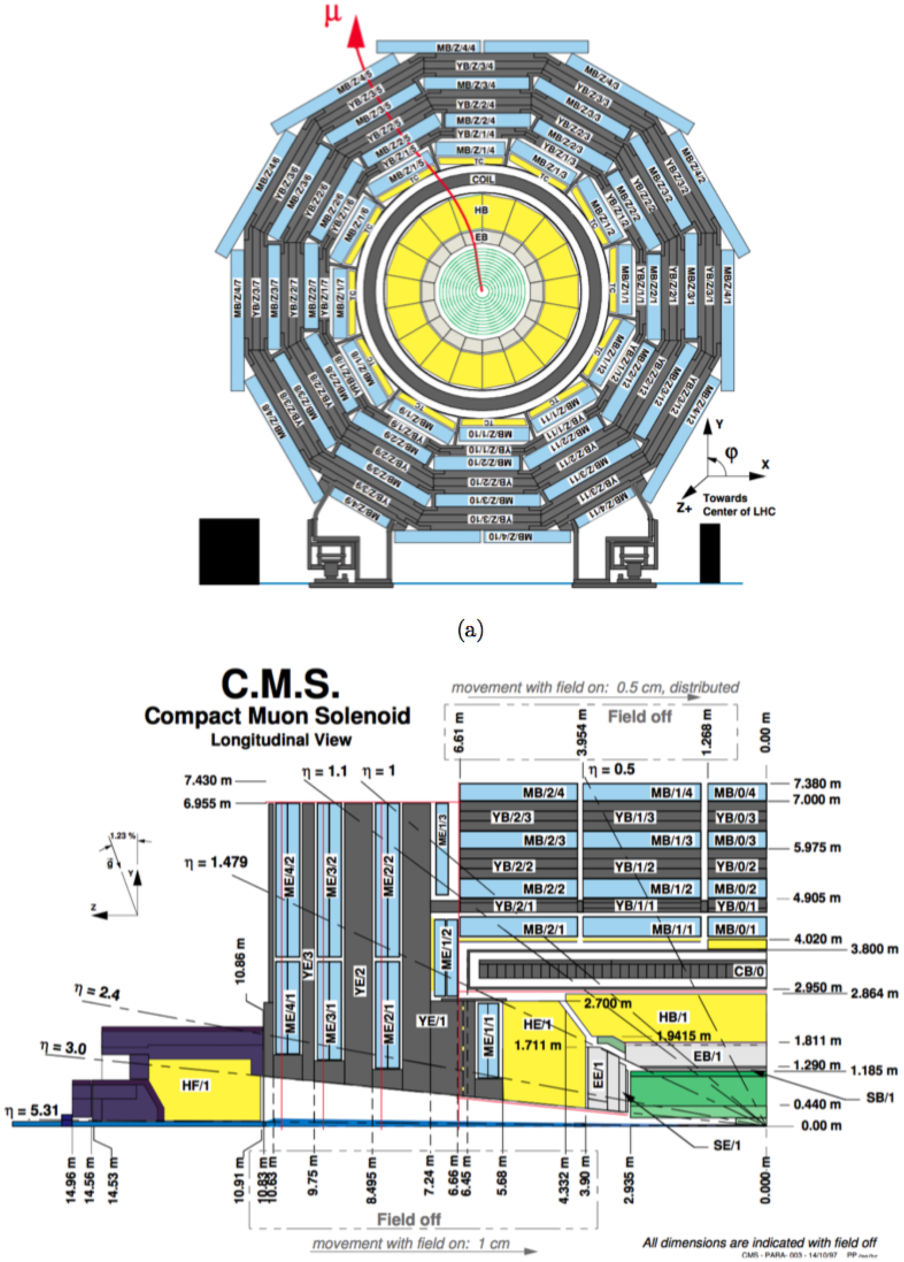

(a)

(b)

Figure 11: On (a) a transverse view of CMS in the barrel region. On (b) a longitudinal view of one quarter of the detector.

Referring to the Cartesian system, the momentum of a particle can be divided in two components: the longitudinal momentum p_z and the transverse momentum p_T , defined as:

$$\vec{p}_T = \sqrt{\vec{p}_x^2 + \vec{p}_y^2} \tag{58}$$

The magnet bends charged tracks on the ϕ plane, so what is effectively measured is the p_T of the particles. For a particle of energy E, the variable *rapidity* (y) is also introduced, defined as:

$$y = \frac{1}{2} \ln \left(\frac{E + p_z c}{E - p_z c} \right) \tag{59}$$

For high energy particles rapidity can be approximated by pseudorapidity. Both rapidity and p_T are used because parton collision can have the centre-of-mass of the interaction boosted along the z direction; both these quantities have invariance properties under this kind of boost.

2.7 INNER TRACKING SYSTEM

Outside the beam pipe, the first sub-detector found by particles coming from the interaction point is the inner tracking system ("Tracker"), a system of silicon sensors designed to provide a precise and efficient measurement of the trajectories of charged particles. The Tracker consists of two major parts, an internal silicon pixel detector and an outer silicon strip detector. The overall length of the Tracker is 5.4 m with an outer diameter of 2.4 m.

2.7.1 The Pixel Detector

The pixel detector [54] consists of three cylindrical layers of hybrid pixel modules surrounding the interaction point at radii of 4.4, 7.3 and 10.2 cm. Two disks of pixel modules on each side complement the pixel detector, as shown in Figure 12(a). It is built to ensure precise 3D vertex reconstruction to allow efficient τ and b jets identification and covers a pseudorapidity range up to $|\eta| < 2.5$ (see Figures 12(b), 12(c)).

The 66 million active silicon sensors are realized on high resistance n-substrate, with an implanted pn-junction and a pixel cell size of 100x150 μm^2. The minimal pixel cell area is dictated by the readout circuit surface required for each pixel and the small pixel size allows to keep single channel occupancy per bunch crossing around 10^{-4} even in the future high flux scenario (10^7 particles/s at 10 cm).

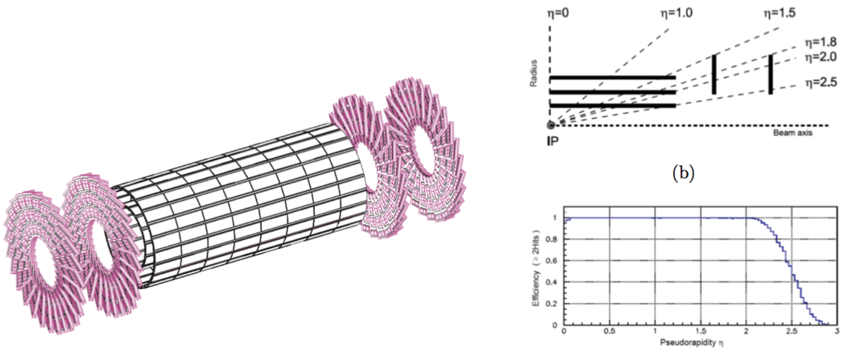

(a)

(b)

(c)

Figure 12: Overview of the pixel detector layout (a); longitudinal view of one quarter of the pixel detector (b) and its hit coverage as a function of (c).

In localizing secondary decay vertices, both transverse and longitudinal coordinates are important and a nearly square pixel shape is adopted. Indium bumps are deposited onto the sensors for subsequent connection to the readout electronics. Movable electrons and holes are created in silicon by ionisation, if a charged particle traverses it. Applying high voltage, these movable charge carriers can be separated and measured as a current, as illustrated in Figure 13(a).

Since the deposited charge is often shared among several pixels, an analog charge readout is implemented. Charge sharing enables interpolation between pixels, which improves the spatial resolution. In the barrel section the charge sharing in the $r\phi$-direction is largely due to the Lorentz effect: the charges drift at an angle (Lorentz angle) relative to the direction of the electric field. The pixel hit reconstruction exploits this effect to improve the spatial resolution by interpolating the charge collected in a cluster. Once the interpolation is done the resulting position is adjusted to account for the Lorentz drift. Because the pixel barrel sensor planes are parallel to the magnetic field, the Lorentz drift is both maximal and in the azimuthal direction. In the endcap pixels the sharing is enhanced by arranging the blades in the turbine-like layout. The spread of the charge over neighboring pixels depends on the particles incidence angle and has a minimum for tracks parallel to the drift direction of the charge carriers. The Lorentz angle is extracted by finding the minimum of the mean cluster size along the local x coordinate measured as a function of the cotangent of the incidence angle α, as shown in Figure 13(b).

The resulting hit resolution depends on the cluster size and position, and is in general between 10 and 25 μm.

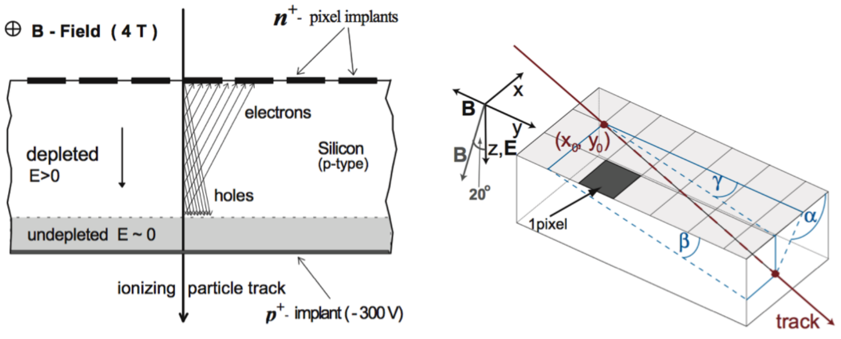

(a) (b)

Figure 13: Functionality of silicon based particle detection (a). On (b) sketch of the track impact angles with respect to a pixel sensor. The magnetic field vector is anti-parallel to the y axis for the barrel sensors and at 20 degrees with respect to the z axis for the endcap sensors.

2.7.2 The strip detector

The pixel system is surrounded by the Silicon Strip Tracker (SST). With its more than 9.3 million detector channels, 15000 silicon modules and a total active detector area of about 200 m^2, it is the largest silicon tracker ever built. The SST was completed at CERN using the tracker integration facility, a clean room with facilities to assemble, connect and operate parts of the tracker in turn. The sealed SST was finally transported to the experimental area and lifted down into the cavern.
The SST consists of four main subsystems, shown in Figure 14: the four-layer Tracker Inner Barrel (TIB), the six-layer Tracker Outer Barrel (TOB) and, on each side of the barrel region, the three-disk Tracker Inner Disks (TID), and the nine-disk Tracker End Caps (TEC). Each TID disk is made of three rings of modules, while TEC disks have seven rings. The entire system is operated at a temperature below 10°C. The active detector elements, the silicon modules, consist of a carbon or graphite fibre frame, which supports the silicon sensor and the associated front-end readout electronics. The silicon sensors are made up of single-sided p^+ strips on n-bulk sensors with two different thicknesses: 320 and 500 μm in the inner four and outer six layers of the barrel, respectively; 320 μm in the inner disks, and 320 and 500 μm in the inner four and outer three rings of the end cap disks, respectively. More than 20 different module geometries exist, with differences in terms of strip length, pitch and material resistivities, to ensure that the single strip occupancy is low even at full LHC luminosity. Both single-sided and double-sided modules (two single-sided modules mounted back to back with a stereo angle of 100 mrad) are used. The final single hits resolution depends on the type of sensors and their

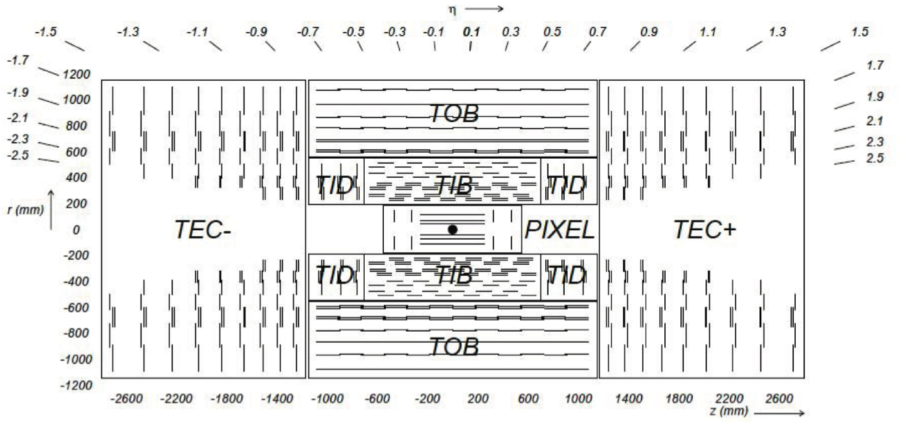

Figure 14: The tracker schematic structure.

position, and has been measured to be between 15 and 45 μm, in accordance to the design expectation.

2.8 THE ELECTROMAGNETIC CALORIMETER

The CMS Electromagnetic Calorimeter is is composed of 75848 lead tungstate ($PbWO_4$) crystals, chosen because of their excellent energy resolution. The detector consists of a barrel region, extending to a pseudorapidity $|\eta|$ of 1.48, and two endcaps, which extend coverage to $|\eta| = 3.0$. The Barrel section (EB) has an inner radius of 129 cm, and is structured as 36 identical supermodules, each covering half the barrel length. Each supermodule is composed by 1700 crystals with a front face cross-section of about 22×22 mm^2 and a length of 230 mm, corresponding to 25.8 radiation lengths (X_0). The crystal axes are inclined at an angle of 3° relative to the direction of the nominal interaction point, in both the azimuthal (ϕ) and η projections.

The two ECAL endcaps (EE) are located at a distance of 314 cm from the vertex and are constructed from four half-disk, each consisting of 3662 tapered crystals, with a frontal area of 2.68×2.68 cm^2 and a length of 22 cm (corresponding to 24.7 X_0), arranged in a quasi-projective geometry. The crystals are focussed at a point 1.3 m farther than the nominal interaction point along the beam line, with off-pointing angles between 2° and 8°.

The crystals in each dee are organised into 138 standard 5×5 supercrystal units, and 18 special shaped supercrystals that are located at the inner and outer radii.

The Endcaps (EE) are located at a distance of 314 cm from the vertex.

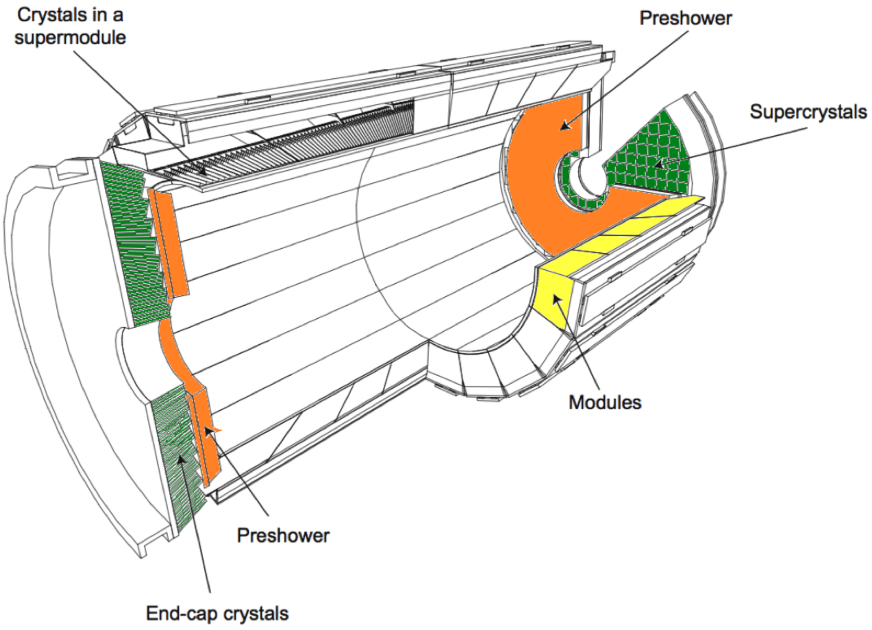

Figure 15: View of the CMS ECAL structure: Barrel (one supermodules in yellow), Endcap (in green), Preshower (in orange).

The endcap crystals have a front face cross section of 28.6×28.6 mm^2 and a length of 220 mm, corresponding to 24.7 X_0. A Preshower detector (ES) is placed in front of the crystal calorimeter over the endcap pseudorapidity range $1.6 < |\eta| < 2.6$. Its active elements are two planes of silicon strip detectors, with a pitch of 1.9 mm, which lie behind disks of lead absorber at depths of 2 X_0 and 3 X_0. A schematic layout of ECAL is reported in Figure 15.

The scintillation light produced in the crystals is read-out by a pair of avalanche photodiodes (APD) for each EB crystal, and a vacuum phototriode for each EE crystal. The small Moliere radius (RM = 2.2 cm) in combination with the large number of crystals results in a fine granularity for the lateral shower shape. In the forward region the granularity is further improved by the Preshower detector.

In order to achieve the desired energy resolution of the ECAL it is necessary to maintain the stability of the per-channel energy calibration over time. This places stringent requirements on the stability of the temperature of the ECAL and of the high voltage applied to the APDs. This is due to the temperature dependence of the crystal light yield, as well as the sensitivity of the APD gains to variations in both temperature and high voltage (the VPT response is much less sensitive to temperature and high voltage variations). The ECAL energy resolution measured in electron test beams is parametrized as

$$\left(\frac{\sigma}{E}\right)^2 = \left(\frac{\alpha}{\sqrt{E}}\right)^2 + \left(\frac{\sigma_n}{E}\right)^2 + c^2 \tag{60}$$

for electrons incident on the center of crystals [55]. The three contributions correspond to the stochastic term, the noise term and the constant term. The stochastic term depends on the event-by-event fluctuations in the electromagnetic shower development, on the photo-statistics and on the photodetector excess noise factor. The noise term depends on the level of the electronic noise and event pile-up. The constant term depends on the non-uniformity of the longitudinal light collection, on the leakage of energy from the rear face of the crystals and on the accuracy of the detector inter-calibration constants. For electromagnetic showers of energies above 100 GeV the energy resolution is dominated by the constant term. As a consequence, in the CMS environment the detector's performance will depend mainly on the quality of its inter-calibration and monitoring.

2.9 THE HADRONIC CALORIMETER

The Hadron Calorimeter (HCAL) is used, together with the ECAL, to perform measurements on direction and energy of hadronic jets and to estimate the amount of missing transverse energy (MET) of each event. The request to perform precise missing ET measurement implies the development of a very hermetic system, whose design is constrained by compactness requests and by the high magnetic field. In order to fulfill these requirements a sampling calorimeter system based on brass absorber layers alternated to active plastic scintillators has been built. The signal coming from active scintillators is read out with embedded wavelength shifting fibers (WLS) and conveyed via clear fiber waveguides to hybrid photodiodes. The choice of brass as absorber material has been driven from its short interaction length λ_I and its non-magnetic nature. The HCAL consists of the following parts:

- HCAL Barrel region (HB). It is located between the EB and the solenoid and covers a range of $|\eta| < 1.3$. The HB contains brass absorber plates alternating with layers of plastic scintillator tiles, which have wavelength shifting fibres embedded for the signal readout. As this setup results in a material thickness of $10.6 \cdot \lambda_I$ at $|\eta| = 1.3$ and only $5.82 \cdot \lambda_I$ at $|\eta| = 0$, the additional HCAL outer region is necessary. The segments of the HB have a tower-like readout, i.e. all the light collected by the scintillator tiles of

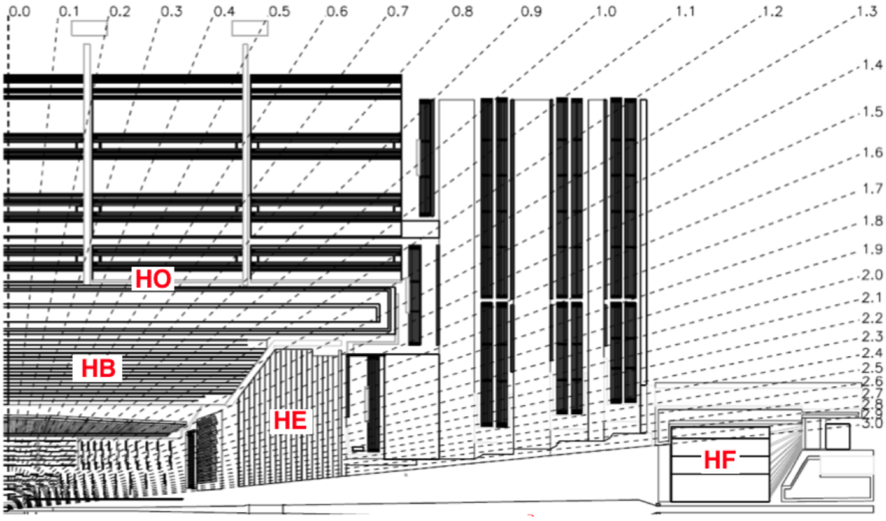

Figure 16: View of the CMS ECAL structure: Barrel (one supermodules in yellow), Endcap (in green), Preshower (in orange).

one segment is directed to one Hybrid Photo Diode via fibres. Thus a two-dimensional resolution of $\Delta\phi = 5^\circ$ and $\Delta\eta = 0.087$ in obtained.

- HCAL Outer region (HO). In order to guarantee the containment of lately developing and high energetic hadronic showers within the calorimeter of the CMS barrel, an additional layer, the HO, is needed. It is also located in the barrel region, but outside the solenoid, and covers $|\eta| < 1.3$ as well. It consists of five wheels, placed in front of the iron return yoke. As the central region of the HB has the lowest material thickness with regard to the trajectory of the hadrons, for the central HO wheel two layers of scintillator tiles surround an absorber (iron). The other four wheels are made of scintillator only, using the solenoid coil as absorber. The segmentation and readout of the HO reflects the HBs tower structure, in order to form combined HCAL towers. Considering all contributions from ECAL, HCAL, the solenoid, support structure and the first layer of the iron return yoke, a minimum material thickness of $11.8 \cdot \lambda_I$ is achieved.

- HCAL Endcaps (HE). They cover a range of $1.3 < |\eta| < 3.0$ and basically work the same way as the HB. As in the HB, scintillator tiles are being read out collectively as HCAL towers. Their granularity decreases from $\Delta\phi = 5^\circ$ and $\Delta\eta = 0.087$ for $|\eta| < 1.6$ to $\Delta\phi = 10^\circ$ and $\Delta\eta = 0.17$ for $|\eta| > 1.6$. Together with the ECAL, the total material thickness is about $10 \cdot \lambda_I$.

- HCAL Forward region (HF). It covers a range of $2.9 < |\eta| < 5.2$, which is not covered by any other detector part. To handle the very high particle fluxes in the forward region of the detector, the design of the HF has to be quite different from the rest of the HCAL. Radiation tolerant quartz fibres are embedded in a $10 \cdot \lambda_I$ long steel absorber. The charged shower particles generate Cherenkov light within the fibres, which are bundled into towers of about $\Delta\phi = 10^\circ$ and $\Delta\eta = 0.17$.

Together, the components of the HCAL cover a range of $|\eta| < 5.2$, which is illustrated in Figure 16 , and only a small range of $< 0.7^\circ$ around the beam direction remains uncovered.

2.10 THE MUON SYSTEM

As implied by the experiments middle name, the detection of muons is of central importance to CMS. Muons provide a clean experimental signature in the detectors that allows to identify signatures of interesting processes, like the predicted "golden-plate" Higgs decays into ZZ or ZZ* then decaying into four muons, over the very high QCD background rate expected at LHC with full luminosity or like many interesting SUSY processes involve muons in the final state. Therefore a precise and robust muon measurement was a central theme from its earliest design stages. The muon system, [59, 60], has 3 functions: muon identification, momentum measurement, and triggering. The high magnetic field enables good muon momentum resolution ($\Delta p_T/pt \sim 10\%$ at $p_T = 1$TeV) while the big amount of material in the flux-return yoke serves as hadron absorber for the identification of muons.

The muon system of CMS is composed by 3 different types of gaseous particle detectors DT, CSC and RPC, as shown in Figure 17. Due to the shape of the solenoid magnet the muon system was naturally driven to have a cylindrical barrel section and two planar endcaps regions. The barrel is composed of five mechanically independent wheels (Wheel ±1, Wheel ±2, Wheel 0). Each wheel is divided in twelve sectors (see Figure 11(a)) and every sector consists of four detector stations integrated in the magnet return yoke. Each of the endcap (see Figure 11(b)) is composed of four disks, called stations (ME1, ME2, ME3, ME4), that close the magnet circuit of CMS. The station ME1 is divided in three concentric rings, while the other three are composed of two rings. With this geometrical layout the muon detector elements cover the full pseudorapidity interval $|\eta| < 2.4$ with no acceptance gaps.

In the barrel region, where the neutron-induced background is small, the muon rate is low and the magnetic field is uniform and mostly

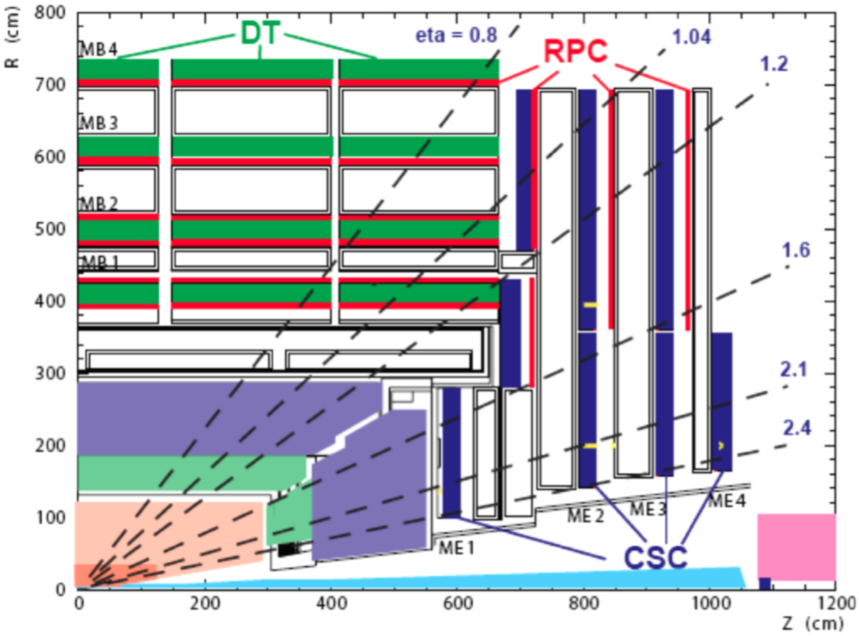

Figure 17: Longitudinal view of on quarter of the CMS detector: he various system composing the CMS muons spectrometer are shown.

contained in the steel yoke, Drift Tube chambers with standard rectangular drift cells are used. The DT chambers [59, 61] cover the pseudorapidity region $|\eta| < 1.2$. and are organized into 4 stations interspersed among the layers of the flux return plates.

The muon system uses Cathode Strip chambers [62] (CSC), in the endcap regions of CMS, where the muon rates and background levels are high and the magnetic field is large and non-uniform. They are characterised by a fast response time, fine segmentation, and radiation resistance. CSCs cover an angular range between $|\eta|$ values of 0.9 and 2.4. They are organized in 4 stations in each endcap, with chambers positioned perpendicular to the beam line and interspersed between the flux return plates. The cathode strips of each chamber run radially outwards and provide a precision measurement in the $r - \phi$ bending plane. The anode wires run approximately perpendicular to the strips and are also read out in order to provide measurements of $|\eta|$ and the beam-crossing time of a muon.

To ensure redundancy and the highest efficiency in the possible high background rates, a complementary dedicated trigger system of resistive plate chambers was added in both the barrel and endcap regions. The RPCs [63, 64] provide a fast, independent, and highly-segmented trigger in the rapidity range $|\eta| < 1.6$. The RPCs are double-gap chambers, operated in avalanche mode to ensure good operation at high rates. They produce a fast response of the order of few ns but a coarser position resolution than the DTs or CSCs. They also help resolve ambiguities in attempting to make tracks from multiple hits in a chamber. A total of 6 layers of RPCs are embedded in the barrel muon system, 2 chambers in each of the first two stations, and 1 in each of the last 2 stations. The redundancy in the first 2 stations allows the trigger algorithm to work even for low-p_T tracks that may not reach the outer 2 stations. In the endcap region, the RPC system composes of one plane in each of the 3 stations.

2.10.1 DT chamber

A schematic layout of a DT chamber and of a DT cell are shown in Figure 18(a) and Figure18(b) respectively. In each chamber there are 12 layers of contiguous drift tube cells grouped in three SuperLayers (SL) with 4 staggered layers each. The innermost and outermost SLs are dedicated to hits measurement in the CMS bending plane ($r - \phi$ plane), while in the central SL the hits are measured along the beam axis ($r - z$ plane). The outermost stations (MB4) located outside the iron return yokes of the CMS magnet have only the two SLs measuring the hit position in the $r - \phi$ plane. Each cell has an area of 13×4.2 cm^2 where 4.2 cm is the distance beetwen two consecutive anode wire. The cells are separated by 1 mm thick aluminium and have a offset of half cell with respect to the upper and lower neighbor cell. With this design, the efficiency to reconstruct a high pT muon track with a momentum measurement delivered by the barrel muon system alone is better than 95% in the pseudorapidity range covered by four stations, $|\eta| < 0.8$.

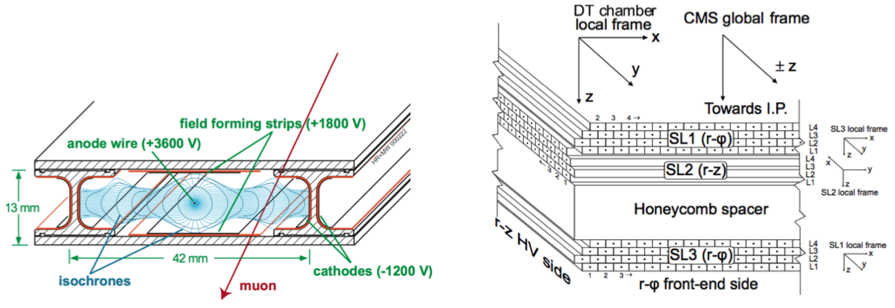

(a) (b)

Figure 18: n (a) transverse view of a drift tube cell, with drift lines and isochrones for a typical voltage configuration of the electrodes. In (b) Cross-section of a barrel muon chamber with the local and global reference frames.

The 100 μm target chamber resolution in $r - \phi$ plane is achieved by the 8 track points measured in the two $r - \phi$ SLs, the single wire resolution being better than 250 μm. To perform a precise BX assignment the deviation from linearity of the space-time relation in each drift cell must be less than 100-150 μm. A multi-electrode design (1 anode wire, 2 field shaping strips, and 2 cathode strips) ensures this performance also in the regions with stray magnetic field.
The DT system consists of 130 chambers, 60 chambers located in the inner three wheel(0, ±1) and 70 chambers in the outer ones(W±2), with about 172000 sensitive wires.

2.10.2 CSC chamber

The CMS Endcap Muon system will consist of 468 cathode strip chambers (CSC) arranged in groups as follows: 72 ME1/1, 72 ME1/2, 72 ME1/3, 36 ME2/1, 72 ME2/2, 36 ME3/1, 72 ME3/2, and 36 ME4/1 (see Figure **??**). The chambers are trapezoidal and cover either 10° or 20° in ϕ; all chambers, except for the ME1/3, overlap and provide continuous ϕ-coverage. A muon in the pseudorapidity range $1.2 < |\eta| < 2.4$ crosses 3 or 4 CSCs. The CSCs are multiwire proportional chambers comprised of 6 anode wire planes interleaved among 7 cathode panels. Figure 20 shows a schematic view of a CSC chamber. Wires run azimuthally and define a tracks radial coordinate. Strips are on cathode panels and run lengthwise at constant $\Delta\phi$ width.

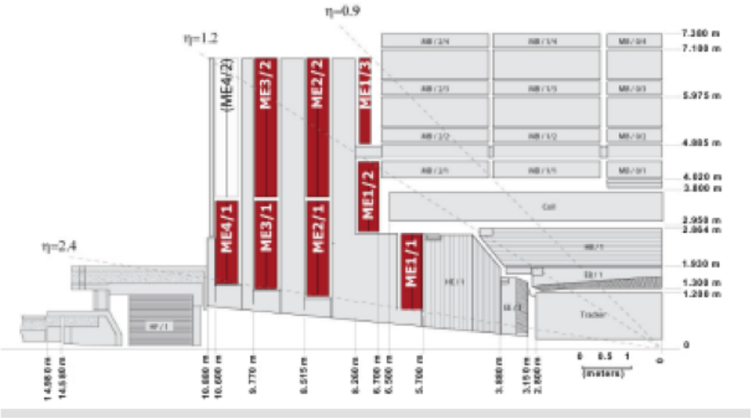

Figure 19: XXX

The largest chambers, ME2/2 and ME3/2, are about 3.4×1.5 m^2 in size. The overall area covered by the sensitive planes of all chambers is about 5000 m^2, for a gas volume more than 50 m^3 , and a number of wires of about 2 million. There are about 9000 high-voltage channels in the

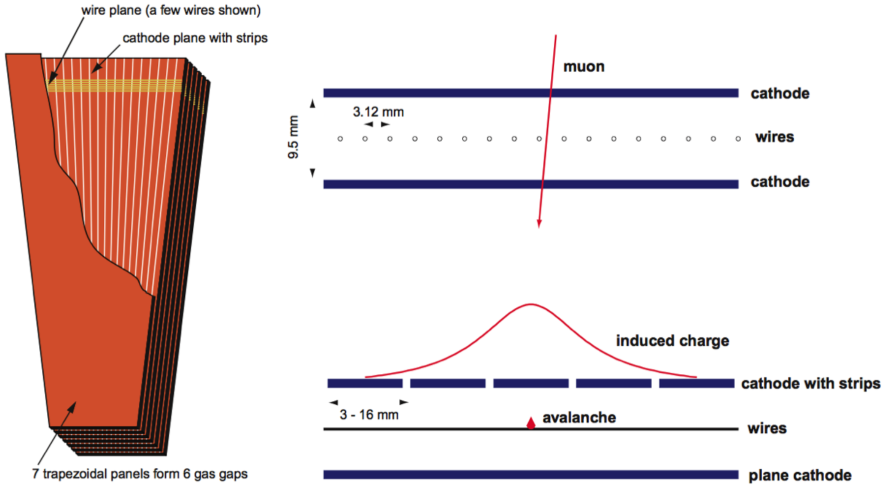

Figure 20: Schematic representation of a CSC chamber (left), and of the effect of a traversing muon in one gap (right).

system, about 220000 cathode strip read-out channels with 12-bit signal digitization, and about 180000 anode wire read-out channels. This system ensures at least 99% efficiency per chamber for finding track stubs by the Level-1 trigger and at least 92% probability per chamber of identifying correct bunch crossings by the Level-1 trigger. This efficiency per chamber and 3-4 CSCs on a muon track path, ensure that the reconstructed muons will be assigned the correct bunch crossing number in more than 99% of cases. The CSC system guarantees a $r - \phi$ resolution at the Level-1 trigger of about 2 mm, that improves up to 75 μm in off-line reconstruction for ME1/1 and ME1/2 chambers and about 150 μm for all others.

2.10.3 RPC chambers

The Resistive Plate Chambers are gaseous parallel-plate detectors that combine adequate spatial resolution with a time resolution comparable to that of scintillators (order of ns). These performances make, the RPCs capable of tagging the time of an ionising event in a much shorter time than the 25 ns between two consecutive LHC bunch crossings (BX). Therefore, a fast dedicated muon trigger device based on RPCs can identify unambiguously the relevant BX to which a muon track is associated even in the presence of the high rate and background expected at the LHC. Signals from such devices directly provide the time and position of a muon hit with the required accuracy. A trigger based on RPCs has to provide the BX assignment to candidate tracks and estimate the transverse momenta with high accuracy in an environment where rates may reach 10^3 Hz/cm^2. The CMS RPC chambers consist of 2 or 3 double-gap modules made by two superimposed single gaps (up and down). Every single gap is formed by two bakelite electrode plates (see Figure 21) characterised by a bulk resistivity of $1 \div 2 \times 1010$ Ω·cm mantained at a distance of 2 mm by polycharbonate bottons. This double-gap configuration with common read-out strips in between (see Figure 22), allows to operate the single-gaps at lower gas gain (lower high voltage) with an effective detector efficiency higher than for a single-gap, because the induced signal is the sum of the 2 single-gap signals. The system works in avalanche mode or low gain mode, that ensures few deposit charge on the electrodes with small dead zone on the plate.

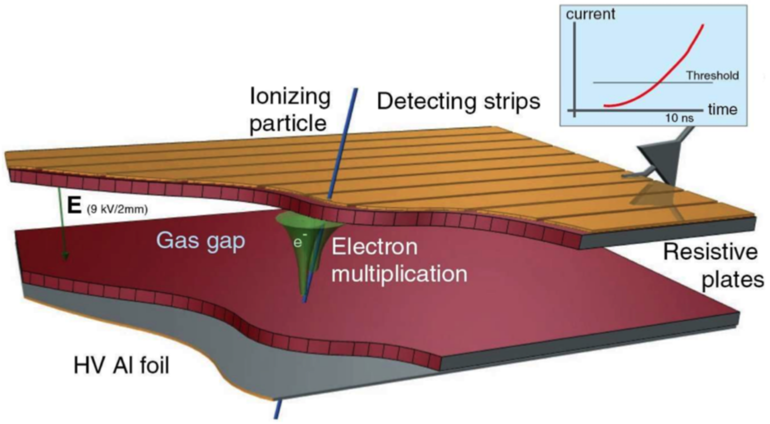

Figure 21: Graphical representation of an RPC gap.

This choice, imposed by high particle flux of LHC, requires a very good front-end electronics enables to work with signal of a amplitude of few pC.

Six layers of RPC chambers are embedded in the barrel iron yoke, two located in each of the first and second muon stations (RB1, RB2) and one in each of the two last stations (RB3, RB4), as shown in Figure 23. The redundancy in the first two stations allows the trigger algorithm to perform the reconstruction always on the basis of 4 layers, even for low pT particles, which may stop inside the iron yoke. In total there are 480 rectangular chambers, each one 2455 mm long in the beam direction. Exceptions are the chambers in sector 3 of wheel-1 and sector 4 of wheel+1, which are 2055 mm long to allow passage of the magnet cooling chimney. Chambers RB1, RB2, and RB3 have widths 2080, 2500, and 1500 mm, respectively. The widths of the RB4 chambers which depend on the location. The strips run along the beam direction providing position measurements in the $r - \phi$ plane .

In the endcap region, the baseline design foresees the instrumentation of the iron disks with 4 layers of RPCs to cover the region up to $|\eta| = 2.1$. They are mounted on both faces of the disks. The double-gaps in every station have a trapezoidal shape and are arranged in 3 concentric rings in the $r - \phi$ view. They overlap in ϕ to avoid dead space at chamber edges. Except for station 1, the chambers of the innermost ring span 20 in ϕ , all others span 10. However, in the first phase, due to budget limitations, only 3 layers up to $|\eta| = 1.6$ are built. A schematic view of endcap RPC system is given in Figure 24.

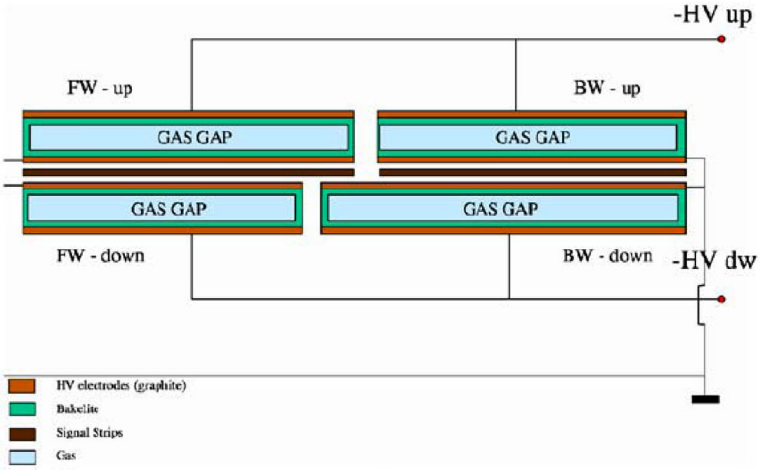

Figure 22: Schematic view of a RPC chamber of CMS

2.11 CMS TRIGGER SYSTEM

When running at its design luminosity, the LHC will deliver bunch crossings every 25 ns, each causing about 20 particle interactions. Most of these events are soft, i.e. no new particles are produced during the collision. Storing the data of all of these events is neither practicable with todays technology nor necessary. In order to select only interesting events and thus to reduce the event rate which has to be processed, a trigger system has been developed for CMS. The Data flow in the CMS Trigger system is shown in Figure 25, it consists of two logic stages:

- The Level 1 triggers (L1 [56]) are hardware based online triggers, meaning that they decide whether to save the events or not, directly after they have been recorded by the detector. In fact, the decision has to be made within 3 μs after each collision, because the data saved in the buffer are overwritten after this period. The L1 triggers lead to a reduction of the event rate from 40 MHz to 100 kHz,

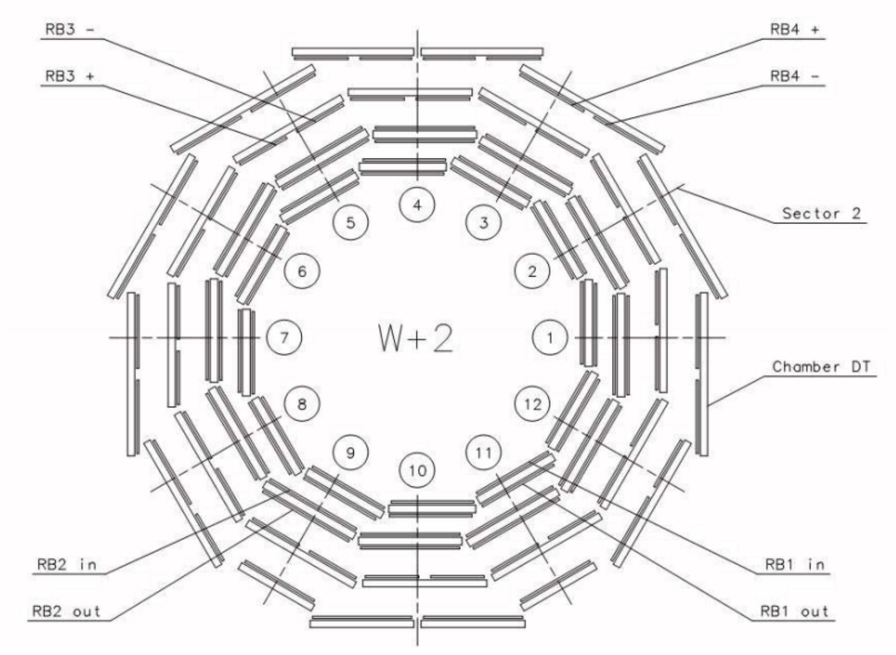

Figure 23: Schematic layout of one of the 5 barrel wheels. Each wheel is divided into 12 numbered sectors.

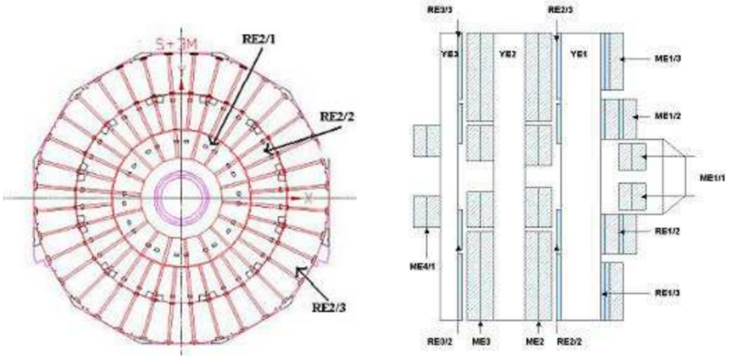

Figure 24: Layout of the $r - \phi$ plane of RE2 RPC (left), and layout of the *initial* CMS Endcap Muon System (right).

which is low enough to be saved and transferred to a computer farm.

- Events passing the L1 trigger are transferred to a computer farm, where they are processed by the second stage of the trigger system, the High Level Trigger (HLT [57]). It is a software based offline trigger, that has more time for making decisions. Thus, it can use reconstruction algorithms to further reduce the event rates. Only permanently storing events that at least passed one HLT criteria, leads to a reduction of the event rate from 100 kHz to 100 Hz, which corresponds to the manageable rate 100 MB/s to be stored on tape.

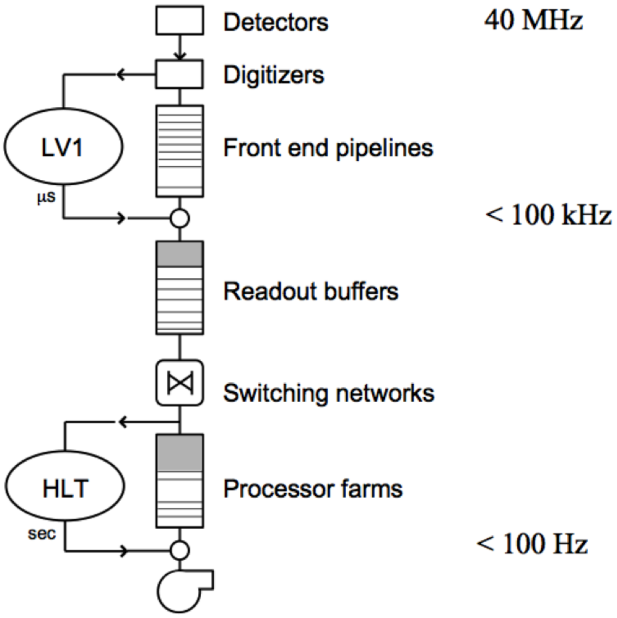

Figure 25: Data flow in the CMS Trigger system. Two consecutive processing stages are implemented: level-1 and High Level Triggers.

Different triggers exist for each of the trigger stages, which are specialised for finding special event types. L1 trigger is organized into three major parts: the L1 calorimeter trigger, the L1 muon trigger, and the L1 global trigger. For sub-L1-systems, the calorimeter trigger preserves the tower energy sums from the ECAL, HCAL and HF individual cells (or towers) and reconstructed candidates of electrons, photons, taus and jets. Thresholds are added on these particle candidates.

In design, for instance, the transverse missing energy trigger requires the events with MET (Transverse Missing Energy) greater than 100 GeV, but at the very first low luminosity this trigger was not enabled. The muon subtrigger focuses on μ preselecting. Information from DT, CSC and RPC is used to drop events with low quality muons. The global muon trigger converts muon tracks from different chambers into the same η, ϕ and p_T scale, then to correlate the tracks.

Another important task for global muon trigger is to identify whether the muon is isolated or not via vetoing the event with an $\eta\phi$ grid of unquiet calorimeter towers. The global L1-subtrigger holds a time match on these information from both calorimeter and muon chambers, and decides to accept or reject each bunch crossing based on the programmed logical combination. The CMS data acquisition system processes events accepted by the first-level trigger at a maximum input rate of a few 100 kHz. Event data are read out from the detector and stored in readout buffers at a total rate of 1 Terabit/s. The event-builder then assembles event fragments into full events employing a large switching network.

The high-level trigger algorithms run on a farm of commercial processors. Each event is processed by a single processor, which has access to the full raw event data. High level-trigger reconstruction code will be as close as possible to the full offline analysis code, the main differences resulting from limited processing time and the possible lack of precise calibration constants. The following three key features of HLT software guarantee minimal processing time:

- Reconstruction on demand. Trigger objects are only reconstructed if needed in the trigger decision. Unnecessary calculations are avoided by rejecting events as early as possible using fast algorithms. The reconstruction and selection therefore take place in several stages (virtual trigger levels), which roughly correspond to the functions of traditional second and third trigger levels. There is no limitation to the number of virtual trigger levels or to the algorithms employed except for CPU time. For historic reasons the terminology Level-2 is used for a first high-level trigger stage based on data from the muon systems and calorimeters while Level-3 refers to algorithms including tracker data.

- Partial/Region reconstruction: only parts of detector information are analysed guided by the trigger objects found in the preceding trigger levels.

- Conditional reconstruction. Reconstruction is aborted if further calculations would not alter the result (for example when reconstructing additional tracks in an isolation algorithm) or if the condition arises that resulting trigger object would not be relevant to the trigger decision.

HLT available algorithm changed a lot since the startup, in order to follow the luminosity delivered by LHC. Events that have passed the HLT reach the CERN Tier0 for the recostruction and are then distributed on the GRID for an easy access for all the CMS collaboration.

3 THE TOP QUARK

3.1 INTRODUCTION

Since its discovery by the CDF and D0 experiments at the $p\overline{p}$ collider Tevatron in 1995 [65, 66] the top quark has been a pivotal topic of particle physics research, for many good reasons. With a mass $m_t = 173.2 \pm 0.9$ GeV [67], it is by far the heaviest of all known quarks. The top quark is around 40 times heaver than the b-quark and has a mass which is comparable to the one of a Rhenium atom (atomic number $Z = 75$). As it is also much heavier than the W boson, it can decay into two-body final states $t \to Wq$, of which the mode $t \to Wb$ has almost 100 percent branching fraction. The latter observation implies that, in the SM with three generations of fermions, the Cabibbo-Kobayashi-Maskawa (CKM) matrix element $|V_{tb}|$ is close to unity. Due to the very short lifetime of the top quark, it decays before it can hadronize. This offers the unique opportunity to study the properties of a bare quark, including effects due to its spin which are transferred into respective angular correlations among its decay products.

The top quark is the charge $Q = +2/3e$, weak isospin $T_3 = +1/2$ partner of the b-quark in the third generation weak isospin quark doublet. Its existence was postulated already many years before its experimental evidence, in particular once the b-quark was discovered in 1977. In the following years, indirect evidence that the top quark must exist was obtained from limits on flavor-changing neutral-current (FCNC) decays of the b-quark as well as from the absence of tree-level mixing in the $B_d^0\overline{B_d^0}$ system, which indicated that the b-quark must be the member of an isospin doublet. In addition, its weak isospin $T_3 = -1/2$ was determined from measurements at LEP and SLC, leading to the conclusion that the postulated partner of the b-quark should have $T_3 = +1/2$.

At hadron colliders, top quarks are produced either in pairs, dominantly through the strong interaction, or singly through the weak interaction. Thus, top quark production and decay allow important tests of the features of two important forces of the SM.

The large value of m_t also implies a large coupling to the Higgs boson. The top quark Yukawa coupling $y_t = m_t/v$, where $v \sim 246$ GeV is the vacuum expectation value, is close to unity. Because of this observation, it has often been speculated that the top quark may play a special role in the electroweak symmetry breaking, either in the context of the Higgs model, or invoking alternative mechanisms through which

elementary particles acquire mass.
The top quark appears in higher order loop diagrams of the electroweak theory, which implies that m_t is a crucial parameter in this theory. Precise measurements of m_t provide, together with other parameters of the electroweak theory, in particular the mass of the W boson m_W , indirect constraints on the mass of the Higgs boson.
Besides its potential role in electroweak symmetry breaking, the top quark plays an important role in many scenarios for new physics beyond the SM. Several models predict the existence of new particles which decay mostly into top quark pairs. In addition, precise measurements of the properties of the top quark and its interactions may reveal effects from new physics. This concerns in particular the study of differential distributions, such as the asymmetry in the rapidity distributions of top quark and anti-quark, but also the search for FCNC in top quark decays and for the production of same-sign top quark pairs.

3.2 TOP QUARK DECAYS

The top quark decays almost exclusively as $t \to Wb$.
Since $|V_{tb}| >> |V_{td}|, |V_{ts}|$, the decays $t \to W(d,s)$ are strongly suppressed; neglecting these decays, the total width of the top quark in the SM at NLO QCD is [68]:

$$\Gamma_t = \frac{G_F m_t^3}{8\pi\sqrt{s}} |V_{tb}|^2 \left(1 - \frac{m_W^2}{m_t^2}\right) \left(1 + 2\frac{m_W^2}{m_t^2}\right) \left[1 - \frac{2\alpha_s}{3\pi}\left(\frac{2\pi^2}{3} - \frac{5}{2}\right)\right], \quad (61)$$

where G_F is the Fermi constant. Using $m_t = 172.5$ GeV yields $\Gamma_t = 1.33$ GeV. The large width of the top quark corresponds to a very short lifetime $\tau_t = 1/\Gamma_t \sim 5 \cdot 10^{-25}$ s.
The lifetime of the top quark is one order of magnitude smaller than the typical formation time of hadrons $\tau \sim 1fm/c \sim 3 \cdot 10^{-24}$ s, which means that top quarks decay before they can hadronize. It also means that no *toponium* $t\bar{t}$ bound state can exist. As a consequence, the spin information of the top quark is transferred to its decay products. The polarization of the W boson from the top quark decay can be either longitudinal or transverse according to the V-A structure of the Wtb vertex. Moreover the decay $t \to Wb$ allows us to measure $|V_{tb}|$ evaluating the ratio:

$$R = \frac{BR(t \to Wb)}{t \to Wq} = \frac{|V_{tb}|^2}{|V_{td}|^2 + |V_{ts}|^2 + |V_{tb}|^2} \quad (62)$$

while $|V_{td}|$ and $|V_{ts}|$ may not be practically measured via the top decay processes. This relation allows to measure the absolute magnitude of $|V_{tb}|$ if we assume three generations of quarks, *i.e.*

$|V_{td}|^2 + |V_{ts}|^2 + |V_{tb}|^2 = 1$. $|V_{tb}|$ can be measured directly, with no assumptions about the number of generations, is to measure single top quark production via the weak interaction.

3.3 TOP QUARK PRODUCTION

3.3.1 Top quark pair production

In the SM, the dominant production mechanism of top quark pairs ($t\bar{t}$) is via strong interaction. Thus, since the top quark mass m_t is much larger than Λ_{QCD}, $t\bar{t}$ production at LHC can be successfully described in terms of quantum chromodynamics. In the QCD parton model, the description of the process $pp \to t\bar{t}$ can be separated into a short distance (hard scattering) partonic cross section for the participating partons of type i and j, $\hat{\sigma}_{ij}$, and into long distance terms factorised together in the parton distribution functions (PDFs) $f_i(x_i, \mu_f^2)$, where x_i is the hadron longitudinal momentum fraction carried by the parton i. The separation is called factorization of the interaction and is set by the factorization scale μ_f^2. The hard process involves only high momentum transfer, is calculable with perturbative QCD and is almost insensitive to low momentum scale. The factorization is valid to all orders of the perturbative theory, getting weaker dependence on the arbitrary scale μ_f^2 as more perturbative terms are added in the expansion.
The parton distribution functions (PDFs) $f_i(x_i, \mu_f^2)$ can be interpreted as the probability density to observe the parton i with the longitudinal momentum fraction x_i, when the hadron is probed at a scale of μ_f^2. The PDFs can not be calculated in perturbative QCD, so are extracted by global fits from deep-inelastic scattering and other data. In Figure 26 PDFs calculated at NNLO are shown [69].
The total top quark pair production cross section for hard scattering processes, in pp or $p\bar{p}$ collisions at a centre of mass energy $\sqrt{s}$ can be written as

$$\sigma_{t\bar{t}}(s, m_t) = \sum_{i,j=q,\bar{q},g} \int dx_i dx_j f_i(x_i, \mu_f^2) f_i(x_j, \mu_f^2) \hat{\sigma}_{ij \to t\bar{t}}(\hat{s}, m_t, \mu_t, \mu_r, \alpha_s). \quad (63)$$

The sum runs over all partons (quarks and gluons) contributing, x_i are the parton momentum fractions with respect to the proton momenta, $f_i(x_i, \mu_f^2)$ are the proton PDFs, μ_f and μ_r are the factorization and renormalization scales, α_s is the strong coupling and $\hat{s} \sim x_i x_j s$ is the partonic centre-of-mass energy. The indexes ij runs over all the parton pairs $q\bar{q}$, gg, qg, where only the processes $gg \to t\bar{t}$ and $\bar{q}q \to t\bar{t}$ contribute at the leading order (LO) approximation. The Feyman diagrams at LO are shown in Figure 27.

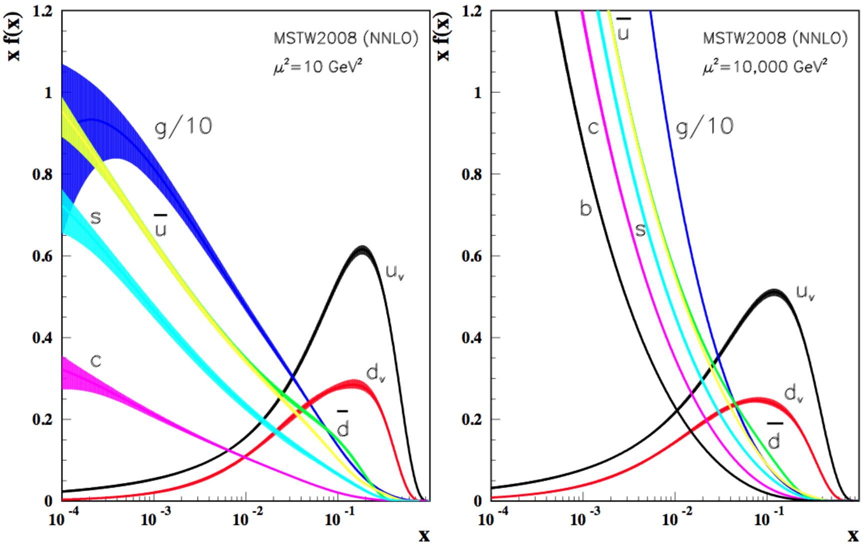

Figure 26: Distributions of x times the unpolarized parton distributions $f(x)$ and their associated uncertainties using the NNLO MSTW2008 parameterization [70] at a scale $\mu^2 = 10GeV^2$ and $\mu^2 = 10000GeV^2$.

The renormalization[1] and factorization scales are typically set to a hard scale of the process, and one often identifies $\mu = \mu_f = \mu_r$. At the LHC with $\sqrt{s} = 7(14)$ TeV, around $80(90)\%$ of the total cross section is due to the gg induced contribution, while the remainder is mostly due to the $q\bar{q}$ initial state. This is due to the large gluon density in the proton at small x (see Figure 26) and the fact that the typical value of $x = 2m_t/s$ (due to the minimal energy needed of $\hat{s} > 4m_t^2$ and setting $x_1 = x_2$) is $0.05(0.025)$ at $s = 7(14)$TeV. At the Tevatron $p\bar{p}$ collider, the situation was reversed with the $q\bar{q}$ contribution dominating and the PDF being probed at much larger x values (around $x = 0.2$). At both colliders, the gq $(g\bar{q})$ contributions contribute only at the percent level, since they are suppressed by an additional factor α_s. The top quark pair production cross section has been recently calculated at the NNLO (next-to-next-to-leading order) in QCD, including threshold resummations, by N. Kidonakis [71].

Table 3 summarizes the $t\bar{t}$ cross section calculations for Tevatron and LHC energies. The LHC is truly a "top factory", producing, at design energy and luminosity more than ≈ 1 top pair per second.

---

[1] The dependence on μ_r of the partonic cross section, computed in truncated perturbation theory, arises in particular from the definition of the renormalized coupling α_s.

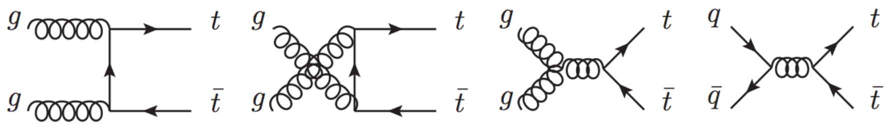

Figure 27: Feynman diagrams for $t\bar{t}$ production at leading order QCD.

	σ_{NNLO} (pb)	$q\bar{q} \to t\bar{t}$	$q\bar{q} \to t\bar{t}$
Tevatron ($\sqrt{s} = 1.96$ TeV, $p\bar{p}$)	7.2	85%	15%
LHC ($\sqrt{s} = 14$ TeV, pp)	894	10%	90%

Table 3: Cross sections, at next-to-next-to-leading order in QCD including gluon resummation corrections, for $t\bar{t}$ production via the strong interaction at the Tevatron and the LHC for $m_t = 173\text{GeV}$.

3.3.2 Production of single top quarks

Top quarks can be singly produced through the electroweak interaction. Three different production modes exist (Figure 28):

- in the t-channel mode, a space-like W boson scatters off a b quark, which is either considered through the b quark PDF in the proton or produced via gluon splitting $g \to b^{-}b$;
- in the s-channel mode, a time-like W boson is produced from two quarks belonging to an isospin doublet, *e.g.* $u\bar{d}$, and subsequently devas into $t\bar{b}$;
- in the tW-channel mode, which is also called associated production, the top quark is produced in association with a close-to real W boson.

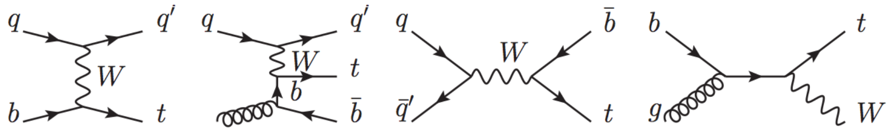

Figure 28: Leading order Feynman diagrams for single top quark production.

So far, the electroweak single top production has been observed at Tevatron in s and t channels [?] and at LHC in tW [?] and t channel [?]. Calculations of fully-differential NNLO or NLO single top quark cross sections have been performed in [72, 73] and the results for Tevatron and LHC energies are shown in Table 4. The production rate changes significantly from the Tevatron to the LHC: a valence-induced process as

s-channel is increased by about an order of magnitude, while the gluon or b-induced processes (t-channel) are enhanced by about a factor of 100. For its small cross section and the presence of large backgrounds the tW-channel has never been observed at Tevatron. On the other hand the s-channel has not yet been observed at the LHC.

Single top quark production is interesting for various reasons. Its proof of existence provides a relevant test of the standard model. It is important to measure all three production modes, since they are sensitive to the Wtb vertex in different ways. Non-standard couplings would indicate the presence of contributions from new physics. Also, single top quark production allows to directly measure the CKM matrix element $|V_{tb}|$ without making an assumption on the number of generations, and to verify the unitarity of the CKM matrix. Deviations from the SM expectation could indicate a possible fourth generation. Another feature of electroweak single top quark production is that the top quark is produced left-handed and in its rest frame, it is 100% polarized along the direction of the light quark. Since top quarks decay before they can hadronize, the polarization information is transferred to their decay products. In particular, the distribution of the polar angle of the lepton from the $t \to Wb \to l\nu lb$ decay and the spin axis, approximated by the direction of the light quark jet in the top quark rest frame, is expected to be proportional to $(1 + \cos\theta^*)$, [74].

The current status of the measurements of single top quark production at LHC will be discussed in next section.

	s-channel	tW-channel	t-channel
Tevatron ($\sqrt{s} = 1.96$ TeV, $p\overline{p}$)	1.04	0.22	2.08
LHC ($\sqrt{s} = 7$ TeV, pp)	4.59	15.6	63.2
LHC ($\sqrt{s} = 14$ TeV, pp)	11.9	83.6	243

Table 4: Cross sections, at the next-to-leading order (for s-channel) or the next- to-next-to-leading order (for tW and t channels), for top quark production via the electroweak interaction, at the Tevatron and LHC, for $m_t = 173$GeV .

4 SINGLE-TOP MEASUREMENTS

4.1 t-CHANNEL TOPOLOGY

Diagrams in Figure 29 show the t-channel so said 2→2, and 2→3 schemes.

The final state of single top events is constituted by one top quark, a light (u,d,s) or c quark and a b quark for the 2→3 scheme. One extra final state b quark is also present in the 2→2 scheme: since there is no valence b quark it can only come from a sea contribution, therefore only $b\bar{b}$ pairs is always present. Such $b\bar{b}$ pairs in the initial state are produced from the splitting of a sea gluon of the proton. This has two consequences: first of all, event samples generated separately for 2→2 and 2→3 processes can have a superposition depending on the hadronization cutoff of the perturbative scale. To evaluate the total cross section of 2→2 and 2→3 the effect of this cutoff has to be taken into account in order to avoid double counting of events. Second, the extra b quark results in an extra b-jet stemming from the quark hadronization, which has to be accounted for in the selection. For this thesis work, we considered events where the top decays through the chain: $t \to Wb \to \mu\nu b$. The branching ratio (BR) of $t \to Wb$ is very close to 1, [? ?] , while the BR of $W \to l\nu$ is ≈ 0.324 and the BR to muons is ≈ 0.11.

The final state event topology therefore consists of one muon, one neutrino, one light quark and one or two b quarks. The muon can be directly reconstructed in the detector, while from b and light quarks hadronization stem jets which can eventually be identified as associated to b quarks throught the b-tagging algorithms. The neutrino cannot be directly detected, yet the components of its momentum in the plane transverse to the beam axis can be inferred from the missing energy in the detector to get kinematic closure of the events. It is notheworthy that we also consider events where W decays to $W \to \tau\nu \to \mu\nu\nu$ as part of our signal. Both our acceptances (rate) and our Monte Carlo simulated distributuons take this fraction of events into account. The effect on the rates is O(10%) and the distortion of the shapes is in most cases negligible. On the other hand, to discriminate $W \to \tau\nu \to \mu\nu\nu$ and $W \to \mu\nu$ events would require much complication, which is not necessary considering them inclusively.

Several physics processes can generate events which reproduce such topology, thus constituting, background sources for our processes. The most important are:

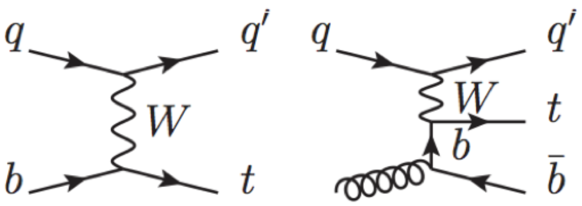

Figure 29: Standard Model single top t-channel production mechanisms: the so said (2)→(2) (left), and (2)→(3) schemes (right).

- W+jets: The processes where a W boson is produced in association to jets are an important source of background. In particular, processes where W decays through $W \rightarrow \mu\nu$ and are associated to a c quark or $b\bar{b}$, $c\bar{c}$ quark pairs could be misidentified as signal events. Also events where W is associated to light partons (u, d, s and gluons), can mimic signal events, in case one of the jets stemming from a light parton mimics the behavior of a b-jet. The low probability for such an event to occur is balanced by the much higher cross section of such processes with respect to t-channel cross section.

- $t\bar{t}$: The processes where a $t\bar{t}$ quark pair is produced are also an important source of background. In particular events where one t quark decays leptonically, namely through the chain $t \rightarrow Wb \rightarrow l\nu b$, and the other top quark decays hadronically, namely through the chain $t \rightarrow Wb \rightarrow q\bar{q}b$, are the most signal like. Such events are also called semi-leptonic $t\bar{t}$events in jargon. The semi-leptonic $t\bar{t}$ jet multiplicity is in general higher than for the t-channel, and this reduces the contamination from this background.

- Multi-jet QCD: Events where a well isolated muon is present and the jet environment reproduces the signal topology in hard QCD scatterings are very rare, nevertheless, due to the much higher cross section of such multi-jet QCD processes its contribution to the background is not negligible.

- s, and tW channels: the other single top processes, in particular the tW-channel, can eventually produce a non-negligible contamination in the signal region. Such backgrounds, like the $t\bar{t}$ background, share with the t-channel the decay chain of the top quark.

- VV ,Z+jets and others: diboson processes like WW, WZ, and ZZ, or Z+jets processes are also minor sources of backgrounds which can reproduce in some cases the t-channel topology. However either the low cross section for VV processes (with $V = W$ or Z), or the extremely narrow phase space for Z+jets processes passing the cuts, consistently limit the contamination from such processes. Other SM possible background processes (multi-boson production, multi-top production, SM higgs) have a much smaller cross section than the t-channel, and in general their countribution is limited to very rare topologies. They are therefore are considered negligible.

4.2 EVENT SELECTION

The events selection is optimized for the final state topology of the t-channel production (see Figure 29), which is characterized by:

- one charged lepton with high transverse momentum and high missing transverse energy coming from escaping neutrino. Both come from the W boson decay stemming in turn from top quark decay;
- one b-flavoured jet with high transverse momentum coming from the hadronization of the b-quark from top decay;
- one low energy b-jet coming from gluon splitting;
- one light jet coming from the hadronization of the light quark recoiling against the top quark. Due to the massiveness of the top quark this jet is produced forward in the collisions, *i.e.* with high pseudorapidity values and thus at low angle with respect to the beam axis.

Therefore, to enrich the data sample in signal events it is required exactly one lepton (muon in this analysis), one b-jet, and one light flavoured jet. The main backgrounds for the signal of interest are W+jets and $t\bar{t}$ events. W+jets, and in particular W+heavy flavours background, where the W decays in leptons is strongly reduced by the 2 jets requirement. W+light partons is further on suppressed requiring that one of the two jets is a b-jet.

The $t\bar{t}$ background can mimic the topology of our signal, especially when one top quark decays leptonically and the other in hadronic modes. Whatever the decay modes are, these events are characterized by the presence of two b-jets stemming from top decay. So, the requirement of only one b-tagged jet helps in reducing this background.

An other dangerous background that has to be taken under control for its very high production cross section is the hadronic multi-jet production in which an muon is present, the so called QCD background. In these processes the lepton could come from the decay of b and c flavored hadrons. The tight lepton selection and the quality criteria on the two jets (as the high transverse momentum requirement) help in reducing this background. An ulterior strong suppression is obtained cutting on the reconstructed W transverse mass which sharply separates the QCD background from the processes where a W boson is produced (as the single top channels, $t\bar{t}$, $W+$ jets). The definition of objects is based on the imposition of general quality criteria and kinematic cuts aiming to minimize the fake rate and to get the best possible measurement of physics objects parameters. In the following we go into details of each selection step.

4.2.1 Physics objects definition and counting

In the following the basic analysis objects are defined on which the event selection and the kinematic reconstruction are based. The reconstruction of all objects is done through the Particle Flow (PF) algorithm [75].

MUONS A reconstructed track in the detector is labelled as a muon by requiring more than 10 valid hits in the silicon tracker, out of which at least one in the pixel detector; at least two segments matched to the global muon object in the muon chambers; a distance of less than 1 cm between the z coordinates of the leading primary vertex and of the muon track at the point of closest approach. Only reconstructed muons with a transverse momentum $p_T > 25$ GeV/c within the trigger acceptance range ($|\eta| < 2.1$) are selected. We add an isolation requirement in order to reject muons coming from QCD events cutting on the "relative isolation" variable $I_{rel} < 0.05$, defined as:

$$I_{rel} = \frac{I^{ch.h} + max((I^{\gamma} + I^{n.h} - I^{PU}), 0)}{p_T} \tag{64}$$

where $I^{ch.h}$, I^{γ}, and $I^{n.h}$ are the sum of the transverse energies deposited by stable charged hadrons, photons, and neutral hadrons in a cone of size $\Delta R < 0.3$ around the muon direction. $I^{PU} = 0.5 \times \sum p_T^{PU}$ is the sum of transverse momenta of tracks associated to non-leading vertices, used to estimate the contribution of neutral particles from pileup events by applying a multiplicative factor 0.5 that takes into account the neutral-to-charged particles ratio expected from isospin invariance. Tight muons are selected by the requirement $I_{rel} < 0.12$.

An additional muon definition is given, with looser identification and kinematic cuts with respect to the tight lepton. We define "loose muon" by requiring a reconstructed muon with $p_T > 10$ GeV/c within the full muon acceptance range ($|\eta| < 2.5$), and $Iso_{rel} < 0.2$.

We require the presence of exactly one tight lepton. In order to reduce the contribution of dilepton events, which can come from $t\bar{t}$ or from Drell-Yan processes, we veto events with additional loose muons or loose electrons. Figure 30 shows the jet multiplicity after the lepton counting in data and simulation. The signal (red) is still overwhelmed by background, in particular W+jets and $t\bar{t}$ events. W+jets events contaminate lower jet multiplicity bins, while $t\bar{t}$ events dominate higher jet multiplicity bins. From Figure 30 it's clear that in most of the signal events two jets are reconstructed, therefore making this bin the most signal efficient.

JETS The jets are reconstructed using the anti-k_T algorithm (described in details in [76]) with a cone size of 0.5, taking as input particles defined in the particle flow algorithm. Briefly it reconstructs and identifies all the physics objects in the event (leptons, photons, hadrons) with a combination of the information from all CMS subdetectors. The redundancy of information allows an optimal determination of the particles direction, energy and type, as well as it reduces the systematic uncertainties and experimental biasses. The jet energy is scaled by a factor that describes the detector response depending on the transverse energy and the pseudo-rapidity of the jet [77].
To reduce contamination from pileup events, charged particle candidates not associated to the main primary vertex are subtracted event by event. The energy of the jet is then corrected by the amount of energy deposited by neutral pile-up hadrons in the jet area.
We perform a cut on the jet calibrated $p_T > 40$ GeV/c, and require $|\eta| < 4.5$. The event is accepted for further analysis only if at least two such jets are reconstructed, and the leading two have transverse energy greater than 60 GeV.

b-JETS Several b-tagging algorithms are available in CMS. Some exploit the long B-hadrons lifetime, others their semi-leptonic decay modes and others use kinematic variables related to the high B-meson mass and hard b-quark fragmentation function. The algorithm used for this study is the so colled "track counting" in the "high purity" version. This algorithm calculates the signed 3D impact parameter significance (IP/σ_{IP}) of all the tracks associated to the jet that pass tight quality criteria, orders them by decreasing values of this observable, and outputs as jet discriminator the value of IP/σ_{IP} for the third track. In simulated signal events with one identified lepton and two jets, we find an average efficiency of

43% for jets matched to b quarks at the generator level within $\Delta R < 0.3$, with $p_T > 40 GeV/c$ and within the tracker acceptance (i.e., $|\eta| < 2.5$). This efficiency however depends on the sample.
The signature of the t-channel single-top production includes 3 partons in the final state, see Figure 29: one light quark recoiling against the virtual W boson, one b quark from the top-quark decay, and a second b quark from the initial gluon splitting. Since the second b quark is most likely produced at very high rapidities, *i.e.*, outside the tracker acceptance of $|\eta| < 2.5$ and thus not allowing b tagging to be performed, we expect most signal events to have only one b-tagged jet. The b-tag multiplicity in 2-jets events is shown in Figure 31 for data and simulation. The contribution of processes without b quarks in the final state is strongly suppressed in the 1-tag sub-sample, showing the largest population of signal events at the same time; the small 2-tags sub-sample is dominated by $t\bar{t}$. Therefore, selected events are required to have exactly one b-tagged jet. This requirement is further tightened by rejecting the event if the jet which fails the tight b-tagging selection passes the loose one.
Notable samples which are studied and used in this analysis are the 2 jets 0 tags sample (W+jets enriched), the 2 jets 1 tag (t-channel enriched) and the 3 jets 1,2 tags, enriched with $t\bar{t}$ events.

MISSING TRANSVERSE ENERGY The missing transverse energy (MET, $\not{E}_{\mathrm{T}}$) is defined as the opposite of the vectorial sum of the transverse momenta of all particles.

TRANSVERSE w BOSON MASS The lepton and neutrino stemming from W boson decay have an invariant mass distribution which is a Breit-Wigner distribution peaked at the W boson mass value. It has to be kept into account that while the transverse momentum components of the neutrino can be reasonably approximated by the components of the missing transverse energy, neutrinos longitudinal momentum is much more difficult to correlate with detector observables, since no reliable estimate of longitudinal energy lost in the beam pipe can be made. A convenient variable to be defined in this situation is the W transverse mass, which is reconstructed out of the transverse components of leptons and neutrino:

$$m_T = \sqrt{(p_{T,l} + p_{T,\nu})^2 + (p_{x,l} + p_{x,\nu})^2 - (p_{y,l} + p_{y,\nu})^2} \qquad (65)$$

This variables is used for QCD rejection since the transverse mass of the alleged W bosons accumulates at low values while all processes with real W bosons tend to cluster around the W mass (this feature is known in the literature as "Jacobian peak").

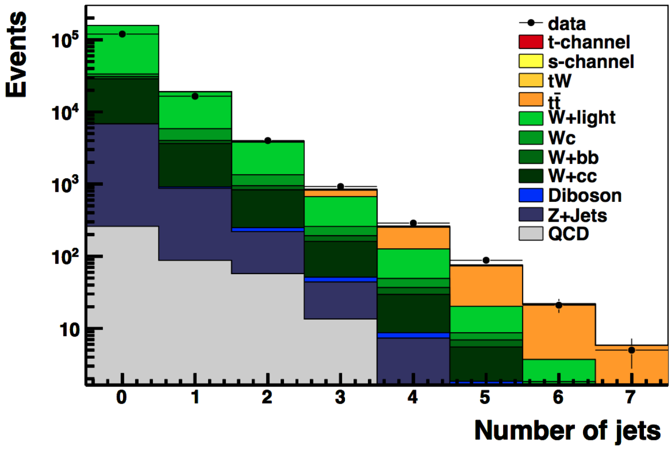

Figure 30: Jet multiplicity after the lepton counting in data and simulation.

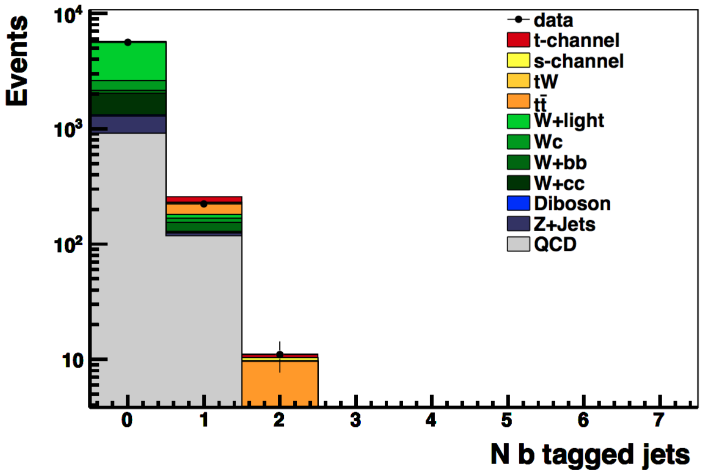

Figure 31: *b*-tag multiplicity in 2-jets event for data and simulation.

4.3 DISCRIMINATING SIGNAL VARIABLES

We identified a set of characteristic single top variables in order to further discriminate signal events from background once the baseline selection has been performed. The Figure shown in this section correspond to 7TeV data and are shown as an example of the variables behavior.

LIGHT JET PSEUDORAPIDITY A first striking feature of single top events is the presence of a jet generated from the fragmentation of the light quark recoiling against the top quark (see Figure 29). Such jet's characteristic η distribution, in Figure 32, stemms from the kinematics properties of the quark scattering against a much more massive object. η_{lj} is an ideal variable for signal discrimination since:

- it is a simple kinematic variable, not requiring any high level object reconstruction,
- it has a very characteristic shape for the signal and backgrounds as well, granting a good discriminating power,
- it has low model dependance.

Therefore we use it in an unbind maximum likelihood fit to extract the signal yield.

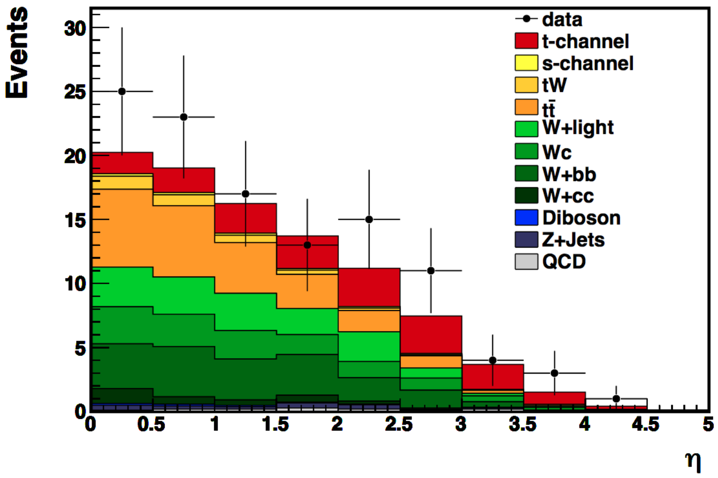

Figure 32: Pseudorapidity of the untagged jet (η_{lj}).

W **MASS** An obvious feature of the signal is the presence of a top quark, recognizable from a mass peak when properly combining the final state objects. The first step in the reconstruction of the top quark from its decay products is the reconstruction of the *W* boson. We assume that the x and y components of the missing energy are entirely due to the escaping neutrino, and apply the *W* mass constraint in order to extract the z component:

$$m_W^2 = \left(E_e + \sqrt{(\not{E}_T^2 + P_{z,\nu}^2)}\right)^2 - (P_{T,e} + \not{E}_T)^2 - (P_{z,e} + P_{z,\nu})^2. \quad (66)$$

In general, this equation has two solution for $P_{z,\nu}$. If they are both real, we choose the one with the small absolute value of $P_{z,\nu}$. If the discriminant is negative the solutions have an imaginary part. An extensive treatment of this case can be found in [?].
If they are both real, we choose the one with the small absolute value of $P_{z,\nu}$. A similar ambiguity is however always present when reconstructing a top-quark, since two jets are selected. The ambiguity is resolved by assigning the b-tagged jet to the top-quark decay.

TOP QUARK MASS Figure 33 shows the mass of the reconstructed top quark ($m_{bl\nu}$) for events passing the baseline selection. $t\bar{t}$ events present a peak at top mass which is broader with respect to signal events. In semileptonic $t\bar{t}$ events this is mainly due to the fact that two b quark from top quark decay are present, so the b-tagged used for top reconstruction jet has roughly 50% chance to stem from the same top quark decay as the lepton. On the other hand in $t\bar{t} \rightarrow 2l$ events (including tauons) the missing energy gets contributions by more than one neutrino.

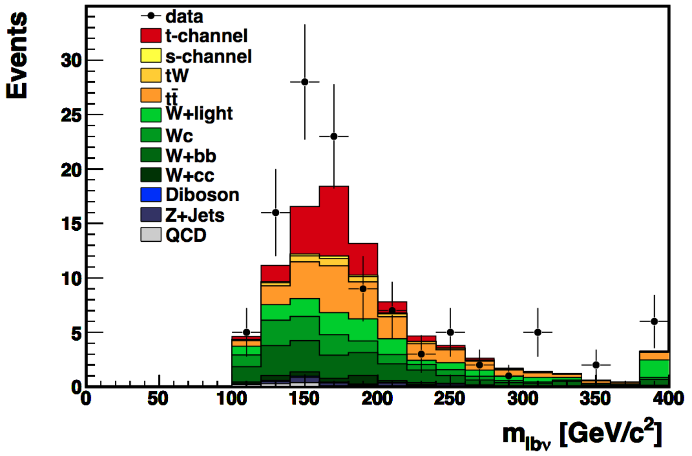

Figure 33: Reconstructed top-quark mass after the full selection.

TOP QUARK POLARIZATION ANGLE The V−A structure of the weak interaction, causes the top (anti-top) quark to have an almost 100% left(right)-handed polarization with respect to the spin axis [78]. Angular correlations in the top quark decay products keep track of the top quark spin direction. We can write:

$$\frac{1}{\Gamma}\frac{d\Gamma}{d\Gamma\cos\theta^*} = \frac{1}{2}(1 + A\cos\theta^*), \tag{67}$$

where θ^* is the angle between the direction of the outgoing particle and the spin axis, in the top-quark rest frame. A is a coefficient of spin asymmetry, which depends on the identity of the particle and is equal to +1 for charged leptons. We make use of the "spectator basis" (see, *e.g.*, [78]), where θ^* the angle θ^*_{lj} between the lepton momentum and the light quark momentum, in the top quark rest frame. We reconstruct this observable taking the direction of the untagged jet is chosen as spin axis and the boost in the top quark rest frame is performed taking the 4-momentum of the top from our reconstruction.

In Figure 34 the distribution of the $\cos\theta^*$ variable. The dip at $\cos\theta^* \approx 1$ is mainly due to the particular muon requirements: the distance ΔR in the $\eta - \phi$ plane between the muon and the light jet in fact cannot be $\Delta R < 0.3$ due to explicit selection requirements and to Iso_{rel} cuts. The sensitivity of the shape of this variable to some modeling effects, have been studied at generator level in [72], and after full reconstruction in previous Monte Carlo studies.

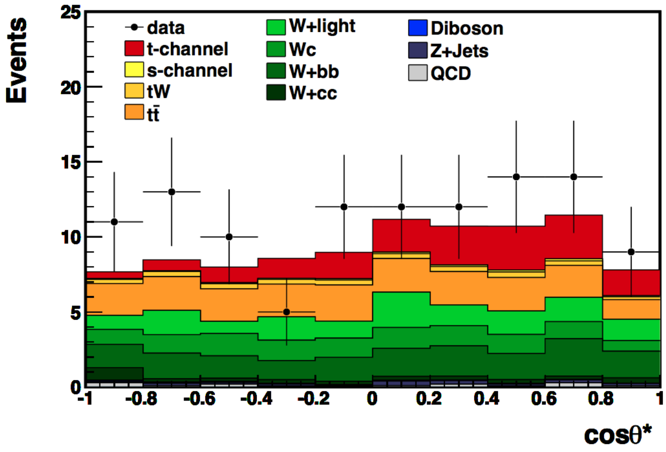

Figure 34: Pseudorapidity of the untagged jet (η_{lj}).

4.4 BACKGROUND DESCRIPTION AND ESTIMATION

4.4.1 W+jets control sample

W+jets events surviving the baseline selection result from a mixture of W+light partons (u, d, s, g) events and W+heavy partons (c, b) events. The W+jets enriched sample is defined requiring exactly 2 jets, but vetoing any b-tagged jet. This sample is also referred to as the 2J0T sample. Figures 35(a) and 35(b) show the muon p_T and relative isolation distributions, showing a discrepancy in the region where QCD is more abundant.

Figures 35(c) and 35(d) show the missing transverse energy and the W transverse mass distributions. We observe a better data-MC agreement in the latter, however in both cases it has to be noted that the most of the disagreement comes from the low MET region where most of the QCD is located. The treatment of QCD will be described in next section, allowing to determine from data the QCD yield.

Another important variable for the analysis is the reconstructed top mass, for which a jet has to be chosen for the top quark decay ansatz. In this sample, the jet with highest value of b-tagging algorithm is chosen. The reconstructed top mass is shown in Figure 35(e).

4.4.2 QCD control sample

The QCD component is estimated directly from data by a cut-based data-driven method.

1. For each sample a corresponding QCD enriched control sample is defined inverting the isolation cut.
2. R is defined as the ratio between the integral of the $m_T >$ 50GeV region and the $m_T <$ 50GeV region which is mostly populated by QCD events.
3. Then, for each sample, the amount of QCD (N_{QCD}) is determined in the region below $m_T <$ 50GeV by taking the difference between data and *non*-QCD processes.
4. The amount of QCD is taken as: $N_{QCD} \cdot R$.

Finally, the η distribution from the QCD enriched control sample is scaled to the yield obtained with the procedure described above. The resulting distribution is taken as data-driven QCD

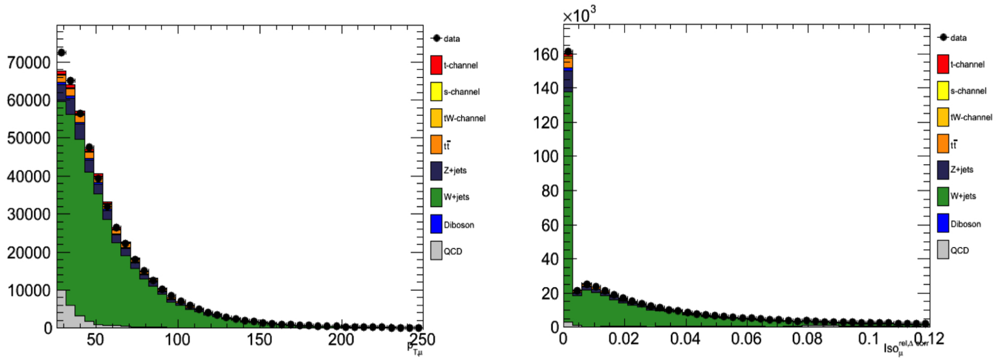

(a) Muon p_T

(b) Muon relative isolation

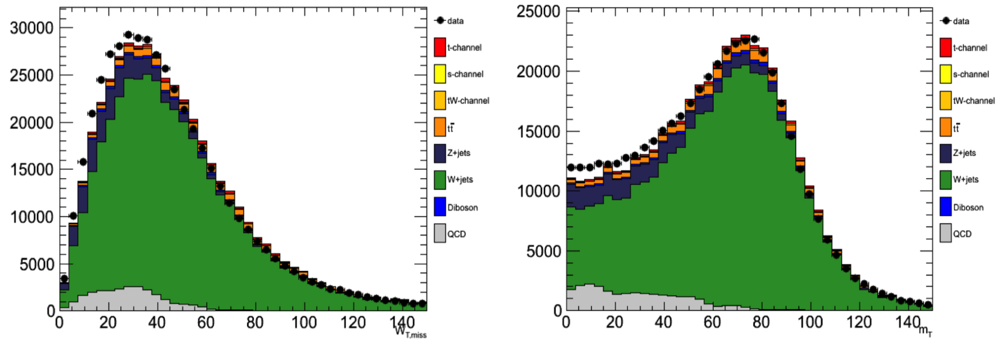

(c) $\not{E}_{\mathrm{T}}$

(d) W transverse mass

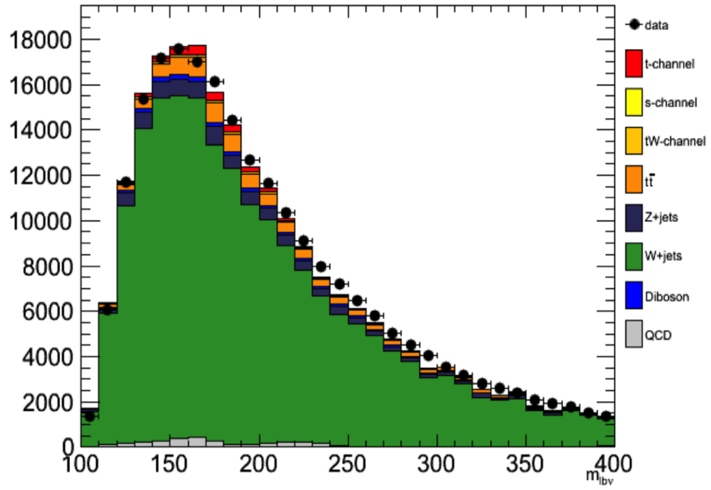

(e) Top reconstructed mass, $m_{l\nu b}$

Figure 35: Peculiar distribution in the W+jets enriched sample, 2JoT.

distribution and used later on in the analysis.

4.4.3 $t\bar{t}$ control sample

$t\bar{t}$ is in general the dominant process in the 3-jets samples with 1 or more b-tags, and is also the main background to the t-channel in the 2-jets 1-tag category. Two meaningful $t\bar{t}$-enriched control samples are therefore used: the 3-jets, 1-tag and 3-jets, 2-tags samples.

The additional cuts in $p_T > 60$ and RMS of the leading and second-to-leading jet defined in [**?**] are applied as well. The QCD yield here is taken from simulation. Figures 36 show the distribution of the light jet η for both control samples, normalized to the data integrated luminosity.

Figures 37 show the distribution of the top mass and the peak which is mostly populated by to semi-leptonic events where the b-tagged jet coming from the same top quark as the lepton is chosen, similarly to what happens with single top t-channel events.

Figure 38 shows the agreement in the signal and sideband region for $|\eta_j^{'}|$ in the 3J2T sample. To cope with any possible modeling effect, we get a reweighting function for the overall η distribution of the light jet taking the bin-by-bin difference between data and MC.

To extract a reweighting function in the 2J1T category, where we intend to perform the signal extraction, we first compare the light jet η distribution in the 3J1T and 3J2T categories to the one from the 2J1T, finding that the 3J2T region displays a similar η distribution as the one in the 2J1T sample, as can be seen in Figure 39. A reweighting function is extracted, taking the difference in shape between data and expectation.

4.4.4 W+jets extraction

In order to keep the W+jets contamination under control in the signal sample (2J1T), an extra cut in $m_{l\nu b}$ is performed, defining a signal region (SR) for events which have $130 < m_{l\nu b} < 220$. Events outside this region form the sideband region (SB). The discrepancy between data and Monte Carlo samples in the sideband region is attributed to the modelling of W+jets . In order to solve this issue, we use a data driven method to extract the W+jets distribution from the sideband. First we extract the

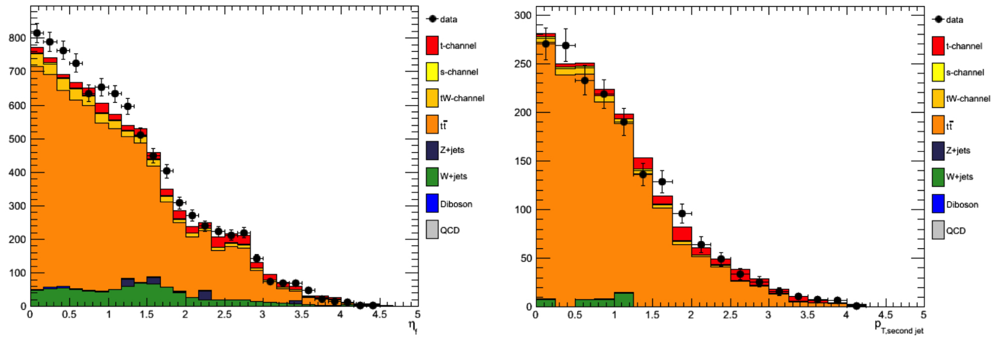

(a) 3J1T **(b)** 3J2T

Figure 36: Distribution of η of the jet with the lowest value of b-discriminator in the $t\bar{t}$ enriched samples with 1(a) or 2(b) tags.

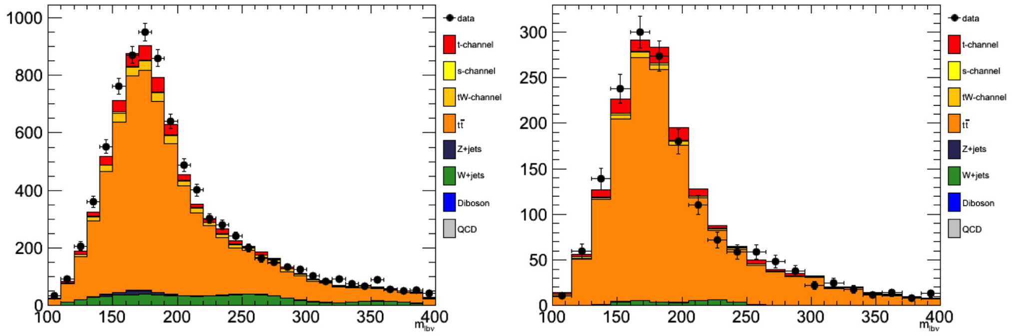

(a) 3J1T **(b)** 3J2T

Figure 37: Distribution of $m_{l\nu b}$ in the $t\bar{t}$ enriched samples with with 1(a) or 2(b) tags.

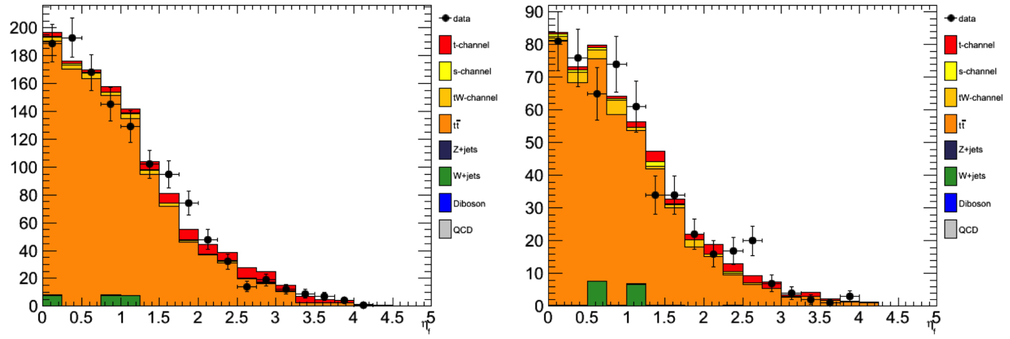

(a) Signal Region **(b)** Sideband Region

Figure 38: Distribution of η of the jet with the lowest value of b-discriminator in the $t\bar{t}$ enriched samples with 3J2T sample inside(a) and outside(b) the $130 < m_{l\nu b} < 220$ region.

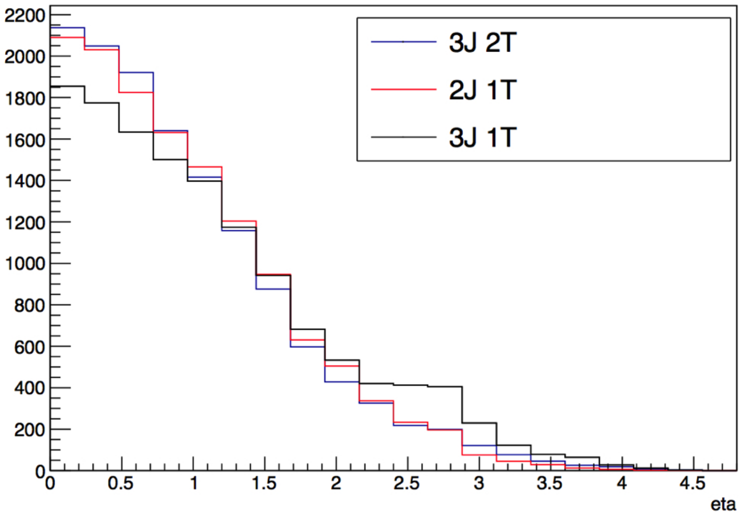

(a) Signal Region

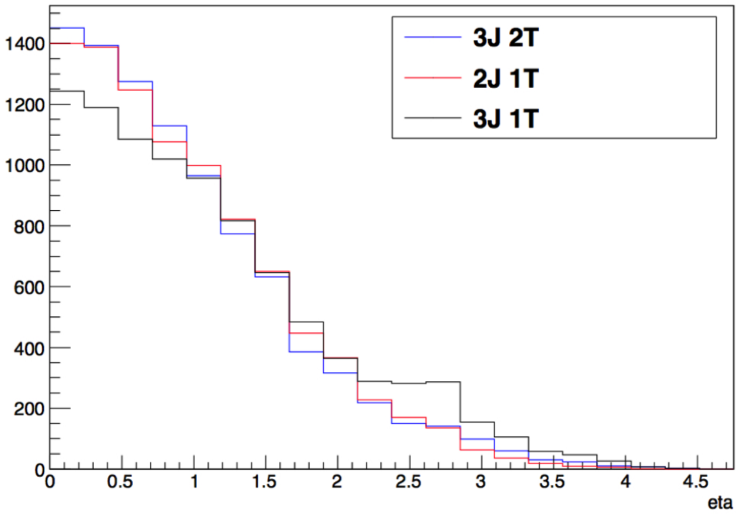

(b) Sideband Region

Figure 39: Comparison of the MC distribution of $|\eta|$ of the jet with the lowest value of b- discriminator in the $t\bar{t}$ enriched samples with with 1 or 2 tags versus the same distribution for the 2J1T category for $t\bar{t}$ events inside (a) and outside (b) the $130 < m_{l\nu b} < 220$ region.

shape and the yield and the $|\eta_{j'}|$ distribution for W+jets in the sideband region. We take the $|\eta_{j'}|$ distribution for the data sample and subtract QCD component determined previously from data (see Section 4.4.2); we then subtract the data-driven $t\bar{t}$ (see Section 4.4.3). The single-top tW, s-channels, and VV contributions are taken from simulation and subtracted. Finally, we also subtract the single-top t-channel, assuming its expected cross section from the SM prediction. What remains is taken as data-driven $|\eta_{j'}|$ distribution from the W+jets component.

Then, we apply the scale factor and $|\eta_{j'}|$ distribution obtained from the previous step to the signal region. This is used for the fit described later on.

Figure 40 shows that the agreement in the 2J1T region between the W+jets shape of the signal and sideband region is good, as the two distributions yield a Kolmogorov-Smirnov p-value of > 90%.

Figure 41 shows the distribution of the light jet $|\eta_{j'}|$ in the top mass sideband region. The mismodeling in $|\eta_{j'}|$ is partially attributed to the W+jets, as it is known that the W+heavy flavours component is significantly different from the Standard Model prediction. On top of that, the small amount of simulation data affects the expected shape.

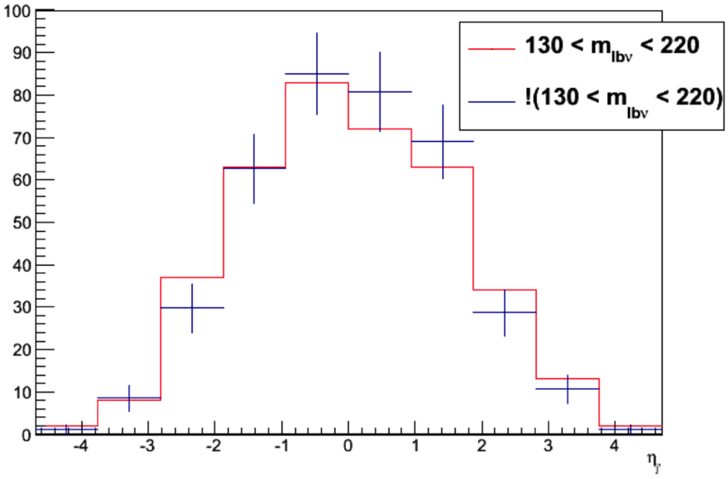

Figure 40: Pseudorapidity distribution of light jets for the W+jets samples inside (red) and outside (blue) the $130 < m_{l\nu b} < 220$ region,

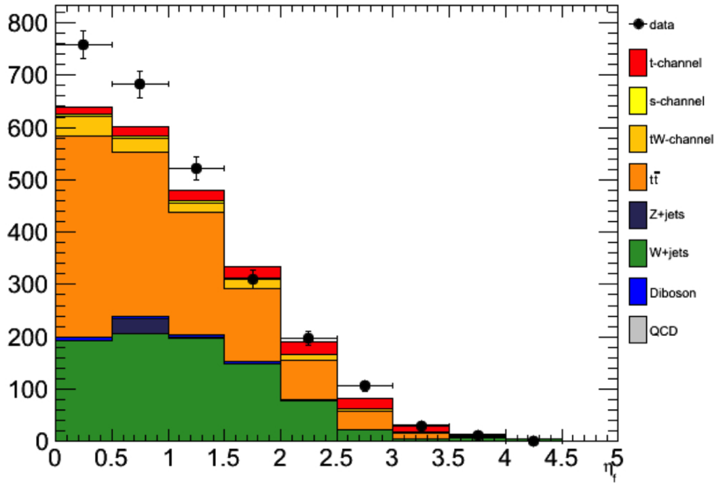

Figure 41: $|\eta_{j'}|$ distribution in the SB region of the 2J1T sample normalized to the data luminosity.

4.5 INCLUSIVE CROSS SECTION EXTRACTION

To measure the single-top t-channel inclusive cross-section a binned maximum likelihood fit is performed on the $|\eta_{j'}|$ distribution. The free parameters of the fit are the yields of the t-channel signal, the yields of the electroweak backgrounds (W/Z+jets, Diboson), and the yields of the top backgrounds ($t\bar{t}$, tW, and s single top channels), while the yield of the QCD is constrained to the value obtained from the control samples in data and the corresponding uncertainty is propagated as systematic uncertainty. The background components are treated separately in the fit in order to reduce the effect of the uncertainties of the individual yield SM predictions. We define the following extended likelihood function:

$$L = (N_s, N_b|\eta_1, ..., \eta_n) = \\ e^{-(N_s+\sum_b N_b)} \prod_{k=1}^{n} \left(N_s \cdot P_s(\eta_k) + \sum_b (N_b \cdot P_b(\eta_k)) \right), \quad (68)$$

where the subscript b labels the different background components ($b = EWK, top, QCD$), N_s and N_b are the yields of signal and backgrounds, n is the number of observed events, and P_s, P_b, , are the probability density functions (pdf) for the signal and the backgrounds. P_s is taken from Monte Carlo simulation.

The pdf for top backgrounds, *i.e.* $t\bar{t}$, tW and s single top channels, P_{top}, is obtained correcting bin by bin the Monte Carlo shape

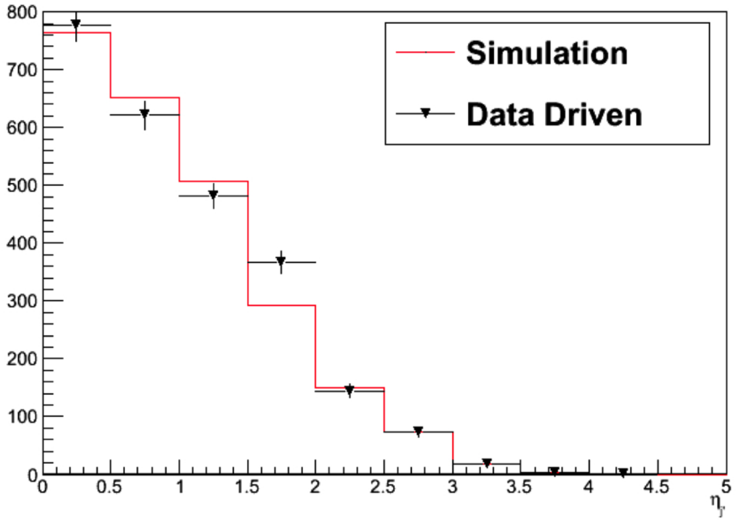

(a) $t\bar{t}$

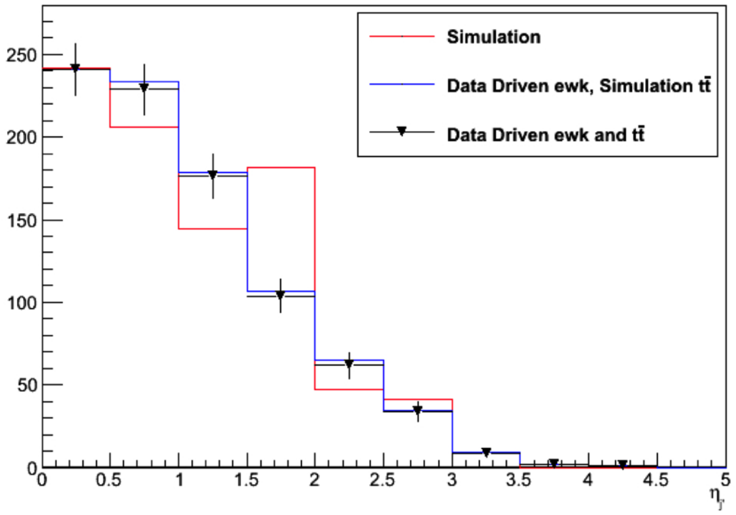

(b) W+jets

Figure 42: Pseudorapidity distribution of light jets for the $t\bar{t}$ and W+jets extracted using data driven techniques in the 2J1T signal region compared to MC expectations.

using the data-driven scale factor calculated with the method explained in Section 4.4.3 . Figure 42(a) shows the comparison between $t\bar{t}$ shape from Monte Carlo (continuous line) and the data-driven shape (triangles).

The electroweak pdf, P_{EWK} is derived with the data-driven method (see Section 4.4.4) taking into account the data-driven pdfs for $t\bar{t}$ and for QCD. Figure 42(b) shows the EWK shape taken from simulation (red line), the one extracted with the data driven technique using $t\bar{t}$ from simulation (blue line), and $t\bar{t}$ from the data driven technique (triangles).

N_s and the various N_b are determined from the fit assuming the pdf to be fixed. It is convenient to define the signal strength S_s, the electroweak strength S_{EWK}, and the top strength S_{top} as the ratios of the measured (N_i) and expected (N_i^{exp}) yields, with $i = s, EWK, top$:

$$S_i = N_i / N_i^{exp}. \tag{69}$$

The fitted $|\eta_{j'}|$ distributions are shown in Figures 43, while the fitted signal strenghts are:

$$S_s = 1.02 \pm 0.06, \quad S_{EWK} = 1.23 \pm 0.22, \quad S_{top} = 0.86 \pm 0.08.$$

A gaussian constraint is put on the S_{top} parameter, *i.e.* we assume a prior gaussian probability distribution with mean and width given by the Standard Model predictions.

A gaussian constraint is also imposed to the S_{EWK} parameter. In this case the width of the prior distraction in set to twice the difference between the data-driven $W+$jets (see Section ...) and the normalization obtained from the Standard Model prediction.

The results reported above have to take into account systematics uncertainties among which those on the estimate of the $W+$jets and $t\bar{t}$ background from data.

The cross-section of the single-top production in the t-channel is related to the signal yield by the formula:

$$\sigma_t = \frac{N_s}{\epsilon \cdot B(t \to l\nu b) \cdot L} \tag{70}$$

where ϵ is the signal selection efficiency, $B(t \to l\nu b) = 0.1080$ [**?**] is the leptonic branching fraction for the top quark leptonic decay and $L = 5041$ pb^{-1} is the integrated luminosity. The resulting cross-section is therefore:

$$\sigma_t^{exp} = 88.9 \pm 5.4pb \tag{71}$$

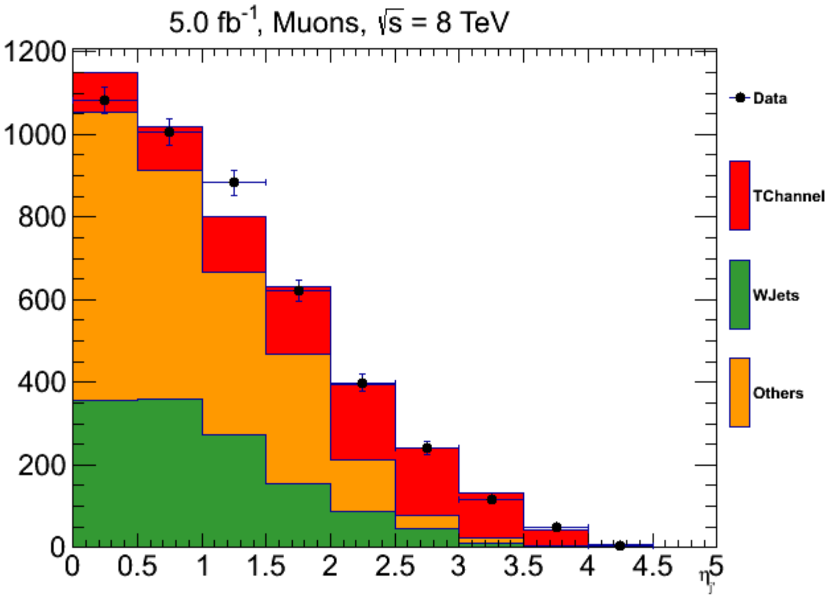

Figure 43: $|\eta_{j'}|$ distribution, normalized with the yields obtained from the fit.

4.6 CHARGE ASYMMETRY MEASUREMENT

A distinct feature of the t-channel is the asymmetry in the production of top and antitop quarks. According to [82] the expected value for the cross-sections are:

$$\begin{aligned} \sigma^{SM}_{top} &= 56.4^{+2.1}_{-0.3}(\text{scale}) \pm 1.1(\text{pdf})pb \\ \sigma^{SM}_{antitop} &= 30.7 \pm 0.7(\text{scale})^{+0.9}_{-1.1}(\text{pdf})pb \end{aligned} \tag{72}$$

The top quark inherits the sign of the charge from the light quark (u,d,s) involved in the hard scattering as shown Figure 29. Thus the asymmetry is a consequence of the contribution of the u quarks being greater with respect to the one from d quarks because of the parton distribution functions of the proton. The aim of this work is to measure σ_{top} and $\sigma_{antitop}$ doing a simultaneous extraction of the positively and negatively charged top quark.

The selection and the counting of the samples are done in the same way as described in Section 4.2, splitting the samples in two according to the charge of the lepton in the final state.

4.6.1 Samples divided by charge

The discriminating variables for different backgrounds have different behaviors with respect to the charge of final state lepton.

In the following these differences will be described in details.

w+JETS CONTROL SAMPLE Due to the different contributions of the u and d quarks proton pdfs, W+jets processes are not symmetric as function of the lepton charge. This feature can be clearly seen in data: Figure 44(a) shows the lepton charge distribution in the sample for muons. We see that the asymmetry in data tends to be different with respect to the prediction, thus in the signal extraction procedure the W+jets asymmetry shall be measured simultaneously to R_t-channel. Figures 44(b), 44(c) and 44(d), 44(e) show the distributions of light jet η and $m_{l\nu b}$ divided by charge.

$t\bar{t}$ CONTROL SAMPLE These backgrounds are expected to be symmetric, and this can be checked in data on those control samples. Figure 45 shows the lepton charge normalized to the data yield obtained for the sake of displaying this feature. Figures 46 and 47 show the behavior of the light jet η and of the reconstructed top mass $m_{l\nu b}$ for positive and negative charge leptons. A reweighting function is extracted from the signal and sideband regions of the 3J2T sample. This extraction is performed exactly as described in Section 4.4.3 . The extracted function is then applied to the $t\bar{t}$ Monte Carlo distribution in the signal region. Since the $t\bar{t}$ sample is symmetric as a function of the charge, we perform the extraction before separating by charge. Figure 48shows that, according to simulation, the top model for light jet η is independent of the charge of the lepton.

SIGNAL SAMPLE Following the prescription given in Section 4.4.4 the 2J1T sample in divided in Signal and in Sideband Region performing a cut in the reconstructed top mass, $m_{l\nu b}$. Then the data-driven W+jets distribution is extracted from the Sideband Region subtracting the signal and other background processes. Figure 49 shows the agreement in the 2J1T region between the W+jets shape of the signal and sideband region for muons with positive and negative charge.

4.6.2 Likelihood fit

To measure the single-top t-channel inclusive cross-section a binned maximum likelihood fit is performed on the $|\eta_{j'}|$

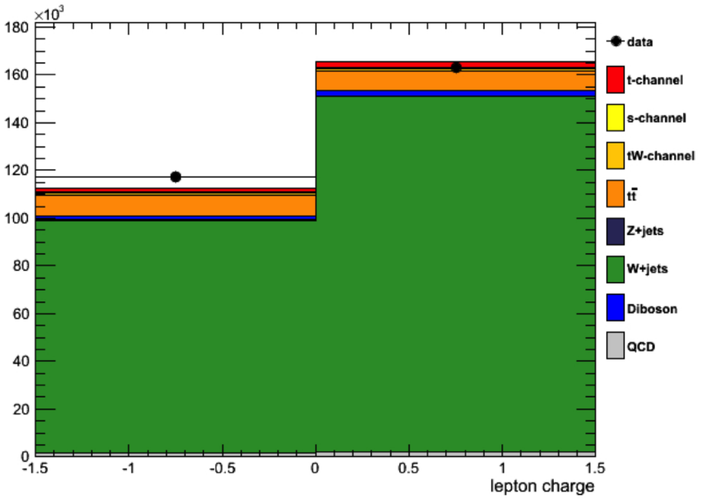

(a) lepton charge

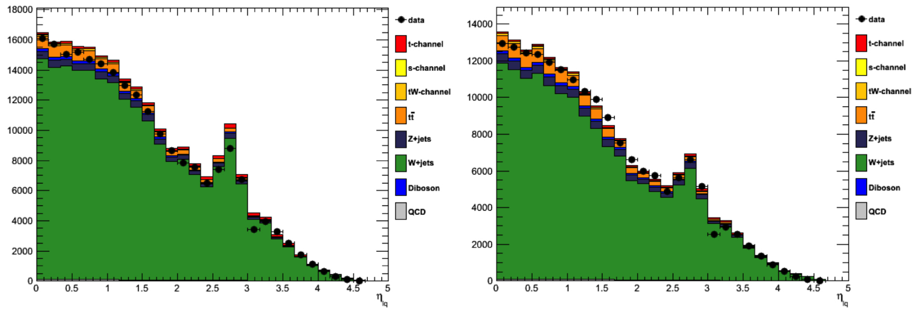

(b) $\eta_{j'}$ (positive charge) **(c)** $\eta_{j'}$ (negative charge)

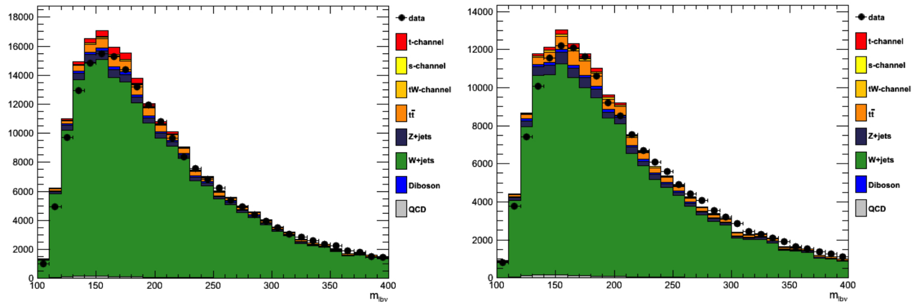

(d) $m_{l\nu b}$ (positive charge) **(e)** $m_{l\nu b}$ (negative charge)

Figure 44: Distributions in 2JoT sample. In particular: lepton charge (a); $m_{l\nu b}$ distributions for positive(b) and negative (c) charge leptons; pseudorapidity distribution of light jets η for positive(d) and negative (e) charge leptons. Simulation normalized to the data yield.

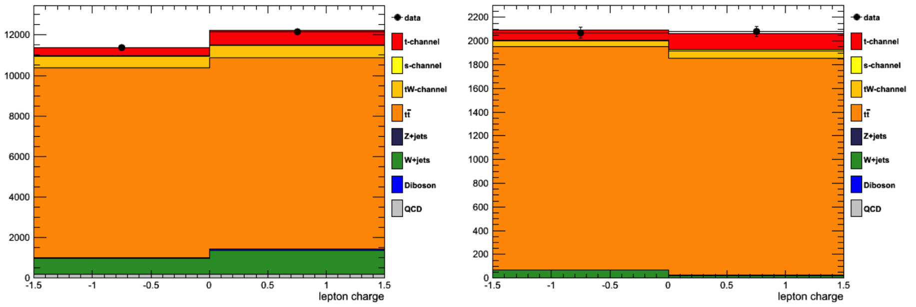

(a) 3J1T **(b)** 3J2T

Figure 45: Lepton charge in the 3J1T(a) and 3J2T(b). Simulation normalized to the data yield.

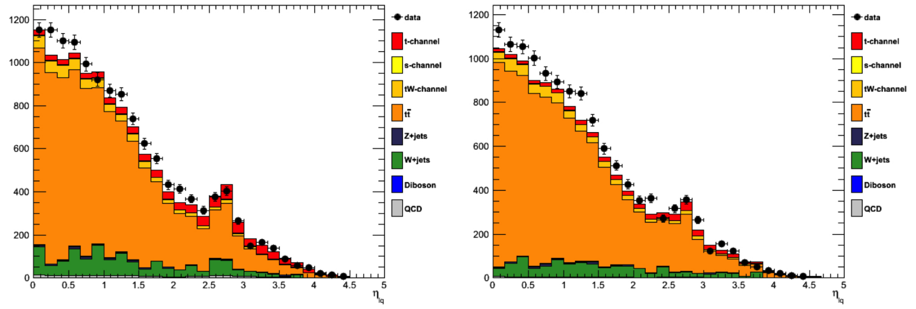

(a) 3J1T positive charge **(b)** 3J1T negative charge

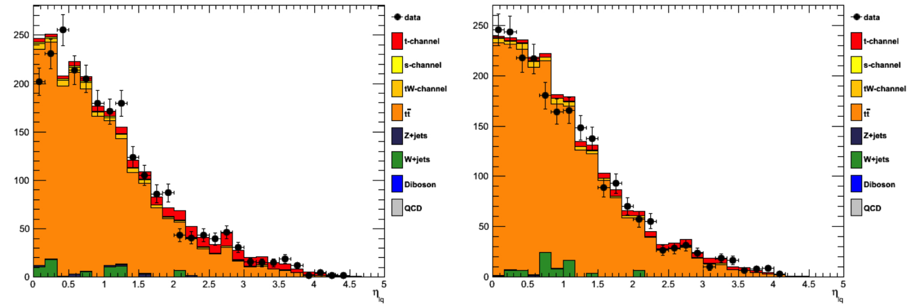

(c) 3J2T positive charge **(d)** 3J2T negative charge

Figure 46: Pseudorapidity distribution of light jets η for positive(a,c) and negative (b,d) charge leptons in the 3J1T (a,b) and 3J2T (c,d) samples.

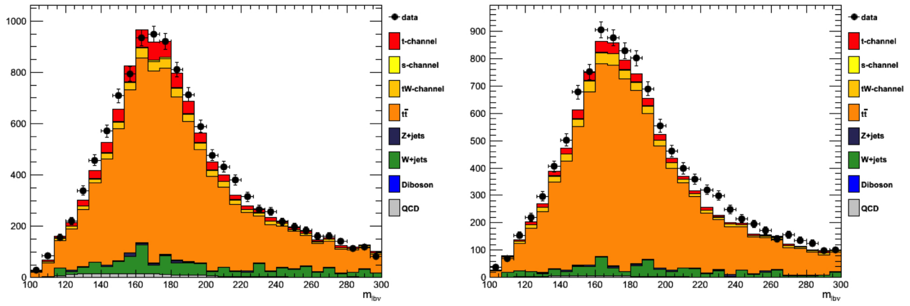

(a) 3J1T positive charge **(b)** 3J1T negative charge

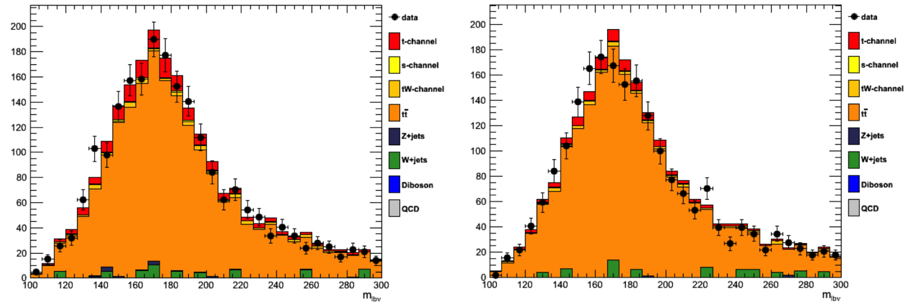

(c) 3J2T positive charge **(d)** 3J2T negative charge

Figure 47: $m_{l\nu b}$ distributions for positive(a,c) and negative (b,d) charge leptons in the 3J1T (a,b) and 3J2T (c,d) samples.

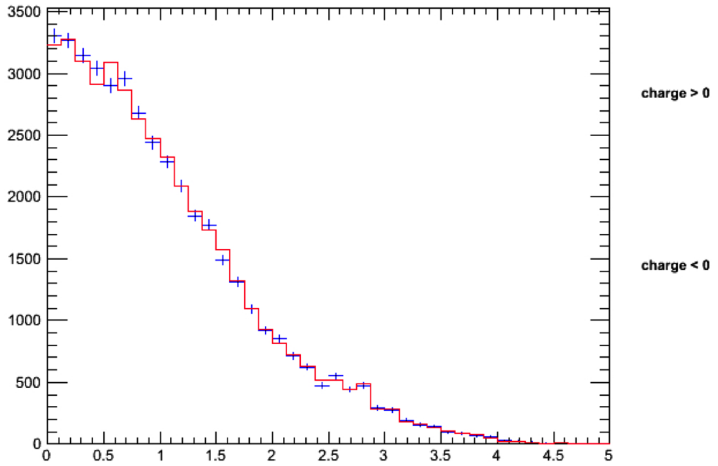

Figure 48: Comparison between the light jet η distributions of samples with positive and negative leptons in the $t\bar{t}$ enriched samples with 3J2T.

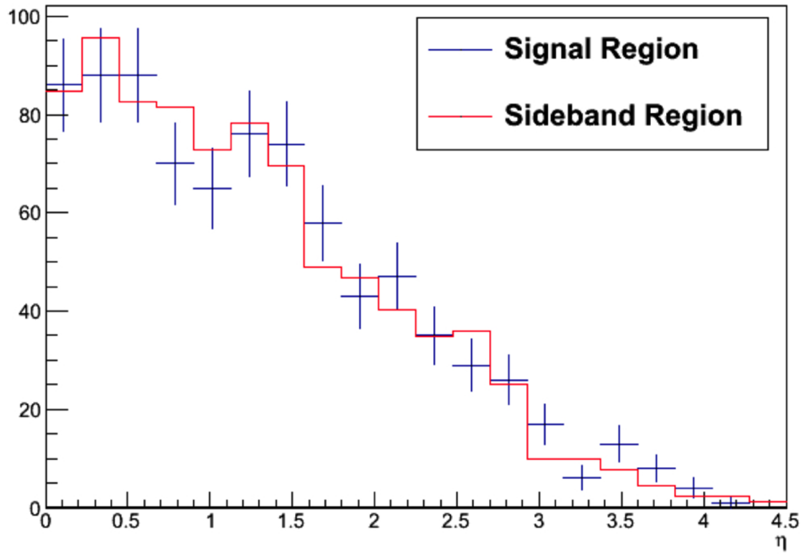

(a) positive charge

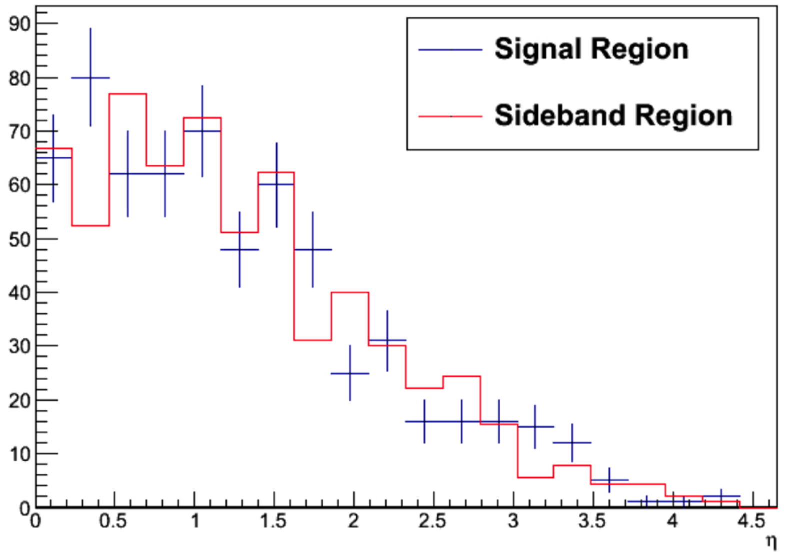

(b) negative charge

Figure 49: Pseudorapidity distribution of light jets η for W+jets samples inside (red) and outside (blue) the $130 < m_{l\nu b} < 220$ region, for muons with positibe (a) and negative (b) charge.

distribution. The free parameters of the fit are the yields of the t-channel signal, the electroweak backgrounds (W/Z+jets, Diboson), and the top backgrounds ($t\bar{t}$, tW, and s single top channels), while the QCD is constrained to the value obtained from the control samples in data and the corresponding uncertainty will be propagated as systematic uncertainty.
As we did for the inclusive cross section measurement, we define the following extended likelihood function:

$$L = L^{+} \cdot L^{+} \tag{73}$$

where $L^{+(-)}$ is the likelihood functions for events with positive (negative) final state lepton. $L^{+(-)}$ have the same form of the likelihood previously defined for the inclusive cross section measurement (see Equation 68)
Following the procedure applied before (see Section 4.5) define the signal strength S_s, the electroweak strength S_{EWK}, and the top strength S_{top} as the ratios of the measured (N_i) and expected (N_i^{exp}) yields, with $i = s, EWK, top$:

$$S_i = N_i / N_i^{exp},$$

with $i = s^+, s^-, EWK^+, EWK^-, top$, and . The fitted $|\eta_{j'}|$ distributions are shown in Figures 50. The fitted parameters are $S_{s,-}$, $S_{s,+}$, $S_{EWK,-}$, $S_{EWK,+}$, S_{top}.

Since the $t\bar{t}$ background is symmetric with respect to the charge of the final state lepton, instead of using two different prior distribution for positive and negative charge we simply use half of the total distribution. As described in Section 4.5 , a gaussian constraint is put on S_{top} and S_{EWK}. The fitted signal strenghts are:

$$\begin{aligned} S_{s,+} &= 0.83 \pm 0.14 \\ S_{s,-} &= 1.19 \pm 0.17 \\ S_{EWK,+} &= 0.69 \pm 0.23 \\ S_{EWK,-} &= 0.71 \pm 0.21 \\ S_{top} &= 0.99 \pm 0.08 \end{aligned}$$

4.6.3 Results

The measured cross section for the top and antitop t-channel are:

$$\begin{aligned} \sigma_{top}^{exp} &= 46.8 \pm 7.9 pb \\ \sigma_{antitop}^{exp} &= 36.5 \pm 5.3 pb \end{aligned} \tag{74}$$

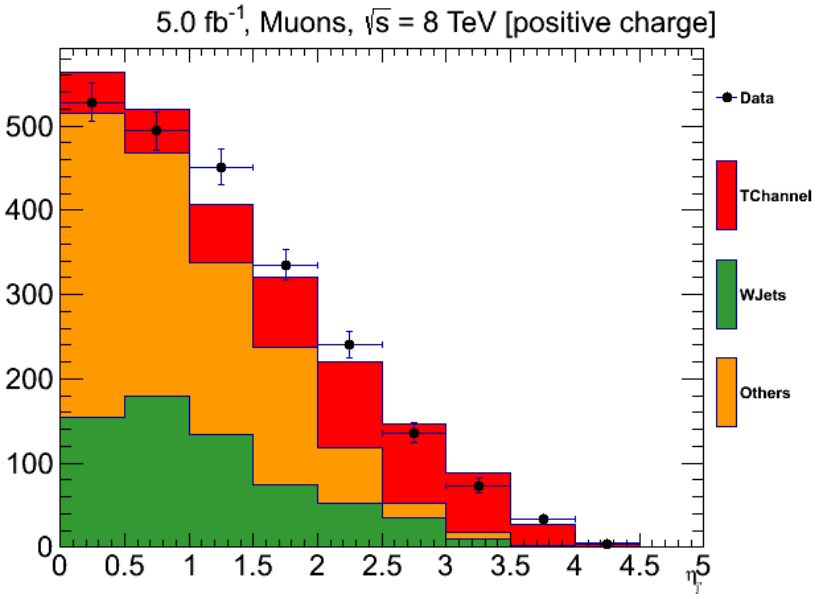

(a) positive charge

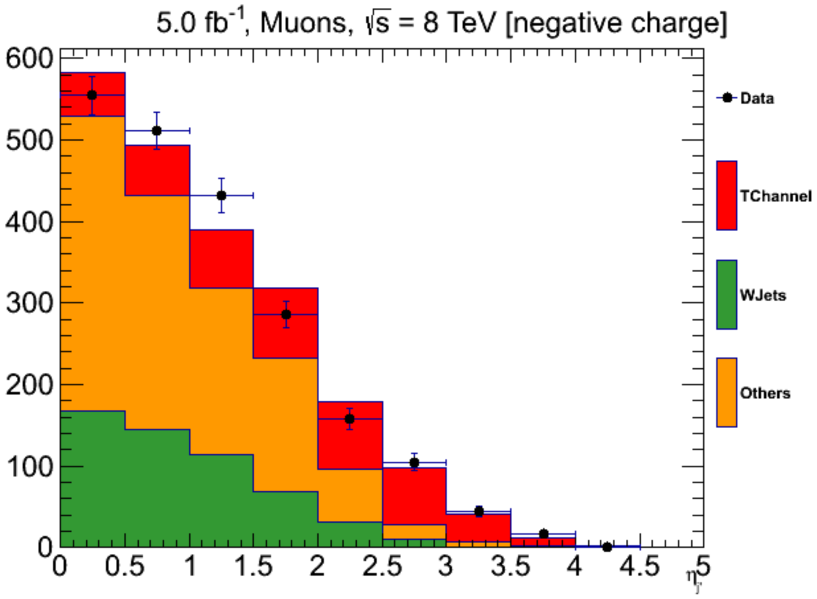

(b) negative charge

Figure 50: Fitted pseudorapidity distribution of light jets η for muons with positive (a) and negative (b) charge.

4.7 SYSTEMATIC UNCERTAINTIES

The systematic uncertainties haven't been treated extensively in this thesis work. Their effect on the measurement is comparable to the statistical uncertainties which dominate at the luminosity of the data-sample used for the analysis. For comprehensiveness, the procedure followed to estimate the systematic uncertainties for CMS public charge asymmetry measurements [86], are explained in this section.

Each systematic uncertainty is evaluated by performing pseudo-experiments which take into account the effect of the corresponding systematic source on the distribution of $\eta_{j'}$ and on the event yield of the physics processes. A fit to $\eta_{j'}$ is then performed on each pseudo-experiment and the mean shift of the fit results with respect to the value obtained in the nominal scenario is taken as the corresponding uncertainty. Among all the possible sources of systematic uncertainties the following are the most important:

- W+jets and $t\bar{t}$ models: the uncertainty related to the W+jets and $t\bar{t}$ extraction method from data is evaluated by generating pseudo-experiments in the SB and in the 3J2T sample, thus performing the template extraction procedure which assumes the same shape in the SR and SB region for the backgrounds and repeating the fit to $\eta_{j'}$ .The uncertainty is taken as the root mean square of the distribution of fit results obtained in this way. This uncertainty depends on the amount of available data it the SB and in the 3J2T sample. In addition, alternative $\eta_{j'}$ shapes are derived in the simulation by varying the $Wb + X$ and $Wc + X$ fractions of the background by factors of $\pm 30\%$ independently in the SR and SB regions. The fit procedure was repeated with the alternative shapes and the maximum difference in the result with respect to the central value was added in quadrature to the other uncertainties.
- Jet energy scale (JES): all reconstructed jet four-momenta in simulated events were simultaneously varied according to the η and p_T dependent uncertainties on the jet energy scale [83]. This variation in jet four-momenta is also propagated to $\not{E}_{\mathrm{T}}$.
- b-tagging and misidentification efficiencies are estimated from control samples in 7 TeV data [84], and the light-parton misidentification efficiencies are remodeled to take into account the extrapolation from 7 to 8 TeV. Scale factors are applied to the simulated samples to reproduce efficiencies in data and the corresponding uncertainties, enlarged by a

factor 1.5 in order to cover possible extrapolation errors from 7 to 8 TeV, are propagated as systematic uncertainties.

- Luminosity: the luminosity is known with a relative uncertainty of ±4.4% [80].

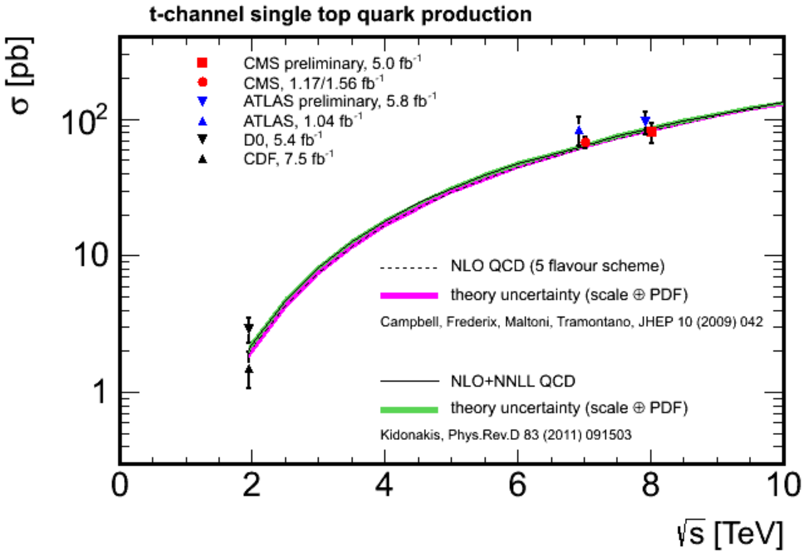

(a) Inclusive cross section

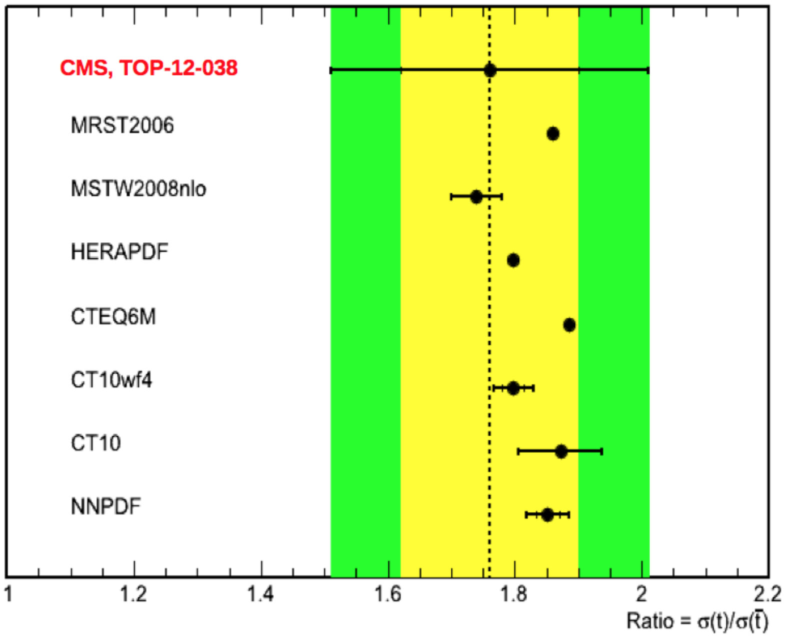

(b) Charge asymmetry ratio

Figure 51: Figure (a) shows the single top cross section in the t-channel versus centre-of-mass energy, comparing this measurement with the previous t-channel cross section measurement at 7 TeV [79] and at Tevatron [67]and with the QCD expectations computed at NLO [80] and at NLO+NNLL [71]. In Figure (b) the comparison of the measured R with the predictions obtained with several pdf sets is shown.

CONCLUSIONS

This thesis has presented a data analysis work performed in the context of the CMS experiment and aimed at measuring the inclusive cross section and the charge asymmetry of single top produced in t-channel and decaying through $t \rightarrow Wb \rightarrow e\nu b$ The main analysis is based on a subset of the data collected by CMS in 2012 at $\sqrt{s} = 8TeV$, corresponding to an integrated luminosity of 5 fb^{-1}.

The topology of the process and the spin correlations between the particles involved allow to perform a very tight selection. Furthermore, data-driven techniques have been set up for a reliable estimation of the main backgrounds (QCD multi-jet, W+jets, $t\bar{t}$) to the signal of interest. Different sources of systematic uncertainties have been taken into account, both of instrumental and physics origin, among which the b-tagging uncertainty and background modeling. At the end the signal extraction is obtained from a template fit to the most discriminating variables. The single top t-channel cross section measured with the inclusion of systematics in the muonic channel is:

$$\sigma_t^{exp} = 88.9 \pm 5.4pb$$

While the Standard Model prediction [82] is:

$$\sigma_t^{SM} = 87.2^{+2.1}_{-0.7}(\text{scale})^{+1.5}_{-1.7}(\text{pdf})pb$$

The measurement has been updated with some small adjustments and the addition of systematics for the CMS PAS-TOP-12-011 [85], yielding a result of:

$$\sigma_t^{PAS} = 80.1 \pm 5.7(\text{stat}) \pm 11.0(\text{syst})pb \tag{75}$$

Figure 51(a) shows the comparison of the single top cross section in the t-channel versus centre-of-mass energy with the previous t-channel cross section measurement at 7 TeV [79] and at Tevatron [67] and with the QCD expectations computed at NLO [80] and at NLO+NNLL [71].

The cross-sections σ_{top} and $\sigma_{antitop}$ are measured doing a simultaneous extraction of the positively and negatively charged top quark:

$$\begin{aligned}\sigma_{top}^{exp} &= 46.8 \pm 7.9 pb\\ \sigma_{antitop}^{exp} &= 36.5 \pm 5.3 pb\end{aligned} \tag{76}$$

The results obtained are in agreement with the Standard Model prediction [82]:

$$\begin{aligned}\sigma_{top}^{SM} &= 56.4^{+2.1}_{-0.3}(\text{scale}) \pm 1.1(\text{pdf}) pb\\ \sigma_{antitop}^{SM} &= 30.7 \pm 0.7(\text{scale})^{+0.9}_{-1.1}(\text{pdf}) pb\end{aligned} \tag{77}$$

The measurement has been updated with some small adjustments and the addition of systematics for the CMS PAS-TOP-12-038 [86], yielding a result of:

$$\begin{aligned}\sigma_{top}^{PAS} &= 49.9 \pm 1.9(\text{stat}) \pm 8.9(\text{syst}) pb\\ \sigma_{antitop}^{PAS} &= 28.3.9 \pm 2.4(\text{stat}) \pm 4.9(\text{syst}) pb\end{aligned} \tag{78}$$

Is possible to define the ratio R between σ_{top} and $\sigma_{antitop}$. In Figure 51(b) is shown the comparison of the measured R with the predictions obtained with several pdf sets. The value of R is the one reported in the [86]: $R = 1.76 \pm 0.15(\text{stat}) \pm 0.22(\text{syst})$.

BIBLIOGRAPHY

[1] S. Glashow. Partial-symmetries of weak interactions. Nuclear Physics, 22:579-588, Feb 1961.

[2] Steven Weinberg. A model of leptons. Phys. Rev. Lett., 19:1264-1266, Nov 1967.

[3] N. Svartholm. Elementary particle theory: relativistic groups and analyticity. Nobel symposium

[4] F. Englert and R. Brout. Broken Symmetry and the Mass of Gauge Vector Mesons. Phys. Rev. Lett., 13:321-323, Aug 1964.

[5] Peter W. Higgs. Broken Symmetries and the Masses of Gauge Bosons. Phys. Rev. Lett., 13:508-509, Oct 1964.

[6] G. S. Guralnik, C. R. Hagen, and T. W. B. Kibble. Global Conservation Laws and Massless Particles. Phys. Rev. Lett., 13:585-587, Nov 1964.

[7] G. Zweig. An SU(3) model for strong interaction symmetry and its breaking. Technical Report CERN-TH-401, CERN, Geneva, Jan 1964.

[8] M. Y. Han and Y. Nambu. Three-triplet model with double SU(3) symmetry. Phys. Rev., 139:B1006-B1010, Aug 1965.

[9] O. W. Greenberg. Spin and Unitary Spin Independence in a Paraquark Model of Baryons and Mesons. Phys. Rev. Lett., 13:598-602, Oct 1964.

[10] H. David Politzer. Reliable Perturbative Results for Strong Interactions. Phys. Rev. Lett., 30:1346-1349, Jun 1973.

[11] H. David Politzer. Asymptotic Freedom: An Approach to Strong Interactions. Phys.Rept., 14:129-180, Jul 1974.

[12] David J. Gross and Frank Wilczek. Ultraviolet Behavior of Non-Abelian Gauge Theories. Phys. Rev. Lett., 30:1343-1346, Jun 1973.

[13] K. Nakamura et al. (Particle Data Group). Review of particle physics. J. Phys. G: Nucl. Part. Phys., 37:075021, 2010.

[14] E. Stueckelberg. Die Wechselwirkungckracfte in der Electrodynamic und der Feldtheorie der Kernkraefle. Helvetica Physica Acta, 11:225-236, 1938.

[15] J. Schwinger. On Quantum-Electrodynamics and the Magnetic Moment of the Electron. Phys. Rev., 73:416-417, Feb 1948.

[16] J. Schwinger. Quantum Electrodynamics. I. A Covariant Formulation. Phys. Rev., 74:1439-1461, Nov 1948.

[17] R. P. Feynman. Space-Time Approach to Quantum Electrodynamics. Phys. Rev., 76:769-789, Sep 1949.

[18] R. P. Feynman. Space-Time Approach to Quantum Electrodynamics. Phys. Rev., 76:769-789, Sep 1949.

[19] R. P. Feynman. Mathematical formulation of the quantum theory of electro-magnetic interaction. Phys. Rev., 80:440-457, Nov 1950.

[20] S. Tomonaga. On a Relativistically Invariant Formulation of the Quantum Theory of Wave Fields. Progress of Theoretical Physics, 1(2):27-42, 1946.

[21] F. J. Dyson. The Radiation Theories of Tomonaga, Schwinger, and Feynman. Phys. Rev., 75:486-502, Feb 1949.

[22] F. J. Dyson. The S Matrix in Quantum Electrodynamics. Phys. Rev., 75:1736- 1755, Jun 1949.

[23] UA1 Collaboration. Further evidence for charged intermediate vector bosons at the SPS collider. Phys. Lett. B, 129:273-282, Sep 1983.

[24] UA1 Collaboration. Experimental observation of lepton pairs of invariant mass around 95 GeV/c2 at the CERN SPS collider. Phys. Lett. B, 126:398-410, Jul 1983.

[25] Antonio Pich. The Standard Model of electroweak interactions. Technical Report CERN-2012-001, CERN, Geneva, Feb 2012.

[26] E. Fermi. Versuch einer Theorie der ?-Strahlen. I. Zeitschrift fur Physik A Hadrons and Nuclei, 88:161-177, 1934.

[27] D. Hanneke, S. Fogwell, and G. Gabrielse. New Measurement of the Electron Magnetic Moment and the Fine Structure Constant. Phys. Rev. Lett., 100:120801, Mar 2008.

[28] T. D. Lee and C. N. Yang. Question of Parity Conservation in Weak Interactions. Phys. Rev., 104:254-258, Oct 1956.

[29] C. S. Wu, E. Ambler, R. W. Hayward, D. D. Hoppes, and R. P. Hudson. Experimental Test of Parity Conservation in Beta Decay. Phys. Rev., 105:1413-1415, Feb 1957.

[30] Nicola Cabibbo. Unitary Symmetry and Leptonic Decays. Phys. Rev. Lett., 10:531-533, Jun 1963.

[31] Makoto Kobayashi and Toshihide Maskawa. CP-Violation in the Renormalizable Theory of Weak Interaction. Progress of Theoretical Physics, 49(2):652- 657, 1973.

[32] B. Pontecorvo. Neutrino Experiments and the Problem of Conservation of Leptonic Charge. Soviet Journal of Experimental and Theoretical Physics, 26:984, May 1968.

[33] S. Fukuda et al. Determination of solar neutrino oscillation parameters using 1496 days of Super-Kamiokande-I data. Phys. Lett. B, 539(3-4):179 - 187, 2002.

[34] M. H. Ahn et al. Indications of Neutrino Oscillation in a 250 km Long-Baseline Experiment. Phys. Rev. Lett., 90:041801, Jan 2003.

[35] S. N. Ahmed et al. Measurement of the Total Active 8B Solar Neutrino Flux at the Sudbury Neutrino Observatory with Enhanced Neutral Current Sensi- tivity. Phys. Rev. Lett., 92:181301, May 2004.

[36] K. Eguchi et al. First Results from KamLAND: Evidence for Reactor Antineutrino Disappearance. Phys. Rev. Lett., 90:021802, Jan 2003.

[37] Ziro Maki, Masami Nakagawa, and Shoichi Sakata. Remarks on the Unified Model of Elementary Particles. Progress of Theoretical Physics, 28(5):870-880, 1962.

[38] S. L. Glashow, J. Iliopoulos, and L. Maiani. Weak Interactions with Lepton- Hadron Symmetry. Phys. Rev. D, 2:1285-1292, Oct 1970.

[39] ALEPH Collaboration, DELPHI Collaboration, L3 Collaboration, OPAL Collaboration, SLD Collaboration, LEP Electroweak Working Group, SLD Elec- troweak, and Heavy

Flavour Groups. Precision electroweak measurements on the Z resonance. Physics Reports, 427(5-6):257 - 454, 2006.

[40] CMS Collaboration. Observation of a new boson at a mass of 125 GeV with the CMS experiment at the LHC. Phys.Lett.B, 2012.

[41] ATLAS Collaboration. Observation of a new particle in the search for the Standard Model Higgs boson with the ATLAS detector at the LHC. Phys.Lett.B, 2012.

[42] J. H. Christenson, J. W. Cronin, V. L. Fitch, and R. Turlay. Evidence for the 2π Decay of the K20 Meson. Phys. Rev. Lett., 13:138-140, Jul 1964.

[43] S. W. Herb et al. Observation of a Dimuon Resonance at 9.5-GeV in 400-GeV Proton-Nucleus Collisions. Phys. Rev. Lett., 39:252-255, 1977.

[44] D0 Collaboration. Search for high mass top quark production in $p\overline{p}$ collisions at $\sqrt{s} = 1.8$ TeV. Phys. Rev. Lett. 74:2422-2426, 1995.

[45] CDF Collaboration. Observation of top quark production in $p\overline{p}$ collisions Phys. Rev. Lett., 74:2626-2631, 1995.

[46] Ling-Lie Chau and Wai-Yee Keung. Comments on the Parametrization of the Kobayashi-Maskawa Matrix. Phys. Rev. Lett., 53:1802-1805, Nov 1984.

[47] "LHC machine," Journal of Instrumentation 3 no. 08, (Aug., 2008) S08001. http://iopscience.iop.org/1748-0221/3/08/S08001.

[48] J. Caron, "Layout of the LEP tunnel including future LHC infrastructures," Feb., 1997. http://cdsweb.cern.ch/record/841560.

[49] ATLAS Collaboration, F. A. Conventi, "A measurement of the ATLAS di-muon trigger efficiency in proton-proton collisions at ps=7 TeV," in 2011 IEEE Nuclear Science Symposium and Medical Imaging Conference (NSS/MIC) Conference Record, pp. 904Ð907. IEEE, Oct., 2011. http://cdsweb.cern.ch/record/1401937.

[50] ATLAS Collaboration, G. Aad, et al., "The ATLAS experiment at the CERN large hadron collider," Journal of Instrumentation 3 no. 08, (Aug., 2008) S08003. http://iopscience.iop.org/1748-0221/3/08/S08003.

[51] CMS Collaboration, S. Chatrchyan, et al., "The CMS experiment at the CERN LHC," Journal of Instrumentation 3 no. 08, (Aug., 2008) S08004. http://iopscience.iop.org/1748-0221/3/08/S08004.

[52] ALICE Collaboration, K. Aamodt, et al., "The ALICE experiment at the CERN LHC," Journal of Instrumentation 3 no. 08, (Aug., 2008) S08002. http://iopscience.iop.org/1748-0221/3/08/S08002/.

[53] LHCb Collaboration, A. A. Alves, et al., "The LHCb detector at the LHC," Journal of Instrumentation 3 no. 08, (Aug., 2008) S08005. http://iopscience.iop.org/1748-0221/3/08/S08005.

[54] Aaron Dominguez. The cms pixel detector. Technical Report CMS-CR-2009-142. CERN-CMS-CR-2009-142, CERN, Geneva, Jun 2009.

[55] R Brunelire. Cms electromagnetic calorimeter performance and test beam results. Nucl. Instrum. Methods Phys. Res., A, 572(1):33Ð35, 2007.

[56] The CMS Collaboration. The tridas project technical design report, volume 1: The trigger systems. CERN/LHCC 2000-038, CMS TDR 6.1, 2000.

[57] The CMS Collaboration. The tridas project technical design report, volume 2: Data acquisition and high-level trigger. CERN/LHCC 2002- 26, CMS TDR 6.2, 2002.

[58] The CMS experiment at the CERN LHC, 2008 JINST

[59] CMS collaboration, The CMS muon project, technical design report, CERN-LHCC-97-032, http://cdsweb.cern.ch/record/343814.

[60] The CMS Collaboration. "The Muon Project: Technical design report". CERN/LHCC 97-32, 1997.

[61] M. Aguilar-Benitez et al., Construction and test of the nal CMS barrel drift tube muon chamber prototype, Nucl. Instrum. Meth. A 480 (2002) 658.

[62] V. Barashko, Performance validation tests of the cathode strip chambers for CMS muon system, IEEE Nucl. Sci. Symp. Conf. Rec. 2 (2005) 827.

[63] R. Santonico and R. Cardarelli, Development of resistive plate counters, Nucl. Instrum. Meth. 187 (1981) 377.

[64] M. Abbrescia et al., Local and global performance of double-gap resistive plate chambers operated in avalanche mode, Nucl. Instrum. Meth. A 434 (1999) 244.

[65] CDF Collaboration, F. Abe et al., Phys. Rev. Lett. 74, 2626 (1995)

[66] D0 Collaboration, S. Abachi et al., Phys. Rev. Lett. 74, 2632 (1995)

[67] CDF and Do Collaborations, TEVEWWG, Combination of CDF and D0 results on the mass of the top quark using up to 5.8 fb^{-1} of data (2011)

[68] M. Jezabek and J. H. Kuhn, Nucl. Phys. B314, 1 (1989).

[69] HERAPDF 1.5 NNLO (https://www.desy.de/h1zeus/combined_results/herapdftable)

[70] M. Cacciari et al., JHEP 0809, 127 (2008); N. Kidonakis and R. Vogt, Phys. Rev. D78, 074005 (2008); S. Moch and P. Uwer, Nucl. Phys. (Proc. Supp.) B183, 75 (2008).

[71] N. Kidonakis, Phys. Rev. D83 (2011) 091503.

[72] N. Kidonakis, Phys. Rev. D81 (2010) 054028.

[73] N. Kidonakis, Phys. Rev. D82 (2010) 054018.

[74] T. Stelzer, Z. Sullivan and S. Willenbrock, Phys. Rev. D58, 094021 (1998)

[75] CMS Collaboration, "Particle-Flow Event Reconstruction in CMS and Performance for Jets, Taus, and $\not{E}_{\mathrm{T}}$", CMS Physics Analysis Summary CMS-PAS-PFT-09-001, (2009)

[76] M. Cacciari et al., The anti-k_T jet clustering algorithm, JHEP 04 (2008) 063.

[77] The CMS Collaboration, Determination of the Jet Energy Scale in CMS with pp Collisions at $\sqrt{s} = 7$TeV, CMS-PAS JME-10-010.

[78] G. Mahlon et al., Improved Spin Basis for Angular Correlation Studies in Single Top Quark Production at the Tevatron, Phys.Rev. D55, 7249 (1997)

[79] CMS Collaboration, "Measurement of the single top t-channel cross section in pp collision at $\sqrt{s} = 7$TeV using 2011 data", CMS Physics Analysis Summary CMS-PAS-TOP-11-021, (2011)

[80] J. M. Campbell, R. Frederix, F. Maltoni et al., "NLO predictions for t-channel production of single top and fourth generation quarks at hadron colliders", JHEP 10 (2009) 042

[81] J. M. Campbell, J. W. Huston, and W. J. Stirling, "Hard Interactions of Quarks and Gluons: A Primer for LHC Physics", Rept. Prog. Phys. 70 (2007) 89

[82] N. Kidonakis, "Differential and total cross sections for top pair and single top production", arXiv:1205.3453.

[83] CMS Collaboration , "Determination of jet energy calibration and transverse momentum resolution in CMS", JINST 06 (2011) P11002.

[84] M. Cacciari, G. P. Salam, and G. Soyez, "The anti-kt jet clustering algorithm", JHEP 04 (2008) 063.

[85] CMS Collaboration, "Measurement of the single-top t-channel cross section in pp collisions at centre-of-mass energy of 8 TeV", CMS Physics Analysis Summary CMS-PAS-TOP-12-011, (2012).

[86] CMS Collaboration, "Measurement of the single-top t-channel charge ratio at 8 TeV", CMS Physics Analysis Summary CMS-PAS-TOP-12-038, (2012).

RINGRAZIAMENTI

Voglio ringraziare il prof. Crisostomo Sciacca e l'intero gruppo CMS di Napoli, in particolare il dott. Luca Lista, Orso e Mario, per avermi guidato nello svolgimento del mio lavoro di tesi.

Un esame preparato insieme, una chiacchiera scambiata fuori la biblioteca, un corso seguito insieme ... per un motivo o per un altro, le nostre strade si sono incontrate. Ne è scaturito un irrefrenabile meccanismo di condivisione: emozioni, vino, gioie, lacrime, pizze, musica, inciuci, giorni e notti, tempo ... Miei cari amici, con tutto il mio affetto voglio ringraziarvi per essere stati, ognuno a suo modo, causa di quegli istanti in cui ritorna la voglia di vivere ad alta velocità. Grazie!
Per me è importante ringraziare Ciccio: mi hai fatto buona compagnia nelle lunghe sere di studio, accucciato sotto la scrivania.
E a voi che siete la mia famiglia, la mia mamma e il mio papà dedico questa Tesi. Grazie!